DEVELOPMENT AND IMPLEMENTATION OF A COMPENSATION TECHNIQUE FOR LUMINESCENCT SENSORS

A Dissertation

by

BRADLEY BRUCE COLLIER

Submitted to the Office of Graduate and Professional Studies of
Texas A&M University
in partial fulfillment of the requirements for the degree of

DOCTOR OF PHILOSOPHY

Chair of Committee,	Michael J. McShane
Committee Members,	Gerard L. Coté
	Javier A. Jo
	Sandun D. Fernando
Head of Department,	Gerard L. Coté

December 2013

Major Subject: Biomedical Engineering

ABSTRACT

Despite offering high specificity and speed compared to other methods, the dependency of the response of an enzymatic sensor on ambient oxygen concentrations. To investigate this issue, a reaction-diffusion model was developed using the finite element method. Due to the growing population of people with diabetes, glucose was chosen as a model analyte. This glucose sensor model was used to examine the oxygen dependency and the resulting inaccuracy of glucose predictions. To improve the accuracy of glucose predictions, an oxygen compensation method was developed which utilizes a variable calibration curve where the fit parameters are dependent on the ambient oxygen concentration. This allows a unique calibration curve to be obtained for every oxygen concentration. Glucose predictions made with this compensation technique were found to be within clinically acceptable regions more than 95% of the time whereas predictions made without compensation were clinically acceptable less than 50% of the time.

In order to apply this compensation technique for real-time analysis, ambient oxygen concentrations must be measured in parallel with the response of the glucose sensor. Despite the growing need for multi-analyte sensors such as this, a suitable method for monitoring multiple responses *in vivo* has yet to be developed. Due to the measurement flexibility provided by luminescence, a time-domain luminescence lifetime measurement system was developed. The Dynamic Rapid Lifetime Determination (DRLD) approach utilizes a dynamic windowing algorithm to select the optimal window width for calculation of lifetimes using an integrative approach. This method was

demonstrated with an oxygen-sensitive luminophore and shown to accurately determine lifetime values six orders of magnitude faster than traditional methods.

This method was then extended to simultaneous measurement of the lifetimes from two luminophores (Dual DRLD or DDRLD) for multi-analyte applications. The ability of DDRLD to calculate lifetimes was demonstrated using temperature and oxygen sensing films. Similar to oxygen compensation of glucose sensors, a temperature compensation method was investigated for oxygen sensors. Lifetimes of the temperature sensing films for dual films measurements made using DDRLD were not significantly different than individual film measurements using DRLD. Oxygen responses for dual films followed the same trend as individual film measurements and displayed a minimal difference on average (2%). Real-time, dynamic temperature and oxygen predictions were demonstrated using DDRLD in conjunction with temperature compensation of the oxygen sensing film response.

ACKNOWLEDGEMENTS

I would like to thank my committee chair, Dr. McShane, and my committee members, Dr. Coté, Dr. Jo, and Dr. Fernando, for their guidance and support throughout the course of this research.

Thanks also go to my friends, colleagues, and the department faculty and staff for making my time at Texas A&M University a great experience. I also want to extend my gratitude to the Texas A&M University Association of Former Students, which provided me funding in the form of a Graduate Merit Fellowship.

Finally, thanks to my mother and father for their encouragement and to my wife for her patience and love.

TABLE OF CONTENTS

Page

LIST OF FIGURES

Page

Page

Page

Page

Page

LIST OF TABLES

Page

1. INTRODUCTION

Despite the growing number of people living with diabetes mellitus, the current standard for monitoring blood glucose levels remains the "finger-prick" method. Although it is recommended to check blood glucose levels 6 to 8 times a day for most patients,[1] the pain and annoyance caused by this method often leads to inadequate glucose monitoring despite the many health complications associated with poor glucose monitoring and diabetes.[2-5] Currently, several continuous glucose monitoring systems (CGMS) are available on the market; however, several issues including compliance remain (see Chapter 2).[6-7]

To combat this non-compliance, a large amount of research is being performed on simple, pain-free sensing methods that can be used to monitor *in vivo* glucose levels.[6, 8] Although a variety of glucose measurement techniques have been proposed, many glucose sensors being developed utilize glucose oxidase (GOx) to transduce glucose concentration because of its specificity and fast reaction rate.[9] This enzyme allows glucose levels to be determined indirectly through changes in hydrogen peroxide or oxygen concentrations as well as changes in pH (Figure 1.1). Luminescent, enzymatic glucose sensors are attracting attention for glucose monitoring because of a possible "smart tattoo" implementation whereby the response of the sensor can be read non-invasively through the tissue.[10-13] These sensors often utilize oxygen-quenchable dyes which are able to provide high selectivity and sensitivity compared to electrochemical methods.[4, 8]

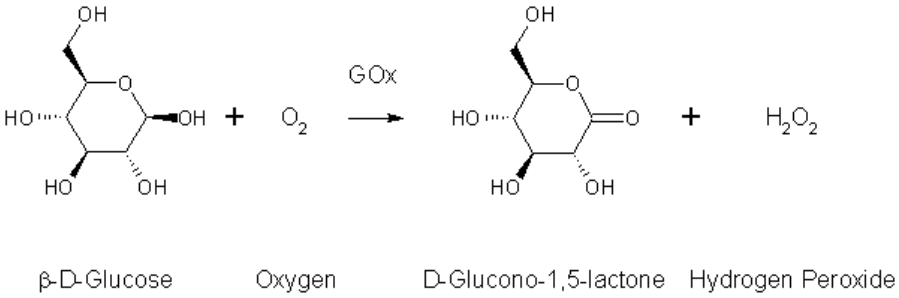

Figure 1.1 Generalized reaction scheme of glucose oxidase showing the substrates consumed and products.

Due to the enzymatic nature of these types of sensors, the steady-state is determined by a balance of the reaction and diffusion rates of the substrates.[12, 14-17] For sensors utilizing GOx, the response is consequently dependent on both oxygen and glucose levels.[15] Even though GOx consumes glucose and oxygen equally, these reactants are not present in equal or constant concentrations in the body. Changes in ambient oxygen concentration will affect the rate of glucose consumption causing shifts in sensor response leading to inaccurate glucose predictions.[18-23] To provide accurate *in vivo* measurements using luminescent glucose sensors, the response of the glucose sensor needs to be compensated for ambient oxygen concentrations. The glucose sensor response can be corrected to enable accurate glucose readings by measuring the ambient oxygen concentration with a second sensor.[18-23] However, a robust method capable of performing compensation has yet to be demonstrated for enzymatic glucose sensors.

Utilization an appropriate oxygen compensation method will also require the development of a method for simultaneously measuring the response of both the oxygen and glucose sensors. Due to scattering and auto-fluorescence associated with tissue, *in*

vivo measurements of implanted sensors can be significantly more complicated than *in vitro* measurements. Time-domain measurements of the lifetime response of luminescent sensors can be used to overcome these and other issues encountered with intensity-based measurements.[24] Non-linear least-squares analysis is typically utilized to fit the decay data and obtain a lifetime value; however, this approach can be computationally intense and dependent on the initial guesses of the fit.[25] Simultaneous measurements of glucose and oxygen sensors will increase the complexity of the measurement due to the need to separate the individual sensor responses and the extensive calibration required.[26] Thus, in order to accurately make simultaneous measurements of the luminescence lifetime response of these sensors, a new evaluation method must be developed that is suitable for *in vivo* measurements.

Following a review of the appropriate background material, the following separate research aims were developed to address these aforementioned issues. First, *the oxygen-dependence of enzymatic glucose sensor response will be investigated using finite element analysis and an appropriate oxygen compensation technique will be developed*. Concurrently, *a luminescence lifetime calculation technique will be developed that can be utilized for real-time measurement applications for both single and dual luminophore responses*. The future goal, outside the aims of this work, will be to utilize the dual response measurement technique for use with oxygen compensation of luminescent, enzymatic glucose sensors. The research performed to achieve these aims as well as further background information will be provided herein.

As mentioned, development of an oxygen compensation method for enzymatic glucose sensors was performed *in silico*. A model for a luminescent, enzymatic glucose sensor using a hydrogel matrix will be developed using COMSOL, a finite element analysis modeling software. With this model, different properties of the sensor will be modified and the oxygen dependent glucose response will be determined. After *calibration* at a range of physiologic glucose and oxygen concentrations, mathematical trends can then be obtained and used for oxygen compensation purposes. The realization of this compensation mechanism will allow the appropriate oxygen dependent calibration curve to be determined by monitoring the ambient oxygen concentrations using a separate oxygen sensor, similar to other approaches.[18-20, 22] Once the ambient oxygen concentration is determined, the appropriate calibration curve can be selected, allowing a more accurate prediction of glucose levels.

A novel time-domain lifetime calculation technique will be investigated based on the Rapid Lifetime Determination (RLD) approach.[27-29] This approach will utilize windows with dynamic widths rather than static widths used in the past. I hypothesized that the Dynamic Rapid Lifetime Determination (DRLD) method will allow increased accuracy of lifetime over a wider range while still retaining improved calculation speed over traditionally used non-linear least squares calculations of lifetime. The method developed will be tested and verified using an oxygen-sensitive porphyrin similar to those utilized in luminescent, enzymatic glucose sensors.[30-31]

After demonstrating the feasibility of this method to determine the lifetime response of an individual sensor, this method will be expanded to allow the lifetime

measurement of two luminophores simultaneously with the goal of using this approach for oxygen compensation. The Dual DRLD (DDRLD) approach will calculate the actual lifetimes of each sensor allowing each sensor to be calibrated individually unlike other multi-sensor approaches utilizing time-resolved measurements of luminescence. In order to implement this method, the lifetime response of each luminophore must be distinct in order to resolve the individual responses. Similar to DRLD studies, the feasibility of DDRLD will be investigated using an oxygen-sensitive porphyrin. Due to the temperature-sensitivity of porphyrins, a temperature-sensitive inorganic phosphor will also be used which will allow for compensation of the oxygen sensor response. Again, I hypothesize that DDRLD will display similar accuracy but improved calculation speed over traditionally used non-linear least squares lifetime calculations.

The content of this dissertation has been organized following the logical progression of the aims outlined above. Furthermore, several chapters are, of themselves, manuscripts that will be submitted for publication or are already in print. Chapter 2 gives an overview of different glucose measurement techniques that are currently being utilized or developed including enzymatic sensors which are of particular interest. In addition, previous reports of oxygen dependent responses and compensation methods are discussed in this chapter. Chapter 3 describes the modeling utilized to determine dependence of enzymatic glucose sensors on ambient oxygen concentrations. In addition, the proposed method of oxygen compensation is demonstrated. Lifetime calculation techniques for both single and dual lifetime measurements are reviewed in Chapter 4. In Chapter 5, the theory of DRLD is discussed and the accuracy of this

method is compared to other methods; chapter 6 extends this work to dual lifetime measurements. Chapter 7 concludes the work performed in this dissertation and proposes directions for future work. Implications of the results in the context of current sensing applications are also discussed.

2. GLUCOSE SENSOR BACKGROUND

As of 2010, diabetes mellitus affected 25.8 million people in the United States, or 8.3% of the population,[32] however, this number could increase to over 30% by 2050.[33] This chronic disease is characterized by high blood glucose levels as a result of the body's inability to produce (Type 1 diabetes) or utilize (Type 2 diabetes) insulin. If blood glucose levels are not properly monitored and treated with insulin or the appropriate medicine, people with diabetes have the risk of developing serious health-related complications including heart disease, stroke, hypertension, kidney disease, nervous system damage, and limb amputation.[32] If not prevented, these health complications can double the odds of people with diabetes dying prematurely compared to people of similar age without diabetes.[32]

In order to reduce the risk of these health issues monitoring of blood glucose levels is needed.[2, 6-7] Through self-monitoring, patients are more likely to keep their blood glucose levels within or near the normal range (euglycemia). This is often done by injecting insulin or taking oral medication when glucose levels are too high (hyperglycemia) or ingesting a sugar-containing substance when glucose levels are too low (hyperglycemia).

2.1 Measurements Utilizing Finger-Lancing

Despite the growing number of people living with diabetes and the documented benefits of controlling blood glucose levels, the current standard for monitoring blood glucose levels remains the "finger-prick" method.[1-2, 34] This method requires lancing a finger up to 6 to 8 times a day so that a blood sample can be obtained for testing with a

glucose meter and test-strip.[1] Due to the pain and inconvenience associated with this approach, patient compliance can often be low. To overcome this issue, millions of dollars are spent each year developing new glucose sensor technology that is less invasive and more patient friendly.[6] The ultimate goal is to develop an artificial pancreas that can replace the deficient pancreas of a person with diabetes.[2]

2.2 Commercial CGMS

Although an artificial pancreas is being researched on many fronts, a large amount of research time and money is being spent on developing continuous glucose monitoring systems (CGMS) which will allow improved glucose monitoring.[35] Adoption of CGMS will ultimately follow several key features including reliability, ease of use, and comfort.[2, 7] With the development of an improved CGMS that meets these criteria, non-compliance associated with self-monitoring will become less of an issue.[2] Several different methods have been researched in order to achieve a working CGMS; the more prominent techniques will be discussed below.

2.2.1 Electrochemical

Most commercial CGMS currently on the market utilize enzymatic transduction to monitor glucose levels in the body's interstitial fluid using a needle-type-sensor with an assay similar to test-strips used with glucose meters.[7] Glucose oxidase consumes glucose and oxygen to produce hydrogen peroxide and glucono-δ-lactone which hydrolyzes to gluconic acid (Figure 1.1). Glucose levels can then be measured indirectly, by monitoring hydrogen peroxide or oxygen levels amperometricallly using a two or three electrode system.[36-37] Enzyme immobilization and matrix material are

important aspects of these and other types of sensors.[7, 37] For example, it is important to slow the diffusion of glucose relative to oxygen because the concentration of glucose is much higher than the oxygen concentration in the body.[23] This will reduce the oxygen-dependence of the sensor response as well as the sensitivity. Alternatively, different mediators can be used to eliminate the need for oxygen.[7, 37]

Currently, there are 2 commercially available, FDA-approved CGMS each employing an electrochemical approach for glucose monitoring. The Guardian REAL-Time from Medtronic MiniMed and the Dexcom SEVEN PLUS provide glucose measurements every 5 minutes and can be used for up to 3 or 7 days, respectively.[37-38] Although electrochemical sensors are commercially available, they still have many limitations. The response of the sensor can drift over time requiring frequent re-calibration (generally 2 times a day).[4, 37] Errors in glucose prediction can also occur due to biofouling and interference from a variety of chemicals found in the body.[2, 4, 35, 37] In addition, these subcutaneous sensors are still considered invasive because they are connected through the skin to external electronics for an extended period of time which could lead to vasculature damage or infection.[7, 35] It should also be noted that commercially-available CGMS are not approved to completely replace finger stick measurements as a means of monitoring blood glucose levels.[2] Despite this, many other electrochemical sensors are still being developed that measure glucose levels through hydrogen peroxide formation or oxygen consumption.[14, 38-46]

2.2.2 Microdialysis

Microdialysis is another approach currently used to measure glucose. For this technique, a hollow, semi-permeable fiber is implanted subcutaneously and used to remove small molecules from the tissue including glucose.[7, 37] This is done by pumping an isotonic fluid through the fiber which allows glucose to diffuse down its concentration gradient into the fiber. The solution is then pumped to an electrochemical detector outside of the body for glucose measurement. This reduces the effects of ambient oxygen concentration on glucose measurement. Biofouling is also reduced but can still cause blockages of flow through the fiber.[37] In addition, measurement times are generally slow with this approach due to the flow rate of the solution.[7, 37] Although a device (GlucoDay, Menarini) using this approach is commercially available, it is typically utilized in a hospital setting for retrospective analysis following data collection for an extended period of time.[37]

2.2.3 Reverse Iontophoresis

Another approach utilizes reverse iontophoresis to make glucose measurements.[37, 47-49] Glucose and other subcutaneous fluids are pulled through the skin by applying a small current across a hydrogel that is in contact with the skin.[7, 37, 50] Glucose is then measured outside of the body using an electrochemical approach similar to the ones described above.[7, 37, 50] This approach is not as susceptible to oxygen fluctuations because the hydrogel is exposed to the ambient air. In addition, biofouling is less of an issue because the skin acts as a natural filter.[7] However, the current exposed to the tissue can cause skin irritations and the method has been shown to be

inaccurate (glucose concentrations in the hydrogel are 1000 times less than ISF concentrations) especially when sweat is present.[4, 7, 37] A system (GlucoWatch, Cygnus) using this transduction method was briefly available before being removed from the market in 2008 due to the issues discussed above as well as long warm up times and frequent re-calibration.[7, 50]

2.3 Optical Methods of Glucose Detection

As an alternative to electrochemical sensors, optical measurements of glucose have been gaining interest in recent years due to their measurement flexibility and sensitivity.[4, 26] Some of the optical methods that have been reported are no longer of interest for *in vivo* glucose measurements due to poor accuracy and/or low signal. These include infrared spectroscopy, intrinsic tissue fluorescence, and diffuse reflectance.[4, 7, 37] However, many other optical measurements of glucose have shown more promise and continue to be researched. Inelastic Raman scattering measurements are also being researched as a glucose measurement technique. However, this approach is susceptible to interference from a variety of analytes. Surface-enhancement is often utilized to improve the signal strength but multivariate analysis is still required.[7, 51] Glucose levels can also be measured through changes in the polarimetry of light shone through a solution containing optically active glucose.[7] This type of measurement is limited to the aqueous humor of the eye due to the loss of polarization through other tissue regions.[52-57] Many other optical glucose measurement techniques such as optical coherence tomography and photoacoustic spectroscopy are still in relatively new phases of development.[6-7, 58-61]

2.4 Luminescence

In contrast to the optical methods of glucose measurement mentioned above, a variety of luminescence-based techniques have been investigated. This approach is of particular interest because of its speed and potential for high sensitivity due to low background.[4, 7] Most luminescent methods utilize proteins to transduce a signal either through binding or enzymatic consumption of glucose. Proteins that can physically bind glucose are used for binding-based assays whereby a measurable signal is transduced based on conformational changes of the protein or displacement of a competing ligand. Enzymatic sensors, however, often measure glucose indirectly as discussed previously. Due to the breadth of these types of sensors, they will be discussed in more detail.

2.4.1 Binding-Based Glucose Assays

A variety of proteins have been utilized to develop glucose sensing assays including Concanavalin A, glucose-binding protein, and different apo-enzymes. The different transduction mechanisms used with each protein are also quite varied although most use luminescence in some form.[4, 8] In addition to proteins, boronic acids have shown the ability to bind glucose and be utilized in measurement assays.

2.4.1.1 Concanavalin A

Concanavalin A (Con A) was one of the first proteins to be used for glucose binding assays. This tetrameric protein has four binding sites that can interact with glucose making it useful for competitive binding assays.[8] These assays generally transduce a signal using a dual labeled approach[62-68] or a single label approach.[69-71] The dual label approach often utilizes Förster resonance energy transfer (FRET) where when

the donor dye is close to the acceptor dye, energy is transferred to the acceptor increasing its fluorescence and decreasing the fluorescence of the donor.[4, 7-8] Binding of glucose to the donor-labeled Con A displaces the acceptor-labeled competing ligand reducing the FRET efficiency and causing a shift in emission intensity.Single dye approaches utilize movement of the dye, into or out of the excitation pathway. This is controlled by immobilizing the non-labeled component (either the competing ligand or Con A) outside of the excitation pathway. Increases in glucose concentration allow the labeled component to enter the excitation pathway causing an increase in measured fluorescence. Although a variety of assays using Con A have been developed, they are susceptible to a variety of problems including low range, stability, and specificity issues.[8] Toxicity may also be an issue due to agglutination of biologically relevant complexes,[8] however, the risk can be reduced by carefully selecting the tissue exposure site and reducing the concentration of the protein.[72]

2.4.1.2 Glucose Binding Protein

Another binding protein often used for glucose sensors is appropriately called glucose binding protein or GBP. Conformational changes in GBP upon binding glucose allow FRET-based assays to be used for glucose detection.[8, 73-76] Single dye approaches have also been demonstrated.[74] Much of the work done with GBP investigates ways to reduce the affinity for glucose because it is naturally too high to use as a useful glucose sensor.[8, 77-79] Specificity is another concern with GBP because of its ability to also bind galactose.[8]

2.4.1.3 Apo-Enzymes

Apo-enzymes are enzymes that have had their co-enzyme removed so that the enzyme can no longer consume glucose but is still allowed to bind it.[8] Glucose oxidase, which has only one glucose binding site, is often used for this kind of assay. Glucose measurements are made using intrinsic fluorescence of the protein[80-81] or competitive binding assays similar to the ones used with Con A.[82-86] However, there is some concern that apo-enzymes are only moderately stable.[8]

2.4.1.4 Boronic Acid

In addition to the binding proteins already discussed, boronic acids are capable of binding several diols including glucose.[87-113] Glucose binding leads to a conformational change in the molecule allowing an optical transduction to occur through FRET, photoelectron transfer, or internal charge transfer.[4, 7-8] Much of the work done on these types of sensors is spent on improving the selectivity of boronic acid over other diols including galactose, allose, mannose, and ethylene glycol.[8, 100] Although the acid dissociation constant of glucose can be tuned by including electron withdrawing or donating groups, sensors based on boronic acid are also dependent on the ambient pH.[8]

2.4.2 Enzymatic Sensors

Many of the luminescent glucose sensors currently being developed utilize glucose oxidase (GOx) similar to commercially available electrochemical methods. This enzyme is often chosen because of its fast reaction rate, reversibility, and specificity.[9] As seen in Figure 1.1, glucose levels can be indirectly measured through oxygen consumption, hydrogen peroxide, or shifts in pH (glucono-δ-lactone hydrolyzes to

gluconic acid).[8, 114] Intrinsic changes in protein fluorescence can also be monitored.[8] Other enzymes that utilize an electron donor other than oxygen have also been used to monitor glucose levels but these are not as common.[8] The reaction of GOx with glucose and oxygen follows the following generalized reaction scheme:

$$E_{ox} + G \overset{k_1, k_{-1}}{\longleftrightarrow} E_{ox}G \overset{k_2}{\rightarrow} E_{red}GDL \overset{k_3}{\rightarrow} E_{red} + GDL \quad 2.1$$

$$E_{red} + O_2 \overset{k_4}{\rightarrow} E_{ox}H_2O_2 \overset{k_5}{\rightarrow} E_{ox} + H_2O_2 \quad 2.2$$

where E_{ox} is the oxidized form of GOx, G is glucose, E_{red} is the reduced form of GOx, GDL is glucono-δ-lactone, O_2 is oxygen, H_2O_2 is hydrogen peroxide, and the k_n terms refer to the binding or reaction rates.

2.4.2.1 Direct, Enzymatic Glucose Sensing

Intrinsic fluorescence changes often in the co-enzyme allow glucose levels to be monitored directly.[7-8] The advantage of this approach is it does not require labeling the enzyme with a dye.[4] However, intrinsic fluorescence is usually weak and changes are often very small.[4, 8] Direct monitoring can also be performed with a fluorescence quencher that competes for binding with glucose.[115]

2.4.2.2 Indirect, Enzymatic Glucose Sensing

Enzymatic glucose sensors typically monitor glucose levels indirectly as previously mentioned. There have been relatively few luminescence methods developed that measure glucose through hydrogen peroxide production because there are not very many transduction mechanisms that allow for measurement of hydrogen peroxide.[8, 116-118] Many of these approaches, however, are based on recent work with quantum dots which are widely considered toxic without appropriate encapsulation.[119] In addition,

hydrogen peroxide can be toxic to the body and the enzyme leading to decreased working lifetime. To reduce these issues, catalase or another hydrogen peroxide consuming enzyme is often included in enzymatic sensors.[31, 120-123] Glucose measurement through changes in pH is also not very common because the initial pH of the environment as well as the buffering range may not be known leading to unpredictable glucose responses.[8] Oxygen consumption is a very common method for enzymatically measuring glucose levels due to the prevalence of oxygen quenchable dyes which provide high sensitivity, long lifetimes, and red to NIR emission.[8, 10-11, 17, 30-31, 124]

2.5 Oxygen-Dependence and Compensation of Enzymatic Glucose Sensors

Although there are numerous advantages to luminescent, enzymatic glucose sensors, inaccurate glucose predictions can arise due to variable ambient oxygen levels.[18-20, 22-23] Because the sensor response is highly dependent on reaction and diffusion rates of the substrates (glucose and oxygen), shifts in substrate concentration can easily lead to shifts in the response resulting in inaccurate glucose predictions.[23] This could be especially problematic for *in vivo* applications where oxygen concentrations are actually much lower than glucose levels and cannot be controlled. This has led many sensors to be designed such that glucose diffusion is slowed relative to oxygen diffusion in order to reduce oxygen-dependence of the sensor response; however, changes in the ambient oxygen concentration can still lead to inaccurate glucose predictions. [23] Despite this issue, there has been relatively little work on

methods to perform compensation for changes in the ambient oxygen concentration and maintain accurate glucose predictions.

Zhang *et al.* were the first to investigate the oxygen-dependence problem using amperometric sensors.[23] They found that by reducing the diffusion of glucose into the sensor, oxygen-dependence was also reduced. However, sensitivity is sacrificed in this process and low oxygen levels could conceivably still lead to an oxygen-dependent response. Other methods to reduce the oxygen-dependent response of amperometric sensors include supplying oxygen internally [125] and circumventing the use of oxygen by wiring the enzyme directly to an electrode using a mediator.[126] Despite these attempts to reduce oxygen-dependence, the response of these sensors is not completely independent of the ambient oxygen concentration.[19, 21]

Rather than reduce oxygen-dependence of the sensor response, another approach is to incorporate a second sensor to monitor ambient oxygen concentrations.[18-19, 21] This method is usually utilized for sensors that monitor consumption of oxygen. This method was first demonstrated using luminescence by Li *et al.* who used a glucose sensor and a reference oxygen sensor in a fiber optic probe.[19] The oxygen sensor was identical to the glucose sensor, with the exception that GOx was excluded from the sensing matrix. By measuring the response of both sensors simultaneously, glucose levels were related to the difference in the oxygen concentration at each sensor.[18-19] They also found that sensors with lower glucose sensitivity were less dependent on ambient oxygen concentrations. Pasic *et al.* used a similar approach where the difference in oxygen concentration from the glucose sensor to a reference oxygen sensor was used to

determine glucose concentrations.[21] The amount of oxygen-dependence was then determined by analyzing the results using Michaelis-Menten kinetics similar to previous methods.[127] In all cases, this approach was only demonstrated for sensors with a linear response and will not be applicable for sensors with non-linear responses.

Another approach was proposed by Wolfbeis *et al.* where the *difference* in oxygen concentration at the glucose sensor and at the reference oxygen sensor plays a key role.[22] With this approach, however, several assumptions must be made: the oxygen and glucose sensor have similar oxygen responses, the difference in oxygen concentration between each sensor is linear with glucose levels, and this difference must also be proportional to ambient oxygen concentrations. Using both linear and non-linear Stern-Volmer relationships and these assumptions, equations were derived that could calculate glucose concentrations with variable ambient oxygen concentrations. Although these equations were straightforward, the authors did not show any *in vitro* testing results; thus, the validity of this method has not been demonstrated.

These methods are limited to sensors with a specific kind of response because of the assumptions made in the compensation algorithm. For example, these approaches generally assume that the difference in the response of the oxygen and glucose is linear. However, this is only true for low and moderate glucose levels and cannot be used due to the high glucose levels associated with diabetes.[22] If GOx levels are increased in order to improve sensitivity or longevity of the sensor, the linearity of this response will also be lost making this approach even less feasible. Thus, a new oxygen compensation technique that can be applied to any glucose sensor with the aid of a reference oxygen

sensor will be investigated. This technique will remove many assumptions, but will require more thorough calibration of the glucose sensor so that trends in the oxygen-dependent glucose response can be found. In principle, accurate glucose measurements can be made at any ambient oxygen concentration. Once an acceptable oxygen compensation method has been developed, there needs to be a method to monitor the response of the oxygen and glucose sensor. Different techniques for measuring luminescence for both single and multiple sensors will be discussed in the following chapters.

3. OXYGEN-DEPENDENCE AND COMPENSATION OF LUMINESCENT, ENZYMATIC GLUCOSE SENSORS

Enzymatic sensors are considered reaction-diffusion systems because the sensor response is dependent on the rate of reaction as well as the diffusion of the substrate(s).[12, 14-17] As mentioned above, glucose oxidase (GOx) consumes both glucose and oxygen, meaning the response of enzymatic glucose sensors is dependent on both substrates. This makes it more difficult to predict the overall system response as discussed below.[15] Electrochemical sensors are able to make the system quasi-dependent on a single species, glucose, by slowing glucose diffusion relative to oxygen such that the reaction rate of GOx is limited by glucose concentration only, *i.e.* oxygen is always in excess.[23] This can be done because electrochemical sensors monitor an enzymatic product, hydrogen peroxide. Luminescent, enzymatic glucose sensors, however, typically monitor oxygen levels to predict glucose concentration. This makes balancing the reaction-diffusion system more precarious because the sensor's response must be optimized while resolving oxygen-dependence. As discussed, investigation of the oxygen-dependent glucose sensor response has been limited to a few, isolated examples.[18-20, 22-23] The methods reported typically rely on the measured difference between the response of a glucose sensor and an oxygen sensor to be linear for all glucose and oxygen concentrations.[18-20] However, this will not always be the case resulting in inaccurate glucose predictions.

To investigate novel methods for compensation of enzymatic glucose sensor response due to variations in ambient oxygen concentrations, a model was developed

using COMSOL Multiphysics. This software uses finite element analysis to approximate solutions for a set of partial differential equations with a set of boundary conditions. This allows the reaction-diffusion system of an enzymatic sensor to be estimated and a sensor response to be determined.[31] By modeling the sensors with these simulations, the influence of a variety of parameters such as enzyme concentration and diffusion properties can be estimated very quickly without performing a host of *in vitro* experiments.

3.1 Theory of Enzymatic Sensor Model

A reaction-diffusion model was developed utilizing the finite elemental method (COMSOL v4.2a) to determine the steady-state response of a luminescent, enzymatic glucose assay immobilized in a hydrogel matrix where the base material is poly(2-hydroxyethyl methacrylate) (pHEMA).[30] The steady-state response of the sensor will depend on the enzymatic reaction rate and the diffusion coefficients of the substrates; in this case, glucose and oxygen. The literature was reviewed in order to determine common values for these diffusion coefficients of glucose (D_g) and oxygen (D_o) in hydrogel materials which have been or could be used for immobilization of enzymatic glucose assays (see Table 3.1).[30, 93, 128-141] From these data, an appropriate range of diffusion coefficients was determined for modeling purposes.

Models were run using D_g values of 1e-15, 1e-13, and 1e-11 m^2/s while the values D_o tested were 1e-13, 1e-11, and 1e-9 m^2/s. This gives a total of nine combinations of diffusion coefficients tested. Modeling the glucose sensor response using these values will allow appropriate material properties to be determined for

Table 3.1 Diffusion coefficients for glucose and oxygen reported for hydrogel materials. *Assuming a partition coefficient of 1.

Material	D_g (1e-10 m^2/s)	D_o (1e-10 m_2/s)	Reference
Polyacrylamide	2.7	8.0	30, 132
Poly(2-hydroxyethyl methacrylate)	0.081 – 0.083	0.14	30,138, 139
Poly(acrylamide-co-hexyl acrylate)	3.4		93
poly(*N*-isopropylacrylamide)	2.7 – 4.7		128
Nafion	0.07 – 0.095*		129
Alginate	6.58 – 6.63		130
Polyurethane blended with poly(vinyl alcohol-co-vinyl butyral)	0.000095 - 0.012		131
Poly(hydroxylethyl methacrylate-co-glycol acrylate>		0.1 – 0.5	133
Poly(N-vinyl-2-pyrrolidone-co-hydroxyethyl methacrylate)	0.01 - 6.62		134
Polypyrrole	0.00027		135
Cellulose	0.16		136
poly(ethylene glycol)/poly(acrylic acid)	2.5		137
Poly(hydroxyethyl methacrylate-co-ethylene glycol methacrylate)	0.022 – 0.038		140
Polyvinyl alcohol	0.45 – 0.62	3.6 – 9.9	141

sensors with optimal range and sensitivity. The enzymatic reaction was determined using the following set of simplified reaction equations described by Gibson *et al.*[142]

$$E_{ox} + G \overset{k_1}{\rightarrow} E_{red}GDL \overset{k_2}{\rightarrow} E_{red} + GDL \quad 3.1$$

$$E_{red} + O_2 \overset{k_3}{\rightarrow} E_{ox}H_2O_2 \overset{k_4}{\rightarrow} E_{ox} + H_2O_2 \quad 3.2$$

where E_{ox} and E_{red} are the oxidized and reduced form of GOx, respectively, G is glucose, GDL is glucono- δ –lactone, O_2 is oxygen, H_2O_2 is hydrogen peroxide and k_n

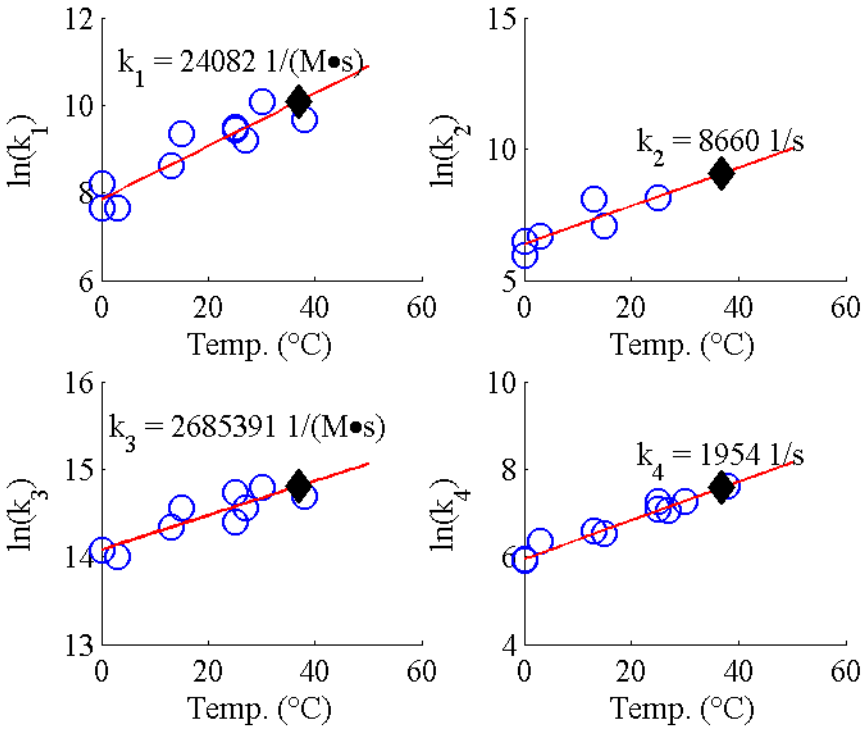

Figure 3.1 These graphs show reported reaction rate constants (blue circles) for Equations 3.1 and 3.2 versus temperature. Predicted values at 37°C are estimated (black diamonds) using linear regression (red lines) following a logarithmic transformation.

are the reaction rate values. The reaction rates utilized were determined by first establishing a relationship between rate constants and temperatures using values of reaction constants that were previously reported for a few different temperatures. These values were logarithmically transformed and plotted versus temperature, then fitted with linear regression to find a trend to predict rate constants at any arbitrary temperature. Logarithmic transformation is necessary due to the exponential dependence of the reaction rates as a function of temperature as defined by the Arrhenius equation. For the model used, reaction rates at 37°C were estimated similar to a method performed by Atkinson *et al.*[142-145] These fits and the values utilized can be found in Figure 3.1.

The model developed was based on previously reported sensors consisting of a hydrogel matrix with a cylindrical geometry.[30] The height of the sensor was 750 μm while the radius was 2.5 mm. The sensing assay (*i.e.* GOx and an oxygen-sensitive porphyrin) was uniformly distributed throughout the matrix. For simplicity, a one-dimensional mesh was used to model the response of a sensor with this geometry. This was done by assuming a symmetrical response from bulk oxygen and glucose concentrations and a semi-infinite boundary in the perpendicular direction, the sensor was modeled using a 375 μm linear mesh with a size of 0.5 μm. Bulk glucose and oxygen concentrations were varied at the edge of the sensor matrix within expected physiological values in order to determine the expected response for a range of values.

Glucose levels for a person with diabetes can have a wide range of values but are typically expected to be within 40 to 400 mg/dL (2.2 to 22.2 mM).[146] Normal physiological oxygen pressure can vary from 24 mm Hg in the dermis to 100 mm Hg in arterial blood.[147] These values can be converted to concentration using Henry's law:

$$c = \alpha p \tag{3.3}$$

where c is the oxygen concentration, p is the oxygen pressure, and α 1.is a solubility constant. Using a reported α of 1.35 μM/mmHg for tissue, the oxygen concentration of tissue-integrating, dermally implanted smart tattoo sensors can range from 22.9 to 135 μm O_2.[148] For modeling purposes, a range of 20 to 140 μm O_2 was utilized.

Using the defined reaction-diffusion system, the finite-element method will determine the steady-state oxygen concentration throughout the defined mesh for specified bulk oxygen and glucose levels. Examples of the oxygen distributions

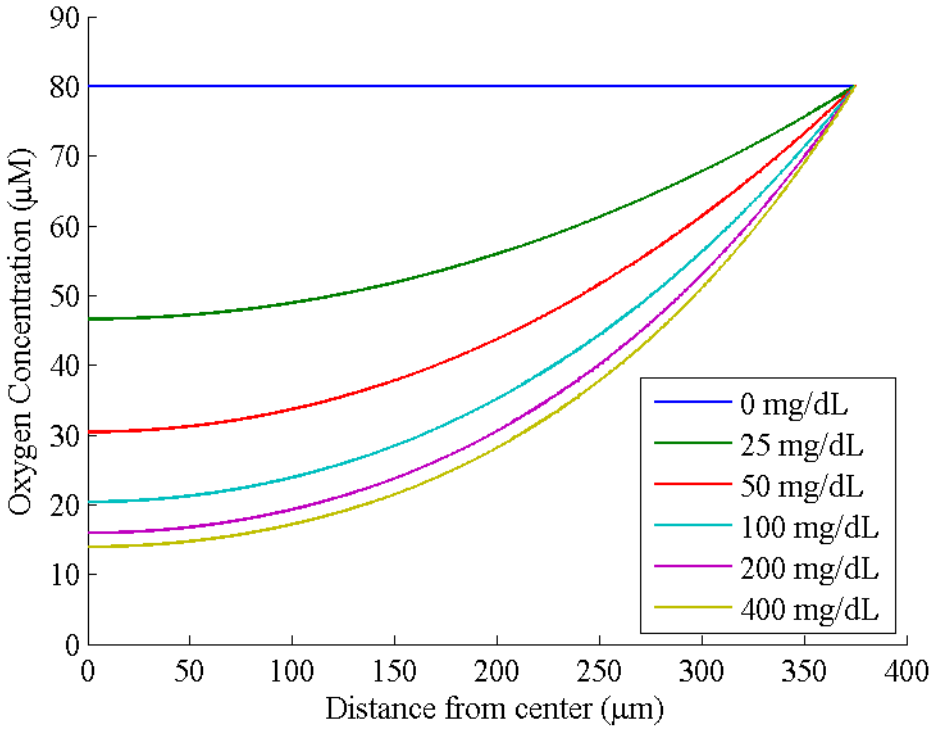

Figure 3.2 Oxygen distributions obtained for different glucose levels for a matrix with D_g and D_o set to 1e-11m^2/s, a bulk oxygen concentration of 80 μM, and a GOx concentration of 1.8e-10 M.

acquired can be seen in Figure 3.2. As expected, in the absence of glucose, oxygen concentration is uniform throughout the mesh at the same concentration as the bulk (80 μM). However, as glucose is introduced, oxygen levels decrease from the bulk concentration at the edge of the mesh to lower values in the center of the sensor. Oxygen levels will always be higher near the edge of the matrix due to the smaller diffusion distance and thus faster supply of oxygen from the bulk. However, higher glucose concentrations will allow more oxygen depletion inside of the matrix until the enzyme reaches a point where it cannot react any faster. This leads to a saturation point where the lifetime response of the sensor reaches a maximum value. The small

difference in the oxygen distribution from 200 to 400 mg/dL shows that the response of this sensor is near the saturation point at these glucose levels. Although not depicted, under the appropriate conditions (faster glucose diffusion, higher GOx concentrations, and slower oxygen diffusion) oxygen levels can be depleted within the sensor matrix.

As mentioned above, luminescent enzymatic glucose sensors can utilize an oxygen sensitive dye to measure the glucose response. The luminescent response, *i.e.* lifetime, is related to oxygen concentration through the Stern-Volmer relationship:

$$\frac{\tau_0}{\tau} = 1 + K_{SV}[O_2] \tag{3.4}$$

where τ_0 is the lifetime in the absence of oxygen, τ is the lifetime, K_{SV} is the Stern-Volmer constant, and $[O_2]$ is the oxygen concentration.[149] The Stern-Volmer properties utilized in this study were determined after measuring the response of a hydrogel sensor *in vitro*. Experimental details and results can be found in the following section.

To further characterize the modeled sensor response, the Thiele modulus was utilized. This parameter is often used to describe the reaction-diffusion properties of an enzymatic system.[14, 16, 36, 150-151] For glucose, the Thiele modulus is calculated using:

$$\Phi_g = \sqrt{\frac{k_{cat}[GOx]}{D_g[g]}}\, l \tag{3.5}$$

where k_{cat} is the catalytic turnover rate (k_2 in Equation 3.1), $[GOx]$ is the concentration of GOx, D_g is the diffusion coefficient for glucose, $[g]$ is the bulk glucose concentration, and l is the length of the matrix .[16] For this study, the glucose concentration was set to 400 mg/dL, the maximum concentration modeled, for all Φ_g calculations. Inspection of

Equation 3.5 reveals that the numerator represents the maximum rate of substrate conversion while the denominator represents the maximum rate of substrate transport.[150] Thus high values for the Thiele modulus (typically > 1) indicate the system is diffusion-limited, whereas low values (< 0.3) indicate a reaction-limited system.[15, 123, 151] A Thiele modulus can also be calculated for oxygen in a similar manner:

$$\Phi_o = \sqrt{\frac{k_{cat}[GOx]}{D_o[o]}}\, l \qquad 3.6$$

where D_o is the diffusion coefficient for oxygen, and $[o]$ is the ambient oxygen concentration. A value of 80 μM was utilized for all Φ_o calculations. The ratio of the Thiele moduli for oxygen and glucose is also of interest for oxygen-dependence studies. This allowed the investigation of oxygen-dependence in relation to the relative diffusional properties of the system. This ratio can be determined by:

$$\Phi_r = \frac{\Phi_o}{\Phi_g} = \sqrt{\frac{D_g[g]}{D_o[o]}} \qquad 3.7$$

where the catalytic turnover rate, GOx concentration, and matrix length from the original moduli cancel out, leaving contributions only from the relative concentrations and diffusivity of the two substrates.

3.2 Oxygen Response Measurements of a Hydrogel Sensor

Although K_{SV} and τ_0 will change from material-to-material due to diffusion properties,[149] the change in sensitivity to oxygen is expected to be minimal compared to dependence on enzymatic reaction rate and diffusion properties. Thus, to simplify

modeling and reduce the number of *in vitro* experiments, single values for K_{SV} and τ_0 were utilized for all cases.

The values utilized for these parameters were determined for a sensor similar to one previously reported.[30] To make this hydrogel, a solution was made by combining 2-hydroxyethylmethacrylate (HEMA, Polysciences, Inc.) and tetraethylene glycol dimethacrylate (Polysciences, Inc.) in a molar ratio of 98:2. Then 250 μL of this solution was mixed with 2.5 mg of the photoinitiator 2,2-Dimethoxy-2-phenyl-acetophenone (Aldrich). This was followed by additions of 100 μL of ethylene glycol (Sigma), 47.5 μL of de-ionized water, 100 μL of 5 mM tetramethacrylated palladium porphyrin dissolved in dimethyl sulfoxide (Sigma). The porphyrin was synthesized using Pd(II) meso-Tetra(4-carboxyphenyl)porphine (Frontier Scientific) as a base.[*] After mixing, the solution was added to a mold made by an 0.03" Teflon spacer placed between two glass slides. The solution was then vacuumed to remove any bubbles and UV polymerized for 5 minutes on each side. The resulting pHEMA hydrogel was placed in a solution of dichloromethane for 24 hours and then rinsed with acetone. The gels were then stored in a solution of 0.01 M phosphate buffered saline (PBS) until testing was performed.

The response of the sensor was tested by removing a sample from the gel using a 2.5 mm biopsy punch. The sample was then immobilized in a custom reaction chamber previously reported and the luminescence lifetime response to varying oxygen was determined.[152-153] The oxygen concentration was controlled by varying the flow rate of

[*] The methacrylated form of this dye was synthesized and graciously provided by Dr. Soya Gamsey of Profusa, Inc.

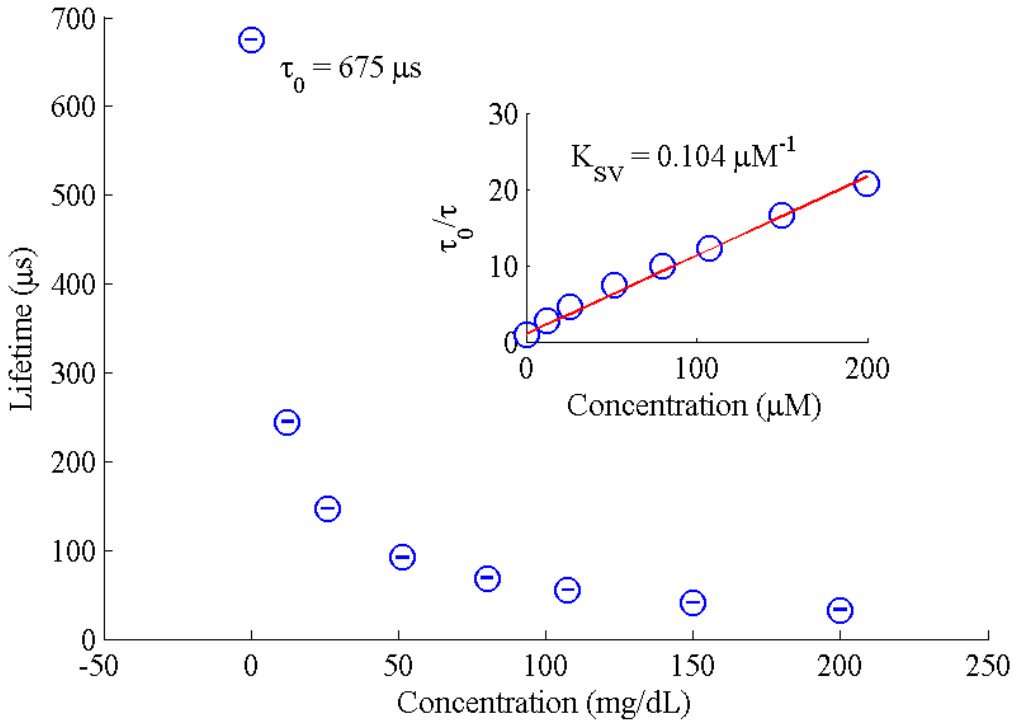

Figure 3.3 The lifetime response of an oxygen-sensitive palladium porphyrin immobilized in pHEMA. The inset shows the resulting Stern-Volmer plot. Error bars represent standard deviation with n = 10.

oxygen into a PBS solution. Chapters 5 as well as the appendices contain further details about the testing and measurement system utilized. The raw data were then analyzed using MATLAB (MathWorks, Inc.) to determine the oxygen response which can be seen in Figure 3.3. As expected, the sensor showed a higher sensitivity to oxygen at low concentrations. The Stern-Volmer quenching curve shown in the inset was fit using linear regression to determine K_{SV}. The values of K_{SV} and τ_0 used for modeling were 0.104 μM^{-1} and 675 µs, respectively.

3.3 Results and Discussion

3.3.1 Modeled Glucose Sensor Response

Initially sensor responses were modeled using a range of diffusion coefficients for glucose and oxygen based on reported values for hydrogels (Table 3.1). Three values were chosen for each diffusion coefficient, representing a total of nine unique *materials* with different diffusional properties, and, hence, different Thiele moduli. Enzyme concentration was also varied by selecting different values for Φ_g (0.1, 0.5, 1, 5, 10, and 50). The response curves obtained for the range of Φ_g values can be seen in Figure 3.4. Each graph also shows the results of different Φ_r values tested; repeated Φ_r values are due to the ratio of the diffusion coefficients tested (see above). There was very little response seen when Φ_g was less than 1, as expected. However, for response where Φ_g was 1 or larger and when Φ_r is 2 or less, the response of the sensor was also very low. When Φ_r is very large (>100), the response becomes saturated at very low glucose concentrations (<25 mg/dL) which was observed for all $\Phi_g \geq 1$. These results indicate that provided enough GOx, there is a "sweet spot" for Φ_r that would yield a desirable combination of high sensitivity and response over a wide range of concentrations before saturation is reached. Based on these results, diffusion coefficients for glucose and oxygen were both set to 1e-11 m^2/s so that a suitable range and sensitivity could be produced. Interestingly, these values are close to the reported values of pHEMA (Table 3.1).

In order to have a sensor with suitable response (*i.e.* range and sensitivity), Φ_r needs to be between 2 and 100 (Figure 3.4). When Φ_r is 16.7, the GOx concentration

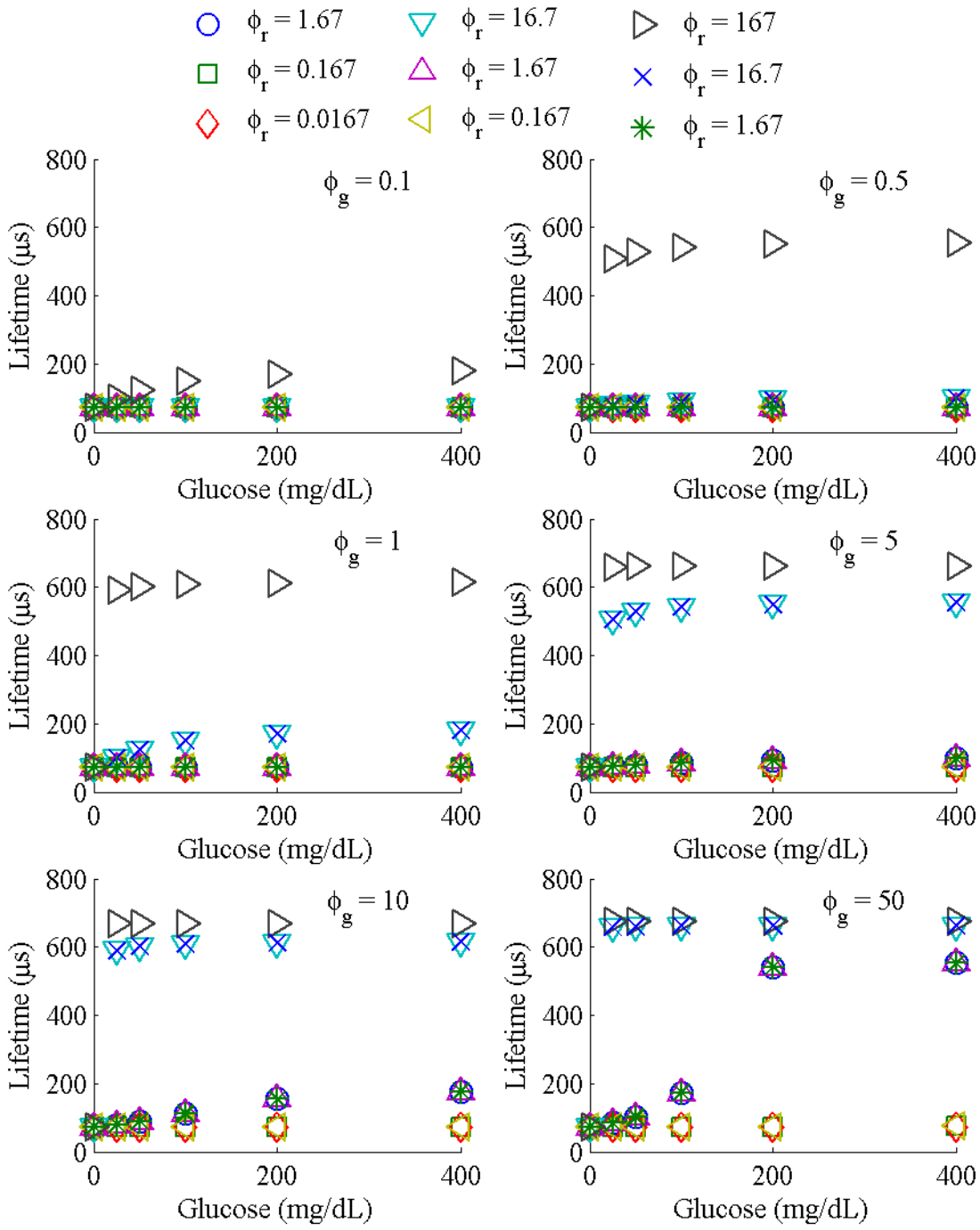

Figure 3.4 Representative glucose responses for a range of oxygen and glucose diffusion coefficients (represented in ratio form) as well as a range of Φ_g values.

plays more of a role in sensor response as seen in Figure 3.5. Using these diffusion coefficients, the lifetime response for different GOx concentrations was plotted versus glucose concentration and fit using:

$$\tau = -ae^{-[g]/b} + c \qquad 3.8$$

where a, b, and c are fit parameters. This was equation was chosen for the calibration curve because it showed a high goodness of fit (R^2) with the data evaluated. It should be noted that any equation can be utilized for calibration purposes (*i.e.* if the response profile follows a different shape) as long as a high quality of fit can be obtained allowing accurate predictions of glucose or other analytes. However, for compensation purposes

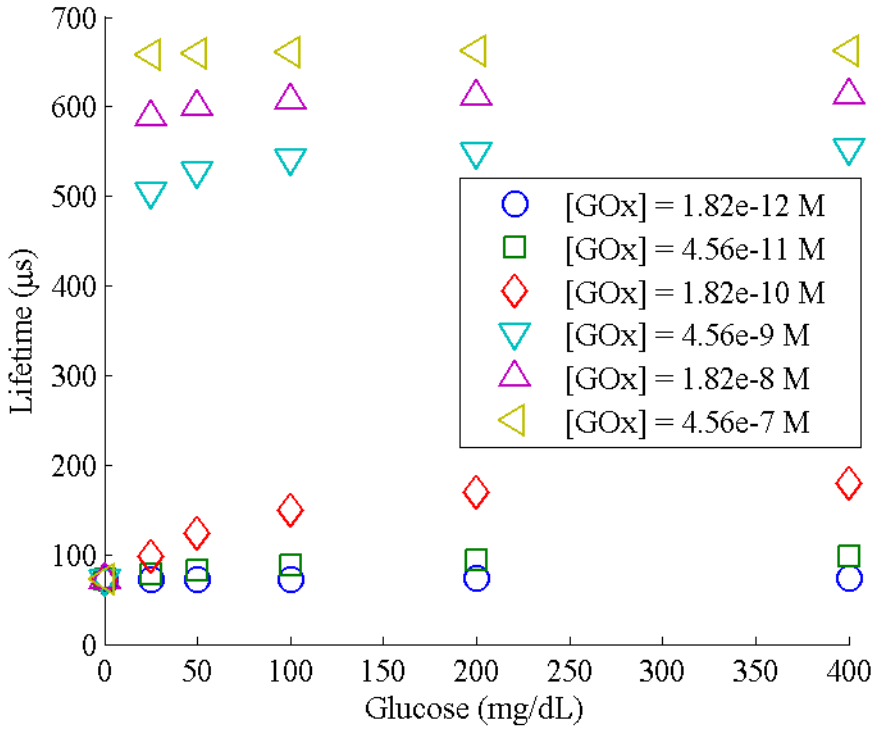

Figure 3.5 Modeled response of a sensor using different GOx concentrations and with D_g and D_o set to 1e-11m^2/s and a bulk oxygen concentration of 80 µM.

where the fit parameters will be determined as a function of the interfering analyte, an equation with fewer fit parameters is desired in order to reduce overall complexity of the calibration. This led to the selection of Equation 3.8 for calibration because only three fit parameters were required to obtain a high quality of fit.

Due to the exponential nature of Equation 3.8, parameter a is representative of the percent change of the signal while b is representative of the range and sensitivity. As expected, the values for a and b obtained after fitting the data in Figure 3.5 are inversely related for different GOx concentrations (Figure 3.6). As b decreases, the range will decrease but the sensitivity will increase and *vice versa*.

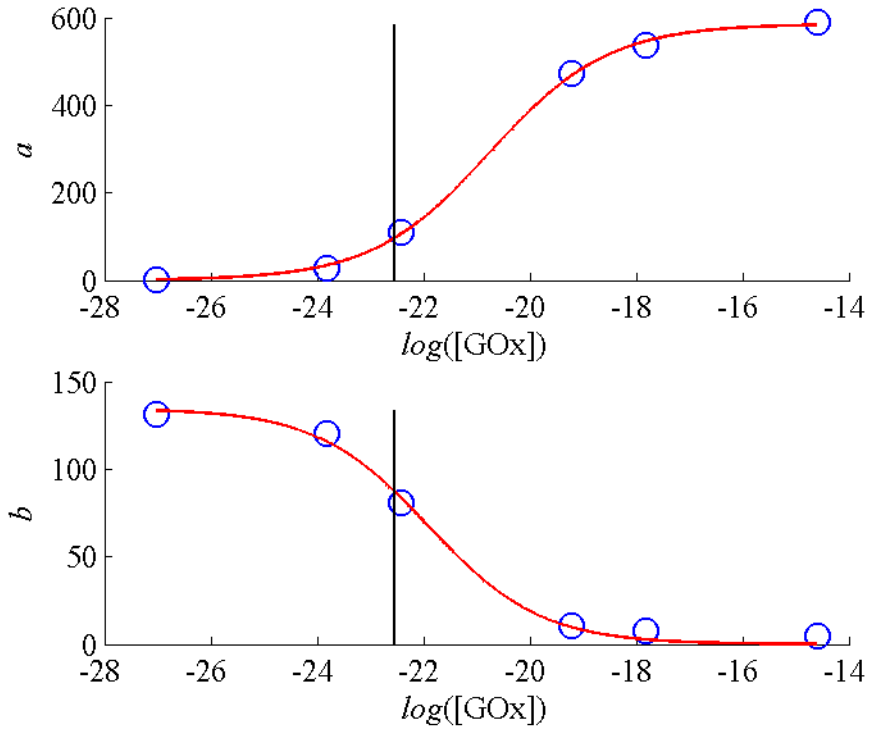

Figure 3.6 Plots of the values obtained for parameters a and b versus transformed GOx concentrations. Parameters were obtained by fitting the results in Figure 3.5. The black line in each graph represents the optimal GOx concentration for a range of 200 mg/dL.

To allow easier fitting of a and b, the GOx concentration was transformed logarithmically and through shifting ($t_{GOx} = \ln([GOx]) + \min(\ln([GOx]))$). Fitting was performed using:

$$X = \frac{A}{B + e^{Ct_{GOx}}} \tag{3.9}$$

where X is either a or b, t_{GOx} is the transformed GOx concentration, and A, B, and C are fit parameters. Fitting of the parameters using this equation allowed the trends in the range and sensitivity to be determined for a wide range of GOx concentrations. By defining the range as the point at which 90% of the exponential has decayed, the optimal value for b can be found using:

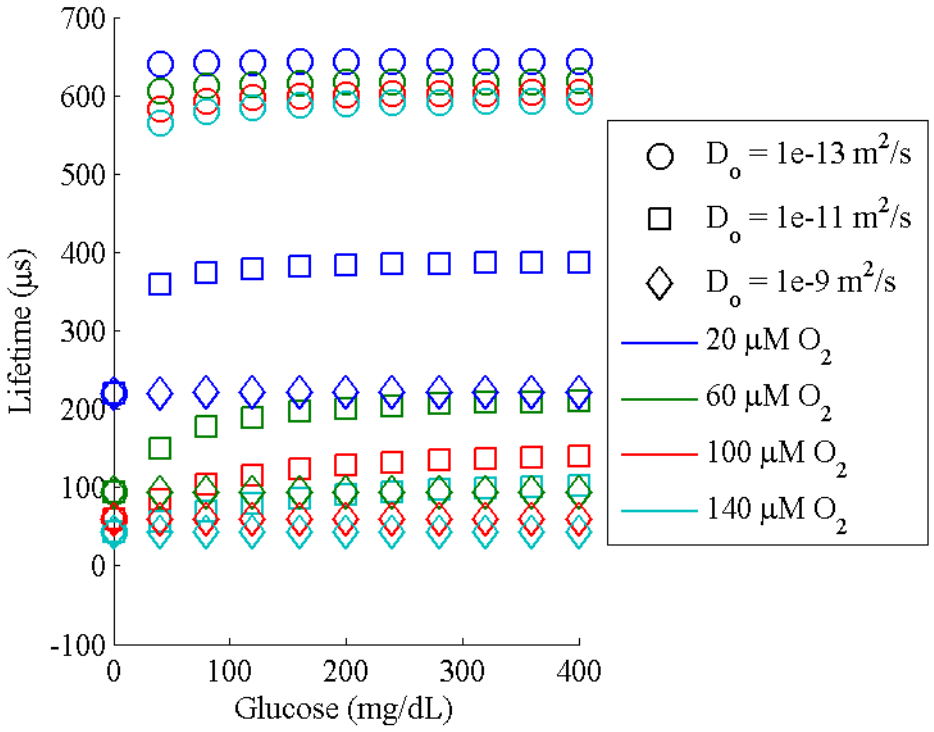

Figure 3.7 This graph shows the oxygen dependent response for three different model materials at four different oxygen concentrations.

$$b_{opt} = \frac{-R}{\ln(1 - {}^{P}/_{100})} \tag{3.10}$$

where R is the desired range and P is the percentage (90%). Once b_{opt} is known, the appropriate GOx concentration can be found using the fits for Equation 3.9. For a desired range of 200 mg/dL, the optimal GOx concentration was found to be 1.62e-10 M using Equation 3.10.

3.3.2 Oxygen Dependent Response of Enzymatic, Glucose Sensors

After finding the appropriate GOx concentration (1.62e-10 M) and diffusion coefficients (D_g=D_g= 1e-11 m^2/s), further sensor response modeling was performed for a range of oxygen concentrations. A range of oxygen diffusion coefficients (1e-13, 1e-11, and 1e-9 m^2/s) was again used to see if Φ_r would influence the response's dependency on oxygen. The results obtained can be found in Figure 3.7. For low values of D_o (1e-13 m^2/s) and high values of Φ_r (167), the response saturates at very low glucose concentration indicating a low range. At a higher value of D_o (1e-9 m^2/s) or lower values of Φ_r (1.67), the range is much higher, but the sensitivity is too low. When D_o and D_g are equal (Φ_r = 16.7), however, the response is improved because it shows suitable range and sensitivity, similar to the results seen in Figure 3.5.

Based on analysis of the previous data, a more extensive oxygen-dependence study was performed for a sensor with D_g=D_g= 1e-11 m^2/s and a GOx concentration of 1.62e-10 M. This was done by modeling the sensor response for a higher resolution within the already specified range of glucose and oxygen concentrations (Figure 3.8). After modeling, the responses were again fit using Equation 3.8. Fits were performed

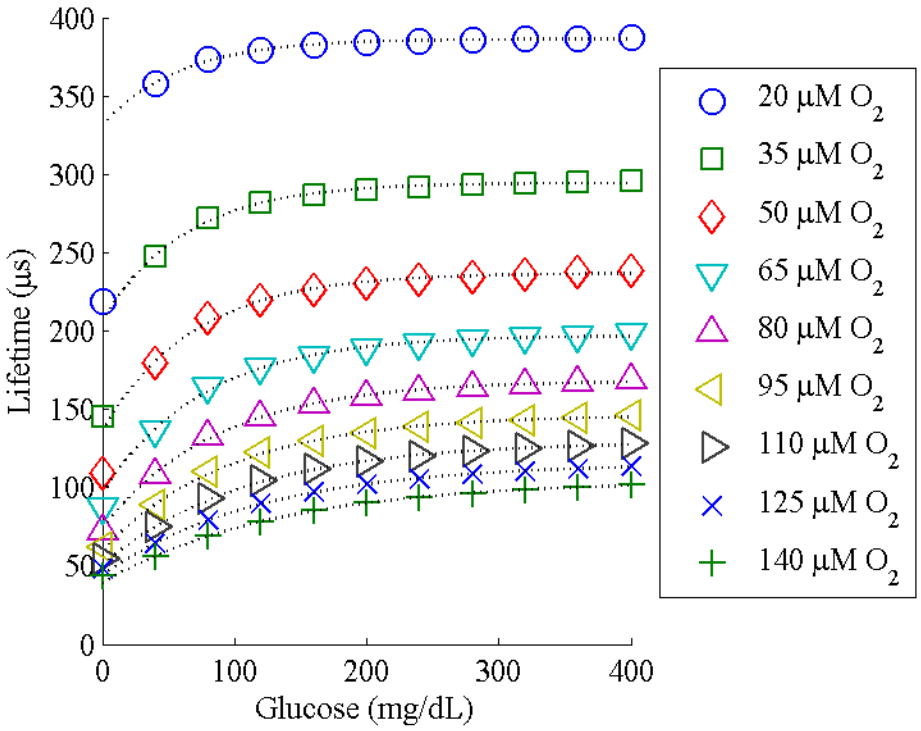

Figure 3.8 This graph shows the modeled sensor response for D_g=D_o= 1e-11 m^2/s, [GOx]=1.62e-10 M, and a range of oxygen concentrations. The dashed lines represent the fitting of the data for glucose values from 40 to 400 mg/dL.

for glucose values ranging from 40 to 400 mg/dL in order to increase the accuracy of the fit (R^2 > 0.99). It is assumed that using only the values above 40 mg/dL for the fitting is acceptable, as lower values will not affect the clinical treatment (*i.e.* sugar intake) for low glucose concentrations.[154]

The trends in the fit parameters were investigated by plotting them versus oxygen concentration and fitting them using a 4th order polynomial ($y = p_1x^4 + p_2x^3 + p_3x^2 + p_4x + p_5$). The complexity of this fit was required in order to ensure a high quality of fit ($R^2 \geq 0.9999$) for the calibration curves. The resulting fits of the data in Figure 3.8

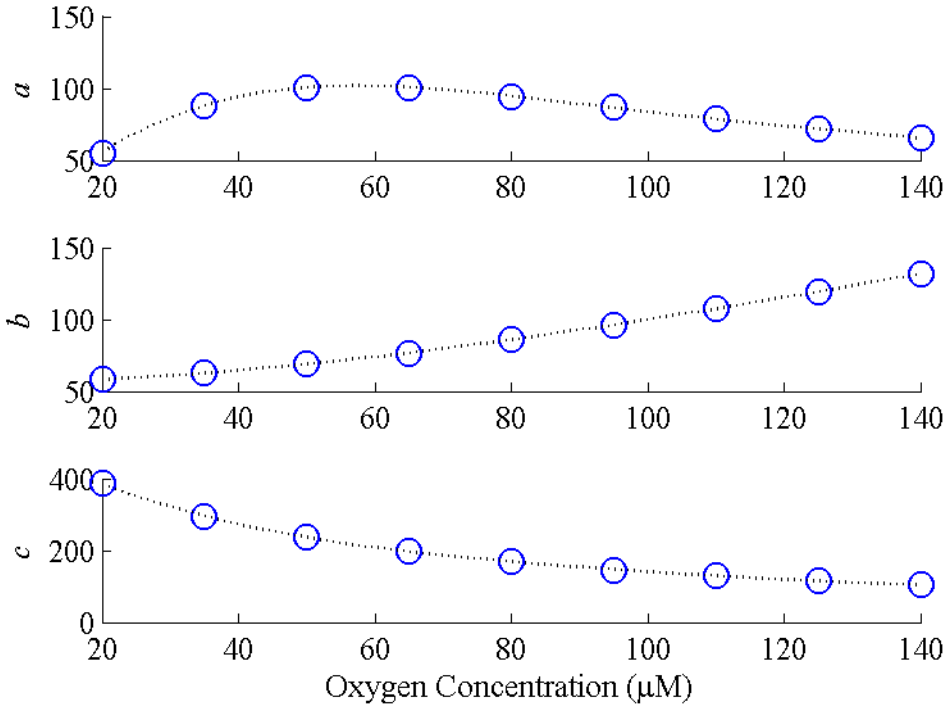

Figure 3.9 Fit parameters of Equation 3.8 as functions of oxygen concentration. Blue circles show actual values obtained and dashed lines represent the fit.

using the parameter values obtained from Figure 3.9 showed good agreement with the data in Figure 3.8 ($R^2 > 0.98$).

The data in Figure 3.8 were then used to perform preliminary oxygen compensation tests by comparing the predicted glucose values with the actual values. To determine the predicted glucose levels, Equation 3.8 was solved for the glucose concentration and the lifetime values from Figure 3.8 and the appropriate parameters for a, b, and c obtained from the fits in Figure 3.9 were inserted. These predictions were also compared with uncompensated glucose predictions using the calibration curve obtained for 80 μM oxygen which is in the middle of the oxygen range tested.

As can be seen in the Clarke error grid in Figure 3.10, many of the uncompensated glucose predictions fall within the C, D, and E zones indicating potentially dangerous errors in measurement.[154] Compensated glucose predictions, however, generally fall within the A and B zones which are clinically acceptable. It should also be noted that not all glucose predictions are displayed in Figure 3.10. Due to the imperfect nature of the fits, some of the lifetimes used to predict glucose were greater than the asymptote of the exponential curve, resulting in an imaginary glucose prediction. High glucose predictions (>400 mg/dL) are not shown either. In the case of

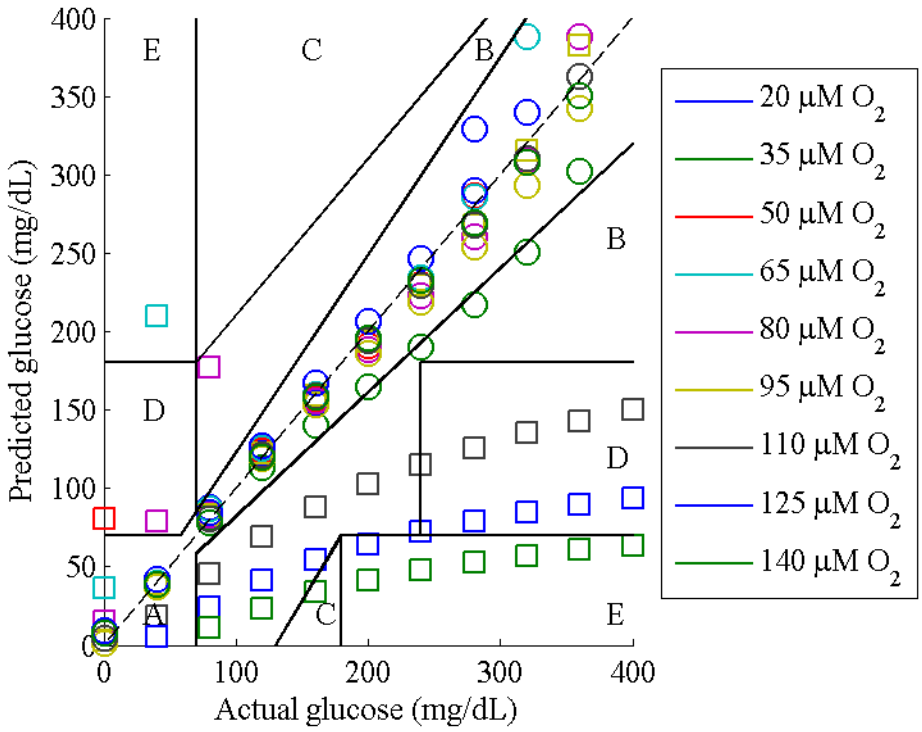

Figure 3.10 This graph shows a Clarke error grid of predicted glucose versus actual glucose concentrations for a range of oxygen concentrations. Circles show values predicted using oxygen compensation and squares show values predicted without oxygen compensation, assuming calibration was performed at 80 µM.

oxygen compensated glucose predictions, these predictions (high and imaginary) occurred at higher glucose levels (≥300 mg/dL) making it less clinically relevant. Uncompensated glucose predictions, however, produced high and imaginary predictions for the entire range of glucose values tested but this decreased as oxygen levels got closer to 80 μM.

Negative glucose values can also be predicted because the glucose curves were only fit from 40 to 400 mg/dL, however, this only occurred when the glucose level was 40 mg/dL or less. The clinical treatment in these cases would not change indicating that this not likely an issue. The number of predictions that fall into each region for each method can be found in Table 3.2. In order to assign a region to every prediction, the lines of the grid were extended for negative and high (>400 mg/dL) predictions and imaginary predictions were assumed to be 400 mg/dL. These results show that glucose predictions without oxygen compensation are only relevant at oxygen concentrations near the concentration at which the calibration was performed. These results indicate that compensation is necessary in order to have a viable glucose prediction.

Table 3.2 Number of glucose predictions that fall within the respective regions for each Clarke error grid displayed.

	Figure 3.10		Figure 3.11		Figure 3.13	
Region	Uncomp.	Comp.	Uncomp.	Comp.	Uncomp.	Comp.
A	33	94	10	99	22	77
B	12	4	38	0	23	20
C	31	1	44	0	48	1
D	10	0	2	1	2	2
E	13	0	6	0	5	0
% Clinically Acceptable	45%	99%	46%	99%	45%	97%

In order to more fully test the viability and necessity of oxygen compensation for enzymatic glucose sensors, 100 glucose predictions were made with and without compensation. The glucose calibration curve obtained at 80 μM was again used for uncompensated glucose predictions. Random concentrations were obtained using a reported physiological glucose distribution (μ=133.3 and σ=72.1 mg/dL) and a uniform oxygen distribution from 20 to 140 μM.[146]

As expected, Figure 3.11 shows that oxygen compensated glucose predictions are much more accurate than predictions that do not consider the ambient oxygen level.

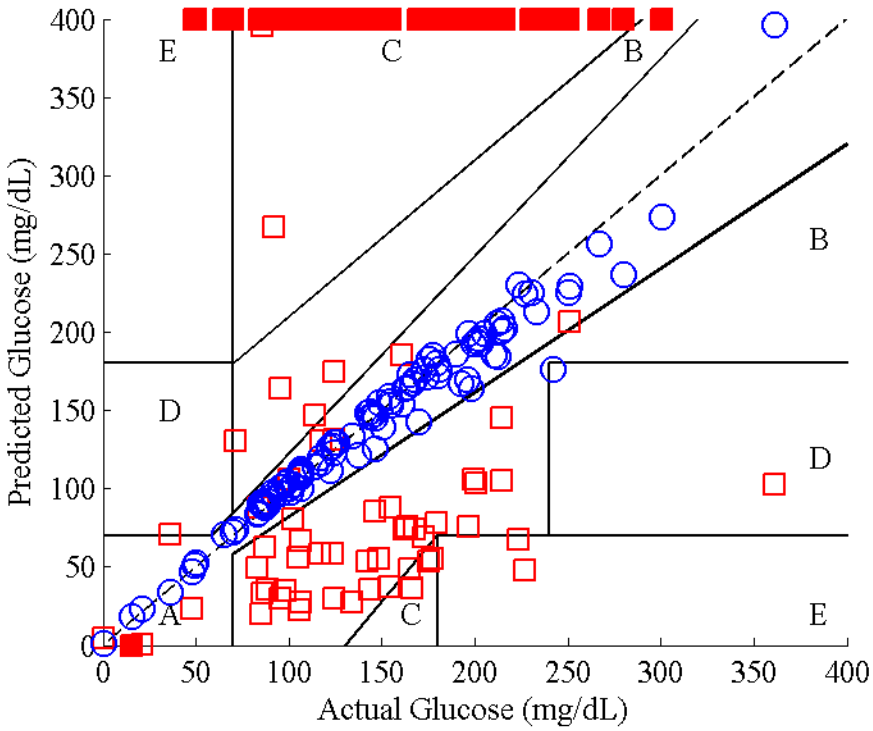

Figure 3.11 This Clarke error grid shows glucose predictions obtained from random oxygen and glucose values. Theoretical measurement error is not included. Blue circles show oxygen compensated predictions and red squares show uncompensated predictions. Markers that are filled in represent negative or imaginary glucose predictions (see text). It should be noted that these values only represent the presence of an erroneous prediction and not an actual predicted glucose value.

Within physiological glucose concentrations, all predicted glucose values using compensation were found to be real and positive, *i.e.* no erroneous predictions were made. However, uncompensated predictions again produced a large number of erroneous measurements (44 imaginary and 1 negative). The difference in the actual and predicted glucose values was also plotted versus oxygen concentration, providing insight into the importance of oxygen compensation (Figure 3.12). Values near zero represent measurements with higher accuracy; as accuracy decreases the difference moves away from zero on the y-axis.

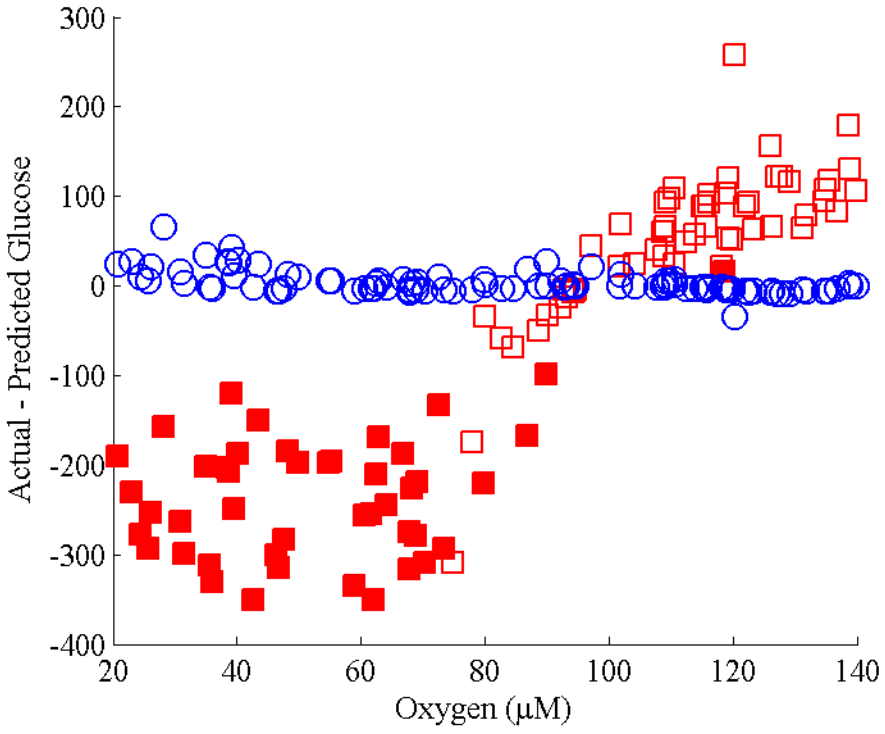

Figure 3.12 This graph shows the difference in actual and predicted glucose values for the results in Figure 3.11 as a function of oxygen concentration. Blue circles and red squares again represent, oxygen compensated and uncompensated glucose predictions, respectively. Markers that are filled in represent the presence of an erroneous measurement (see text).

Erroneous measurements were plotted by substituting 400 mg/dL for imaginary glucose predictions and 0 mg/dL for negative glucose predictions. Compensated values showed a near uniform variation across the range of oxygen concentrations with some increase at lower oxygen concentrations which is most likely due to a loss in range at the lower oxygen concentrations (Figure 3.8). The mean difference and standard deviation for oxygen compensated measurements was 3.3 and 12.8 mg/dL, respectively. Uncompensated values had a mean difference of -76.5 mg/dL and a standard deviation of 163.1 mg/dL. Uncompensated glucose predictions showed a linear trend with the highest accuracy occurring at 80 μM as expected. Predictions with less than 80 μM oxygen tended to be imaginary due to the low percent change of that calibration curve while predictions at higher oxygen concentrations showed a decreasing accuracy. It is expected that if calibration was performed at another oxygen concentration, the results would be similar where the highest accuracy should occur near the oxygen concentration at which calibration was performed.

In a second test, theoretical measurement error was also introduced into the system to see how this would affect *in vivo* glucose predictions. A pooled standard deviation (0.61 μs) was determined using the lifetime results in Figure 3.3 and applied to the lifetime response produced by the model. In addition, an equation for random uncertainty was applied to the same results to obtain an oxygen measurement standard deviation of 2.17 μM.[155]

When applied to the model, similar results were seen (Figure 3.13) when measurement error was introduced into the system as those made without measurement

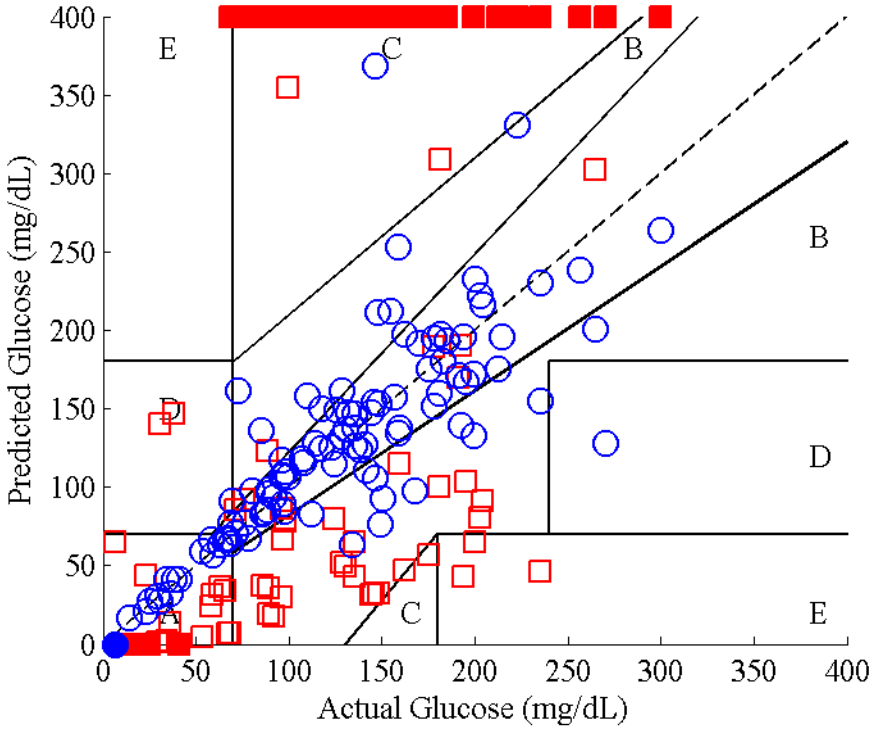

Figure 3.13 This Clarke error grid shows glucose predictions obtained from random oxygen and glucose values. Theoretical measurement error was also considered. Blue circles show oxygen compensated predictions and red squares show uncompensated predictions. Markers that are filled in represent negative or imaginary glucose predictions (see text). It should be noted that these values only represent the presence of an erroneous prediction and not an actual predicted glucose value.

error. Glucose predictions did become less accurate for both cases but oxygen compensated predictions again showed a higher accuracy than those made without compensation. One erroneous prediction (1 negative value) was made for compensated glucose predictions while 50 measurements (47 imaginary, 3 negative) were erroneous for uncompensated predictions. The trends in accuracy as a function of oxygen concentration also showed results similar to those in Figure 3.12 but with slightly lower accuracy overall. The average difference and standard deviation for oxygen

compensated glucose predictions was -0.9 and 41.2 mg/dL, respectively. Uncompensated predictions had a mean and standard deviation of -103.9 and 162.5 mg/dL, respectively.

3.4 Conclusions

The inaccuracy of enzymatic, glucose sensors due to variability in the ambient oxygen concentration was demonstrated *in silico*. This is a major concern for *in vivo* applications (*i.e.* self-monitoring of blood glucose levels) where oxygen levels are expected to vary. To overcome this issue, a technique for compensation using an oxygen dependent calibration curve was described where the appropriate calibration curve was selected based on ambient oxygen concentration. Using this approach, glucose predictions were found to be more accurate than uncompensated predictions over a wide range of ambient oxygen concentrations. Despite the extensive calibration that will be required *in vitro* before implementation *in vivo*, the improvement in accuracy outweighs this drawback. This oxygen compensation technique addresses a limitation of current enzymatic, glucose assays and could also be utilized to improve the accuracy of other enzymatic assays.

4. BACKGROUND ON TIME-RESOLVED MEASUREMENTS OF LUMINESCENCE*

As already mentioned, luminescence is an attractive transduction method for measuring sensor response due to its inherent measurement flexibility and sensitivity over other types of transduction, specifically electrochemical.[4, 156] Luminescent sensors have been reported for a variety of analytes including oxygen, pH, and temperature.[114, 157] The response of these sensors is typically determined by measuring the intensity, anisotropy, or lifetime of the luminophore following excitation.[24, 149]

In the past, intensity measurements have been primarily used to measure luminescent sensor response due its simplicity.[24, 114, 158] In order for intensity measurements to be utilized, they must be independent of any other factor except the concentration of the analyte.[159] However, this is not often the case leading to inaccuracies in analyte measurement. [24, 159] Many of these inaccuracies are attributed to the measurement of the intensity in relative units which are difficult to compare without some standard or reference measurement.[24] For example, reproducibility from instrument-to-instrument is often difficult to achieve due to variability within the hardware itself. In addition, fluctuations in light source intensity or detector sensitivity can lead to erroneous measurements.[24, 160-161] Errors can also arise from the sensors due to non-homogenous distributions, sensor-to-sensor variations in concentration, and photobleaching of the luminophore.[158, 162] Background signal caused by scattering or autofluorescence can also lead to inaccuracies.[24]

To reduce the instrument-related problems, several wavelength ratiometric approaches have been developed.[152, 163] These approaches either utilize a dual emitting dye where the peaks respond in opposite directions (i.*e.* the intensity at one wavelength increases while the other decreases) or two luminophores, one of which is an insensitive reference (*i.e.* remains constant) and the other is sensitive to the desired analyte (Figure 4.1).[164] Due to the self-referencing nature of these kinds of sensors, the results are generally more reproducible from instrument-to-instrument.[24] However, photo-bleaching is still a concern for two luminophore systems because the time-dependent rate can be different for each luminophore utilized.[24] Thus if one luminophore bleaches faster than the other luminophore, drifts in the ratiometric response will occur. Temperature-dependent quenching will also be different for each luminophore again leading to a drift in the response as the ambient temperature changes.[24] In addition, the

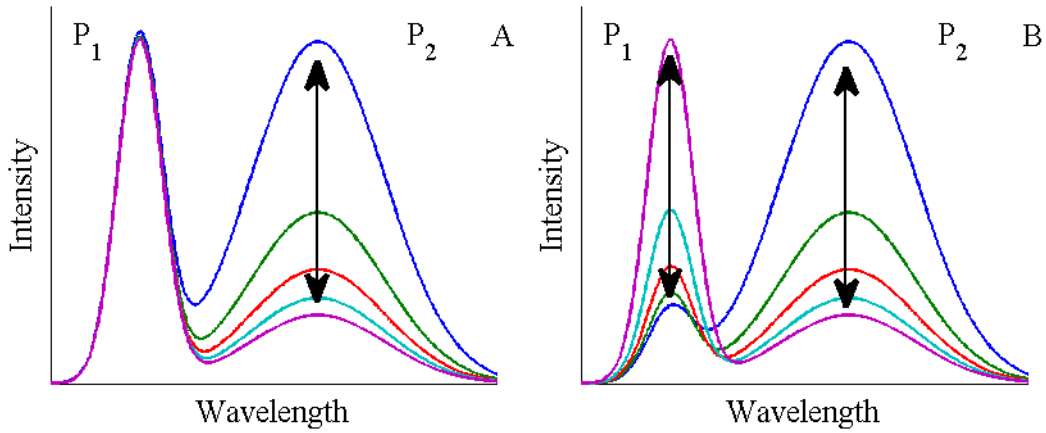

Figure 4.1 A) Diagram of an intensity-based ratiometric response where P_1 is the peak of an insensitive reference and P_2 is the analyte sensitive luminophore. B) Another intensity-based ratiometric response where both P_1 and P_2 respond to the analyte of interest but in opposite directions.

sensor-related issues discussed above (*e.g.* variations in concentration from sensor-to-sensor) will remain an issue with ratiometric systems utilizing two luminophores. Although this is less of an issue for dual-emitting or self-referencing luminophores, luminophores with the appropriate spectral and sensing properties may not be available.

Measurements of luminescence anisotropy can also be utilized by exciting a luminophore with polarized light.[24, 149] Analyte-dependent rotational diffusion of the luminophore allows measurements of the degree of polarization or anisotropy to be used for sensing applications.[24] Anisotropy can overcome some of the issues of intensity measurements; however, this technique is still susceptible to inaccuracies due to scattering and any diffusional restriction (*e.g.* rigid immobilization) of the dye will lead to a loss in sensitivity.[24]

Measurements of the luminescence decay rate or *lifetime* are of interest because they are not susceptible to the errors that hinder intensity and anisotropy measurements.[24] This is because the lifetime response if independent of the luminophore concentration and not sensitive to the optical parameters of the instrumentation.[24] In addition, background signal due to scattering or auto-fluorescence is often not an issue because these events are present for only a few nanoseconds while most luminescent indicators have longer lifetimes (tens of nanoseconds to greater than a millisecond).[24] Lifetime measurements can either be made in the time-domain (TD) with pulsed excitation light or in the frequency-domain (FD) with intensity-modulated light. TD-based approaches are attractive for *in vivo* measurements because they are less affected by short-lived scattered excitation light or tissue autofluorescence than FD

measurements. These background signals can be removed in the FD also, but require measurement at multiple frequencies which is time consuming.[149, 165-166]

In addition, the long lifetimes of the luminophores utilized for oxygen and glucose sensing allow luminescence decays to be recorded in a single measurement rather than re-built using time-correlated single photon counting TCSPC which is often used for imaging applications.[149, 161] The long lifetimes also prevent the need for deconvolution of the luminescence from the excitation signal or any instrument response.

Some of the more applicable lifetime calculation techniques will be discussed below, but further review of other lifetime calculation techniques for mono- and dual-exponential decays can also be found elsewhere.[149, 165, 167]

4.1 Numerical Analysis

The lifetime of a mono-exponential decay can be calculated using a variety of methods including linear and non-linear least squares analysis (LLS and NLLS, respectively), the phase-plane method (PPM), the maximum likelihood estimator (MLE), the maximum entropy method (MEM) and the rapid lifetime determination (RLD) method.[149, 167-170] Of these methods, NLLS is most often utilized but relies on several assumptions and can require extensive computational power making it unsuitable for real-time applications.[25, 149, 171-173] In addition, NLLS does not guarantee a suitable solution for the lifetime which can be dependent on the initial guess of the parameters for the fit.[25, 173] Accuracy can be improved by using weighted least-squares analysis whereby data points with lower standard deviation are given higher priority towards

fitting which is often done in cases where the standard deviation across the data set is variable but in a predictable manner.[174] However, when using a weighted approach, it is often assumed that the weights are known exactly which is usually not the case. If the data are improperly weighted, inaccuracies can occur.[175-176] A closed form solution for the lifetime can also be obtained by transforming the data logarithmically (after background subtraction) and using LLS analysis.[27, 173] Usually only a portion of the decay is analyzed after logarithmic transformation because errors can occur due to inaccurate baseline levels.[29, 177] Weighting of the response is typically utilized with this method which again must be chosen carefully.[178-179] Lifetime calculations using the Guggenheim method eliminate the need for background correction by plotting the logarithmic transform of the difference between equally-spaced, paired data points.[177] This and other numerical analysis techniques have given way to NLLS analysis, however.

More recently developed techniques tend to utilize window integration to perform lifetime calculation. This is done by dividing the decay data into separate bins or windows which are then summed.[171, 180] Integration can also be performed in real-time using CCD cameras.[181] Different methods utilizing window integration are discussed below.

4.2 Phase-Plane Method

The Phase-Plane Method (PPM) developed earlier by Demas *et al.* was one of the earliest methods to utilize window integration to calculate lifetimes.[182] This approach transforms data obtained using windows and determines the lifetime by finding

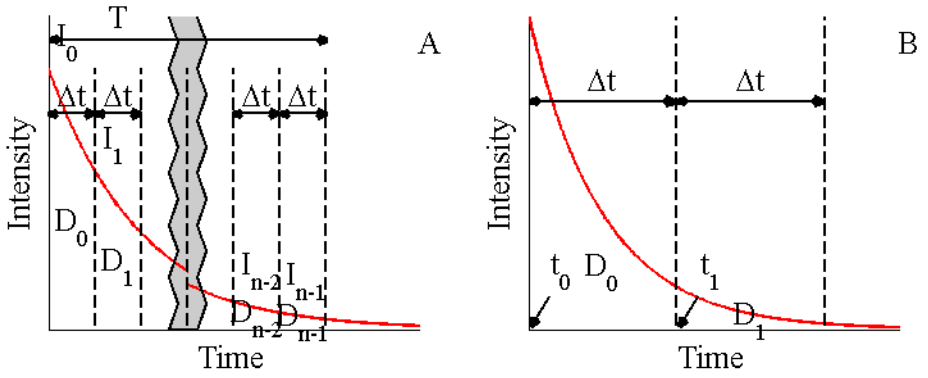

Figure 4.2 A) Multi-window technique utilized to determine lifetimes with the PPM and MLE methods. B) Representation of a two-window approach for RLD lifetime calculations. The variables t_n, D_n, and I_n refer to the start time, integrated intensity and initial intensity of the n^{th} window. The length of the window is represented by Δt.

the slope of a line (Figure 4.2A). Although this method has been used as a means of deconvolution from the excitation signal,[180, 182] it has also been adapted by Moore *et al.* for study of mono-exponential decays.[171] The primary equation of interest for this approach is:

$$W(t) = -\frac{1}{\tau}D(t) + k \qquad 4.1$$

where $D(t)$ is the integrated values for each window over time and $W(t)$ is approximated by averaging the D value on each side of the interval $((D_i - D_{i-1})/(2\Delta t))$. The plot of $W(t)$ vs. $D(t)$ gives data which can be fit using LLS to find the values for the lifetime, τ and the initial intensity, k. Error analysis of the PPM was performed by Greer *et al.*[180] They found the precision and accuracy of PPM to be similar to LLS but for mono-exponential decays only. Jezequel *et al.* were able to demonstrate lifetime measurements in the presence of scattering media by expanding the

method to examine bi-exponential decays.[183] They were able to show repeatable lifetime measurements when different levels of scattering were introduced.

4.3 Maximum Likelihood Estimator

Hall *et al.* developed the maximum likelihood estimator (MLE) approach to determine the lifetime of a probe using integration of several windows similar to PPM (Figure 4.2A).[184] In the equation below, the left-hand side consists of the lifetime, τ, and the pre-determined sampling parameters while the right-hand side is a function of the collected data:

$$1 + (e^{T/t} - 1)^{-1} - m\left(e^{\frac{mT}{t}} - 1\right)^{-1} = (D_t)^{-1}\sum_{n=1}^{m} iD_n \qquad 4.2$$

where m is the total number of windows, D_t is the total number of counts, D_n is the number of counts in the n^{th} window, and T is the total collection time. Once the data have been collected, an iterative solver is used to calculate the lifetime. This approach was found to provide faster calculations and produce similar results compared to NLLS. When the signal level was low, MLE even provided more accurate calculations than NLLS.[171, 179, 184-186]

4.4 Rapid Lifetime Determination

First introduced in 1984 by Woods *et al.*, the rapid lifetime determination or RLD method is able to calculate the lifetime of a decay using only two or three windows (Figure 4.2B).[29] The standard approach utilizes two windows to calculate the lifetime, τ, using:

$$\tau = \frac{\Delta t}{ln(D_1/D_2)} \quad 4.3$$

where Δt is the window length, and D_n is the integrated intensities for the n^{th} window.[27] If the background level is unknown and nonzero, a third window may be incorporated into the calculation.[28-29] Because iterative approaches are not utilized, this method is significantly faster than LS analysis, allowing real-time sampling of the luminophore lifetime.[27, 29] However, the accuracy of the lifetime calculation has been shown to be dependent on the length of the window with respect to the lifetime.[27, 187] Waters *et al.* developed a method to determine the optimal window length based on the mean expected lifetime for a dynamically changing luminophore to reduce the effects of this problem.[188] Sharman *et al.* also determined that overlapping the windows improves accuracy of the calculation.[181] Collier and McShane recently demonstrated a method that utilizes windows with dynamically changing lengths; compared to the static window lengths previously used. This real-time adjustment of windows leads to improved lifetime accuracies over a wide range of lifetime values.[153]

Following the development of RLD, several iterative approaches utilizing two windows have also been developed. Rather than implement both windows following the end of excitation, Chan *et al.* developed the Square-Wave RLD (SWRLD) method which applies one window during the excitation of the luminophore and one immediately following.[187] They found the precision of this method comparable NLLS and superior to the standard RLD approach. Chan *et al.* also developed a generalized RLD (GRLD) approach that utilizes two overlapping windows of unequal length implemented following probe excitation.[189] Again, this method showed improved

accuracy over standard RLD calculations. Both of these methods, however, require an iterative solver which leads to increased computation time compared to RLD.[153]

Moore *et al.* compared several of these window-based approached and found the precision of MLE, PPM, and GRLD was much better than standard RLD.[171] They also showed that PPM is susceptible to systematic errors at large sampling times which can be reduced by increasing the number of windows used. MLE was found to have consistently lower standard deviations than the other methods; however, both MLE and RLD were susceptible to errors due to non-zero baselines.

4.5 Dual-Exponential Lifetime Decay Response Measurement Techniques

Much like single sensor responses, NLLS is often used to calculate lifetimes when multiple emitters are present; in this case, multi-exponential fits are applied (similar to equation 12). In addition, the luminescence acquisition method required for multi-exponential response in the TD is often not different than the method used for mono-exponential responses, making them easier to implement than multi-luminophore FD approaches. However, in order to distinguish the lifetimes of multiple luminophores, they need to be temporally-distinct.[181]

Hradil *et al.* developed one of the first methods to utilize temporally-distinct luminophores for dual lifetime calculations that does not require multi-exponential LS analysis.[190] This method was utilized for temperature compensation of an oxygen sensing film. In order to resolve the response of both luminophores, the decay time of the longer-lived luminophore is approximately three orders of magnitude longer than the other luminophore (Figure 4.3). This is necessary in the TD in order to ensure the

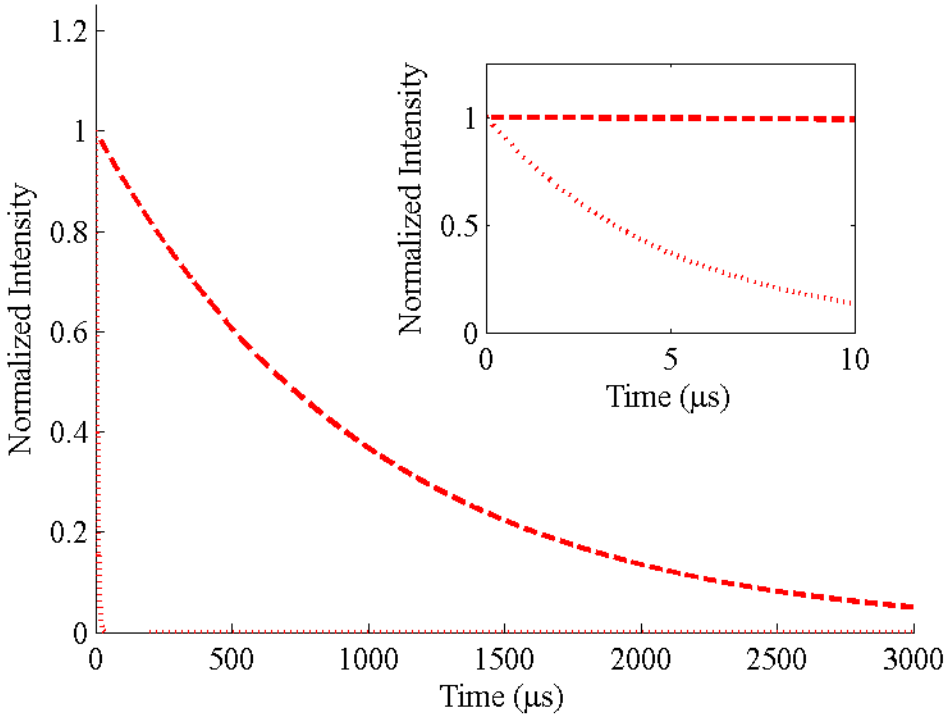

Figure 4.3 Depiction of TD decays for two temporally-distinct dyes with lifetimes of 5 and 1,000 μs. Inset is of the same decays but at a smaller period to show the decay of the shorter-lived luminophore and the nearly constant signal of the longer-lived luminophore.

contribution from τ_2 is constant while measuring the response of τ_1 and while measuring the response of τ_2, the response of τ_1 has decayed to zero. The response of the longer-lived luminophore is sampled after a delay to prevent any contamination from the shorter-lived luminophore. NLLS is then used to determine each lifetime.

In addition to NLLS, the RLD approach has been also been expanded for multi-exponential decay calculations by Sharman *et al.*[181] Similar to RLD for mono-exponential decays, two windows for each luminophore are used and are applied either contiguously or overlapping (Figure 4.4). The ratio of the τ_2 to τ_1 for this approach,

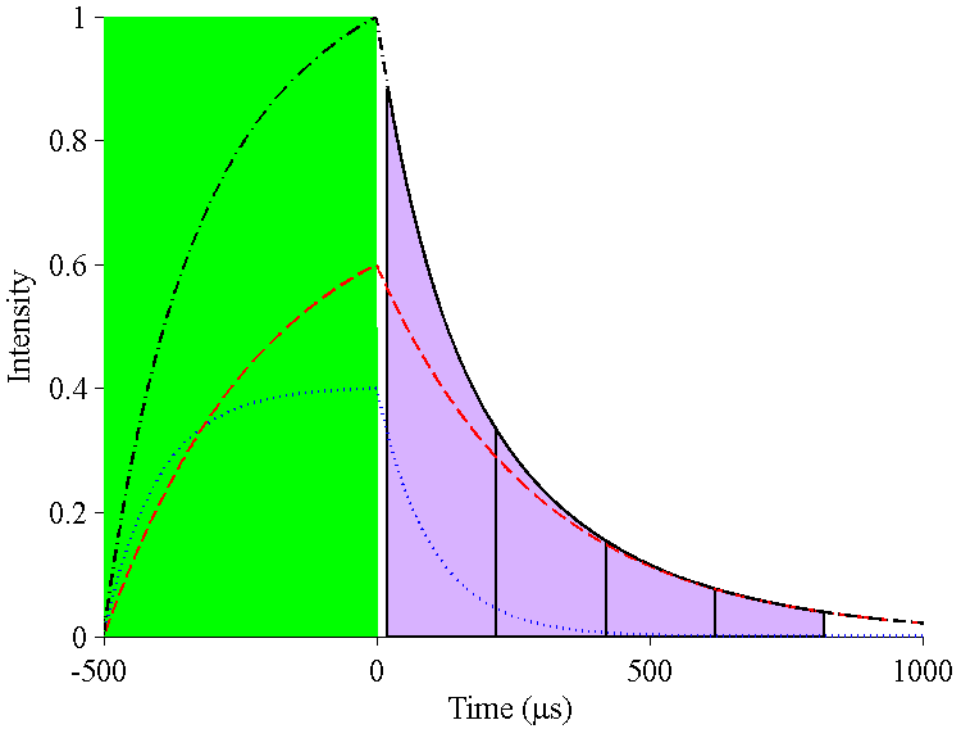

Figure 4.4 Example of a contiguous, equi-width window implementation of dual RLD lifetime calculations.

however, needs to be at least 2; the precision of the measurement is reduced as the lifetimes get closer.[181] The calculations for this dual RLD approach, however, are more complicated than the traditional RLD calculation and the method seems to be susceptible to measurement noise.[191]

Another method that utilizes the principles of RLD is the Dual Lifetime Determination (DLD) method developed by Nagl *et al.*[156, 162, 192] Similar to the scheme used by Hradil, the probes must be temporally-distinct; however, this method utilizes the standard RLD calculation to determine the lifetime rather than NLLS. Two pairs of windows are required (one for each lifetime calculation), where the second pair is

applied following decay of the shorter-lived luminophore to zero. It is important to note that the longer-lived luminophore does not necessarily give a constant signal during measurement of τ_1 as long as the mixed signal behaves monotonously with regards to the analyte of interest; this reduces the temporal-distinction requirements of the luminophores. The response was also shown to be heavily dependent on the window width utilized.[156] Stich *et al.* applied this method for oxygen and temperature sensing while also implementing a spectrally separated pH probe to measure three analytes at once.[192]

Becker *et al.* have developed a unique method to simultaneously record the response of a fluorescent probe and a phosphorescent probe.[193] Using a pulsed laser

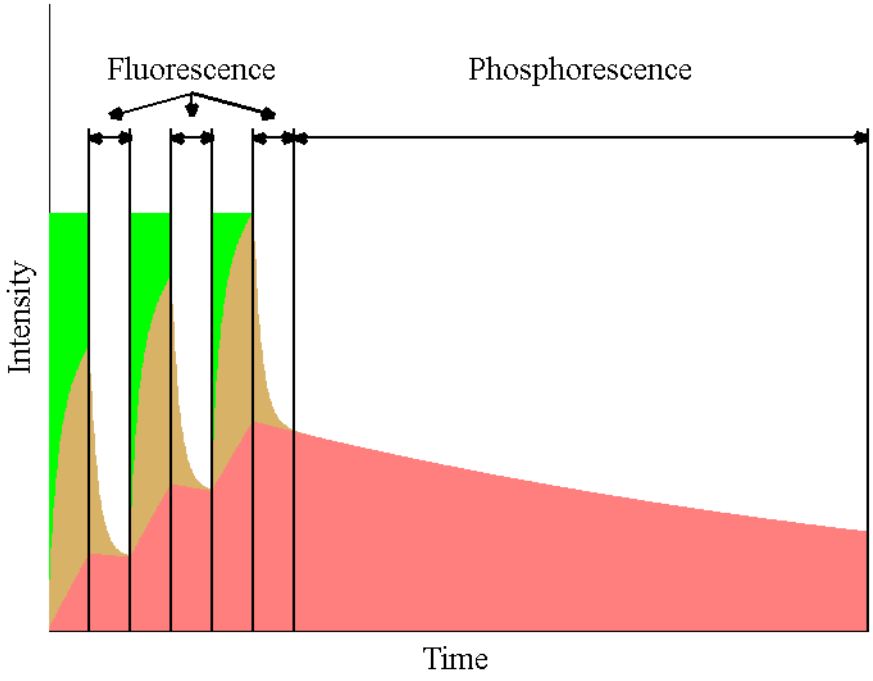

Figure 4.5 This is a depiction of the pulsed excitation and emission of a dual fluorescence and phosphorescence measurement.

with a high repetition rate, they were able to excite both probes simultaneously (Figure 4.5). Between excitation pulses of a pulse train, fluorescence decay measurements are made (again assuming constant signal from the phosphor). During the pulse train, however, phosphorescence steadily builds up due to its long decay time. After completion of the pulse train, phosphorescence measurements are made. Lifetime calculations are then made using NLLS.

5. DYNAMIC RAPID LIFETIME DETERMINATION*

Luminescent sensing and characterization have become widely researched areas in biomedical, environmental and food industries because of their ability to provide greater sensitivity and measurement flexibility when compared to electrochemical analysis schemes.[4, 156] In the past, intensity measurements have been predominantly used to measure analyte concentrations or physical properties; however, these methods are susceptible to many sources of error including photobleaching, drift in light source intensity, and variations in dye concentrations from sensor to sensor.[156, 194] These issues can be overcome by measuring the rate of luminescence decay or *lifetime* which is independent of the intensity (see Chapter 4 for more details).[195-196]

Although lifetime measurements can be made using either time-domain or frequency-domain techniques, the former can be advantageous because of its ability to easily eliminate scattering and shorter lifetime fluorescence from calculations. For example, many proteins found in the body, including collagen and elastin, are known to emit nanosecond lifetimes which can effect lifetime calculations of the dye. In addition, time-domain methods have been shown to have a higher precision than frequency-domain methods especially at lower intensities.[195, 197] Traditionally, linear and non-linear least-squares fittings have been used to determine the lifetime during time-domain measurements but these methods require extensive computing power due to the large number of iterations required to arrive at an accurate estimate.[25, 173] The lifetimes calculated with fittings are also dependent on the initial guesses for each parameter.[25] If

the initial guesses are not relatively close to the true values, convergence of the fit will take more time. A complex fit can also lead to the selection of the fit parameters at their local minima leading to biased estimates.[25]

To overcome these limitations, several groups have investigated alternative processing techniques using gate- or window-sums to calculate lifetimes.[27-29, 181, 188-189] The rapid lifetime determination (RLD) method utilizes two windows of equal width applied over the decay of a luminophore.[27] By summing over the width of the window, the lifetime can be determined using:

$$\tau = \frac{\Delta t}{\ln(W_1/W_2)} \qquad 5.1$$

where Δt is the window width and W_1 and W_2 are the sums for windows 1 and 2, respectively (Figure 5.1). This calculation is much faster than the traditional fitting methods but can still be susceptible to errors which occur because a single static window width is oftentimes not optimal for lifetimes much shorter or longer than the widths.[27-28, 181, 188] For example, this becomes especially problematic for sensing applications where dynamic lifetimes of a wide range are utilized. In order to overcome this problem, several methods have been developed in order to appropriately select the window width and increase the accuracy of lifetime calculations. These methods maintain the advantage of speed over NLLS but are still limited in range because of the static window width.[27-28, 181, 188]

The original two window-based method, referred to here as the contiguous RLD (CRLD) method, utilizes windows of equal width run back-to-back to calculate the

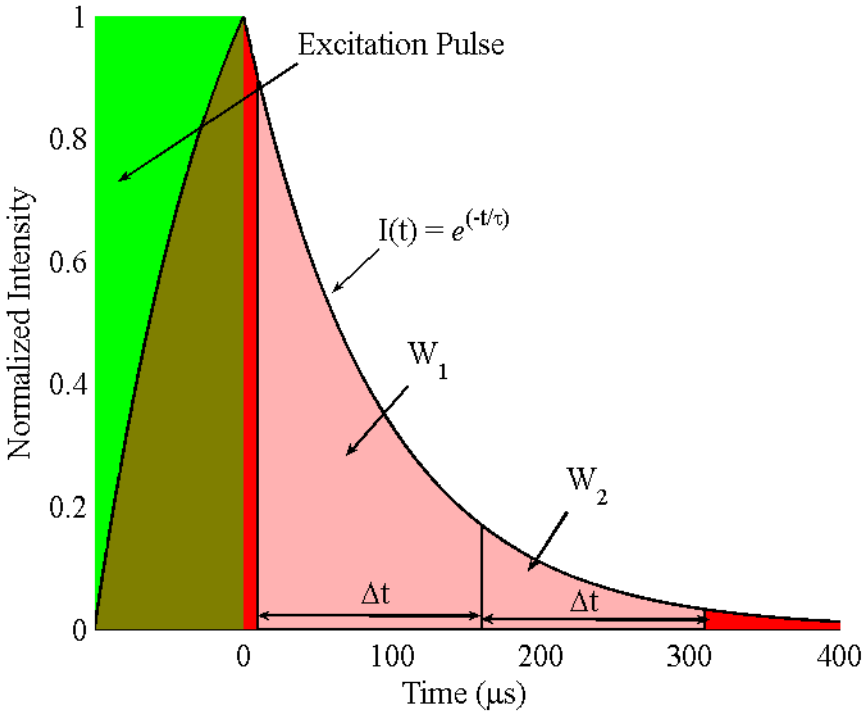

Figure 5.1 Diagram of the basic RLD lifetime determination approach with contiguous windows of equal width.

lifetime.[27] The second window of the overlapping RLD (ORLD) method, however, begins before the first one ends.[181] Both of these methods utilize Eqn. 1 to calculate the lifetime. However, the generalized RLD (GRLD) method, utilizes overlapping windows of different width which requires a different equation to the calculate lifetime.[189]

For the current work, rather than use a window with a static width, a computer-based algorithm to dynamically determine the appropriate window width is evaluated. After collecting the data, I hypothesize the lifetime response will then be calculated with increased accuracy compared to those methods with a static window width. In practice this method will only be limited by the sampling frequency and the number of data

points recorded over time, but in theory this method could calculate the lifetime of *any* response. As with NLLS, however, a larger range of possible lifetimes will lead to an increased number of iterations performed and increased computation time. This approach is based on the original two-window RLD where the windows are contiguous and of equal width, but will be applicable to a much more extensive range because the window widths are allowed to change dynamically as the lifetime changes.

5.1 Theory

The optimal window width for lifetime determination is usually described by the ratio of the window width, Δt, to the lifetime, τ.[27-28, 181, 189] Ballew and Demas initially proposed an optimal ratio for contiguous RLD near $\Delta t/\tau = 2.5$ and other groups later describe an optimal region from 1 to 3 $\Delta t/\tau$.[27, 181, 189] To implement DRLD, the ratio of window-sums can be correlated to $\Delta t/\tau$ by re-arranging Eqn. 1:

$$W = \frac{W_1}{W_2} = \mathrm{e}^{\frac{\Delta t}{\tau}} \qquad 5.2$$

where W is the ratio of the window-sums. The optimal range for $\Delta t/\tau$ can then be plugged into this equation to get the corresponding optimal range for W. When performing the calculation for data that exhibit significant changes in τ, the window widths should be adjusted for every lifetime calculation until W is within the optimal range or another termination condition is met.

To implement a dynamic window change, the window width can be adjusted by multiplying the previously calculated lifetime by a value that lies in the middle of the chosen optimal range of $\Delta t/\tau$. The window size is initially set to a small value so that a

maximum window change is only used for increases in window width. Maximum window widths and maximum window changes are also implemented to prevent programming errors. Protection from negative W values, which can occur when the decay shows low signal-to-noise ratio, should also be implemented in this algorithm. The lifetime is re-calculated until W is in the optimal range, the maximum width is reached, or a maximum number of loops has been reached. A flow-chart of the entire algorithm can be seen in Figure 5.2 and an example of the code can be found in Appendix C.

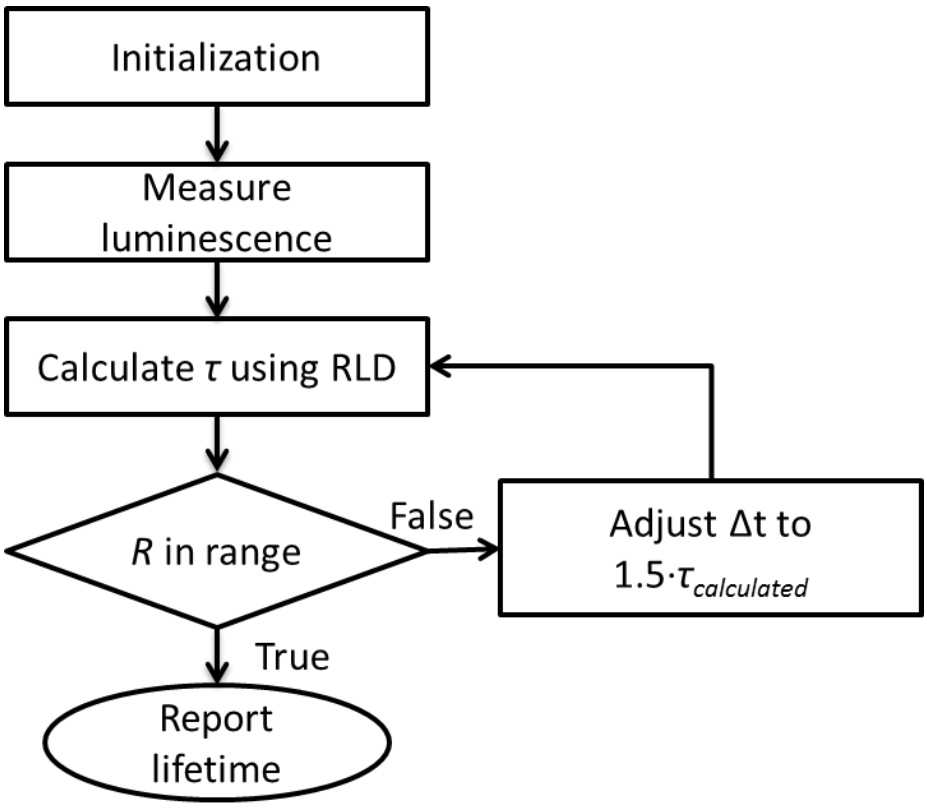

Figure 5.2 Simplified low chart of dynamic windowing algorithm operation.

5.2 Experimental Details

5.2.1 Lifetime Techniques

In addition to DRLD and NLLS, the three other static windowing methods described previously were used for comparison of lifetime calculations. The width of the windows for CRLD was set to $0.25\bar{\tau}$ which was previously determined to be the optimal width for this method where $\bar{\tau}$ is the mean expected lifetime.[188] Two variations of the ORLD method were utilized to calculate the lifetime. Both utilize a second window start time of $0.25\bar{\tau}$ but the window widths were to set to $0.5\bar{\tau}$ and $1\bar{\tau}$ for ORLD1 and ORLD2, respectively. For GRLD, the equation below was adapted from the original equation to incorporate an initial delay of the window start times:

$$\frac{W_2}{W_1} = \frac{e^{-Q(X+Y+P)} - e^{-Q(X+Y)}}{e^{-Q(X+1)} - e^{-QX}} \tag{5.3}$$

where X is the fractional delay of W_1 in terms of Δt, Y is the fractional delay of W_2 (relative to W_1) in terms of Δt, and P is the width of W_2 in multiples of Δt. Using an iterative solver, Q is solved for and then plugged into:

$$\tau = \frac{\Delta t}{Q} \tag{5.4}$$

to obtain a lifetime. The width of W_1 or Δt was set to $0.25\bar{\tau}$ because an optimal value was not previously determined. Other iterative window-summing methods for lifetime calculation are available but often require 10 or more windows. This number of windows means greater complexity and increased computation. These methods will not be compared here but have been elsewhere.[171, 185-186] For calculations performed, an initial delay of window start times was set to 0.8 μs in order to eliminate back-scattered

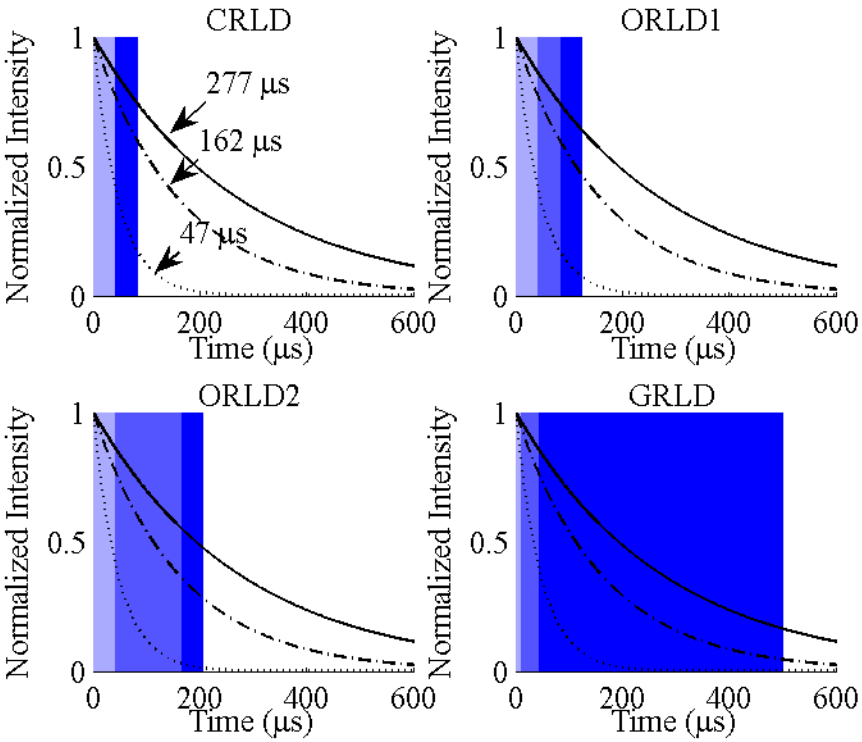

Figure 5.3 Theoretical implementation over three different lifetimes of the four static window methods utilized to compare to DRLD. W_1 is represented by a light colored box and W_2 is represented by a dark colored box. Any overlap of the windows is represented by a shade in between the two window colors.

excitation light from the lifetime calculations. This delay represents a single data point collected for each decay (based on the sampling rate) and will not affect lifetime calculations or optimal window widths. Theoretical implementation of each of these methods can be seen in Figure 5.3.

5.2.2 Modeled Lifetime Responses

Initial modeling investigated the possible calculation errors in static window width methods. If a dynamic windowing algorithm is not used and the lifetime response changes dramatically, a large error may be observed. From our calculations, if the

lifetime response was 25 μs and the windows were 37.6 μs ($\Delta t/\tau$ = 1.5) the calculated lifetimes would have a very good accuracy and repeatability as indicated by a mean modeled lifetime calculation of 24.8 μs and a standard deviation of 0.322 μs (n = 10, SNR = 10). However, if the lifetime were to suddenly change to 250 μs, the precision of the measurement is greatly reduced as seen by modeled calculations with a mean lifetime of 264.2 μs and a standard deviation of 39.2 μs (n = 10, SNR = 10).

To test the algorithm described above, a lifetime profile was designed in MATLAB (Mathworks, Inc.) to simulate a real-time response and test the ability of different window-summing lifetime calculation methods to calculate a range of lifetimes. A decay for each lifetime was simulated with a SNR of 10 (Figure 5.4), and each of the five methods were used to calculate τ. The residuals and R^2 values for each method were also calculated to determine the accuracy of each method.

5.2.3 Custom Lifetime Measurement System

A custom time-domain lifetime measurement system was developed to experimentally demonstrate the DRLD technique. For luminophore excitation, a fiber optic green LED (530 nm peak, Industrial Fiber Optics, Tempe, AZ) was utilized with a driver circuit (see Appendix A) to improve the operating speed (ns rise and fall times) of the diode. The circuit consisted of a transistor and resistors and capacitors. Luminescence detection was performed using an avalanche photodiode module (APD, C5460, Hamamatsu). Two plano-convex lenses (LA1951-A, Thor Labs) were used to collect the luminescence from a bifurcated fiber bundle and focus it onto the active area of the APD. A long-pass filter (3RD620LP, Omega Optical) was also used to reduce

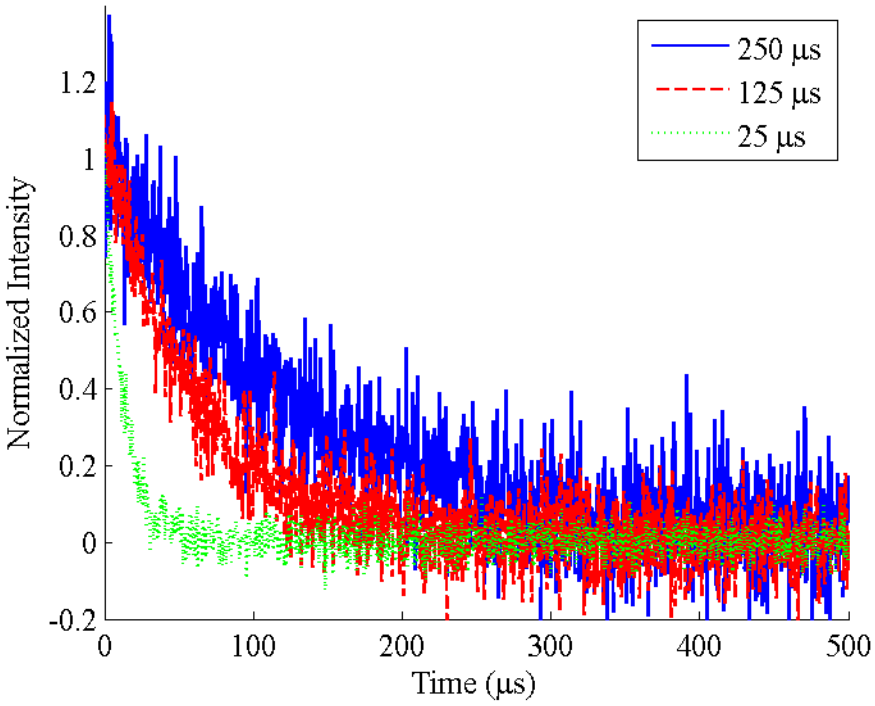

Figure 5.4 Examples of modeled luminescence decays with an SNR of 10.

interference from back-scattered excitation light. A data acquisition board (USB-6259, National Instruments) was used to provide an excitation signal to the LED and collect the emission signal with a sampling rate of 1.25 MHz. Custom control programs were also developed using LabVIEW development software (National Instruments). A diagram of the system and its components can be found in a previous publication as well as in Appendix A.[198]

During dynamic response testing and decay collection, a 40 Hz rectangular excitation signal was used to excite the luminophore and 40 raw decays were summed to yield one decay for lifetime calculations. A background signal was also collected at 40 Hz for 1 second before each excitation and subtracted out of the summed decay. A total

of 25 summed decays were obtained for each steady-state response. The summed decays with background subtracted out will henceforth be referred to only as *decay*s.

To implement DRLD, the initial window width was set to 10 μs and the maximum number of loops was set to 10. The maximum window change allowed for one loop was set to 50 μs and the maximum window width allowed was set based on the 1000 μs total acquisition time. The windows were also delayed 0.8 μs from the end of the excitation pulse in order to reduce error from back-scattered excitation light. Most importantly, the range of $\Delta t/\tau$ was chosen to be from 1 to 2, giving W the corresponding range of 2.7 to 7.4.

5.3 *In Vitro* Testing and Comparison

Oxygen sensors were exposed to six different oxygen concentrations in random order during testing. Although real-time calculations were obtained using the proposed dynamic windowing algorithm (data not shown), 25 luminescence decays for each oxygen concentration were also saved for post-processing to compare the accuracy and computation time required for the various methods. As a standard for comparison, lifetimes were calculated with a mono-exponential fit using a non-linear least-squares (NLLS) solver. These lifetimes were determined first and utilized to determine $\bar{\tau}$ by averaging the lifetime at the minimum and maximum concentrations measured. This value was used for other lifetime calculation methods to determine the appropriate window width. Mean R^2 values were obtained for the fittings at each oxygen concentration. The SNR at each concentration was also determined by dividing the mean NLLS lifetime by the standard deviation. The NLLS values were considered as

Table 5.1 Calculated R^2 values for the simulated profile.

Method	R^2 for Simulated Profile
NLLS	--
DRLD	0.996
CRLD	0.888
ORLD1	0.966
ORLD2	0.989
GRLD	0.992

the archetype lifetime measurements and were used to determine the accuracy of the other methods. Programs for each different lifetime calculation were written using MATLAB and computation time of each lifetime calculation was determined using the *tic* and *toc* functions.

5.3.1 Oxygen Sensors and *In Vitro* Experimental Setup

Porous, amine-modified silica microspheres (YMC America, Inc., 10.3 μm average diameter, 13.1 nm average pore diameter) were used as the sensor matrix. Palladium(II) meso-Tetra(4-carboxyphenyl) porphine (PdP, 710 nm peak emission) from Frontier Scientific was utilized as an oxygen-sensitive luminophore to create oxygen sensors by covalently coupling to the silica microspheres using a procedure described elsewhere.[152] The particles were then immobilized on a glass slide for testing. Two mass

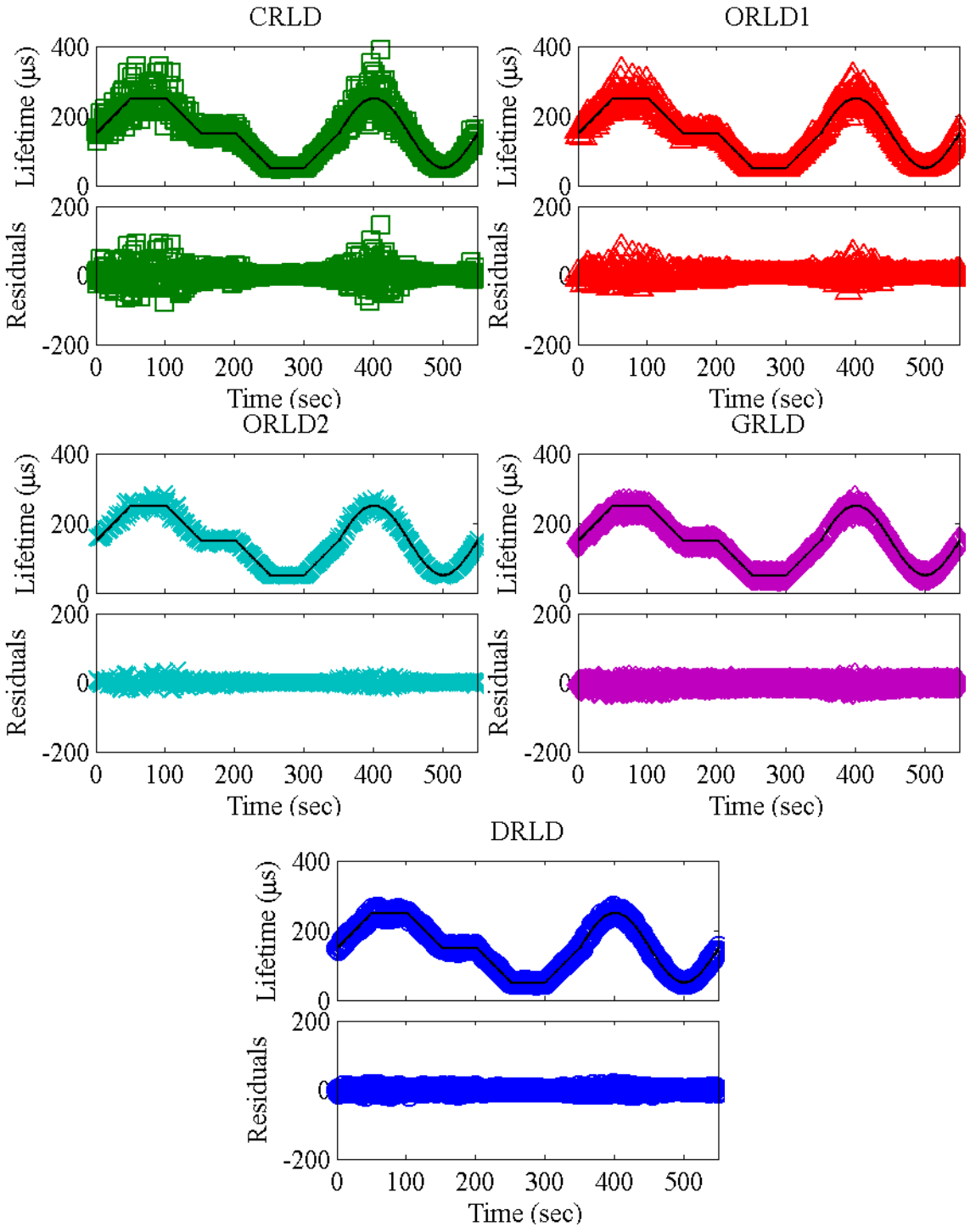

Figure 5.5 The lifetimes calculated for each window-sum based method in response to a simulated profile can be found in the top portion of each graph while the residuals of those calculations can be found on the bottom. The black line represents the simulated lifetime for each point in time.

flow controllers and a controller (1179A and PR4000, MKS Instruments) were used to mix nitrogen and compressed air as a means to control dissolved oxygen concentration in the phosphate buffered saline solution which was used to perfuse oxygen sensors and validate the response. An amperometric oxygen sensor was also used to monitor the dissolved oxygen concentration (PA2000, Unisense). A peristaltic pump (Masterflex 7550-50, Cole Parmer) was used to deliver the buffer solution to the sensors.

5.4 Results and Discussion

From the simulated response profile (Figure 5.5), all of the methods appear to be

Table 5.2 Lifetimes calculated using different window-summing techniques for simulated decays with different SNR. Values in parentheses represent one standard deviation for *n*=10.

Lifetime (μs)	SNR	CRLD	ORLD1	ORLD2	GRLD	DRLD
50	5	49.89 (2.52)	48.58 (1.90)	50.06 (1.68)	49.00 (3.17)	50.61 (2.83)
	10	50.65 (1.79)	50.31 (0.97)	49.64 (1.15)	49.84 (1.15)	50.16 (1.56)
	20	50.05 (0.65)	50.05 (0.47)	49.85 (0.27)	49.04 (0.49)	49.93 (0.45)
150	5	151.75 (14.69)	150.3 (13.24)	145.88 (5.07)	144.72 (5.33)	148.09 (6.24)
	10	143.55 (13.39)	152.49 (7.8)	149.98 (4.56)	146.34 (3.93)	148.89 (4.9)
	20	150.91 (3.74)	150.07 (2.74)	150.69 (0.98)	147 (1.02)	149.5 (1.12)
250	5	305.99 (119.69)	238.65 (44.99)	241.85 (16.66)	238.64 (6.49)	253.52 (8.7)
	10	263.71 (56.8)	260.81 (36.11)	257.05 (13.25)	241.24 (8.81)	246.99 (7.61)
	20	257.01 (13.51)	252.7 (7.14)	251.61 (5.34)	241.7 (1.96)	249.99 (2.64)

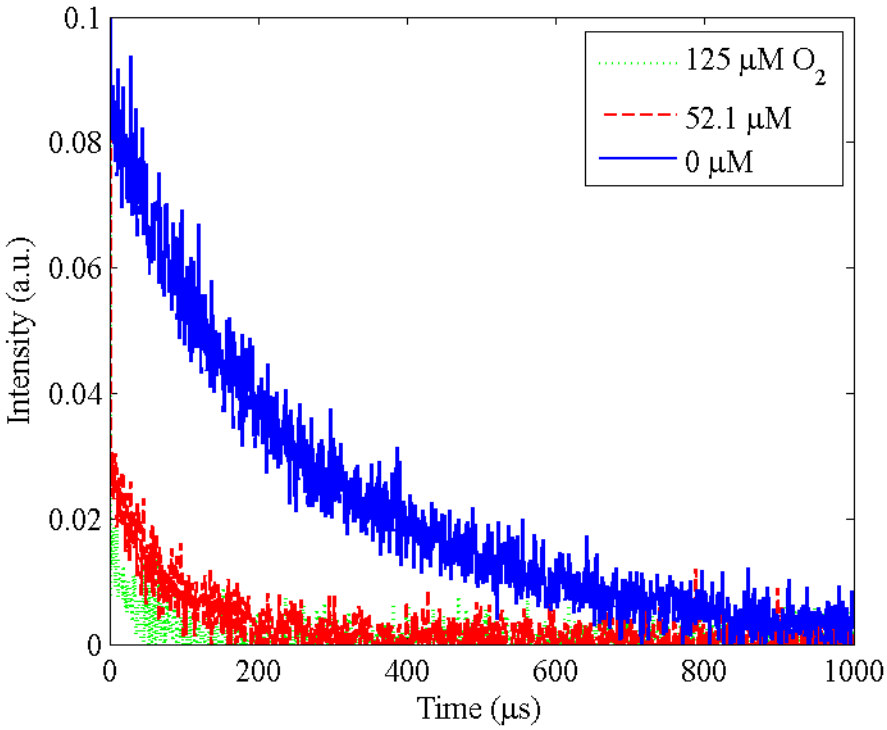

Figure 5.6 Example decays obtained from the custom lifetime measurement system for each oxygen concentration tested.

very accurate at low oxygen concentrations; that is, when the windows are able to cover most of the decay. However, at higher oxygen concentrations, DRLD and GRLD were the only methods to keep a high accuracy, as indicated by the high R^2 values (>0.99) for both methods (Table 5.1). The decrease in accuracy at higher lifetimes is a result of the large amount of neglected data, as suggested by Figure 5.3. The original window-sums technique, CRLD, had the worst accuracy out of all of the methods and reinforces the limitation of fixed window widths. This initial testing suggested that DRLD would be able to perform well under dynamic testing conditions.

Table 5.3 R^2 values for NLLS exponential fittings of lifetime decays and calculated SNR at each concentration. Percent difference from NLLS for the different window-summing methods is also shown for each oxygen concentration.

$[O_2]$ (μM)	R^2	SNR	NLLS Lifetime (μs)	Percent Difference from NLLS				
				DRLD	CRLD	ORLD1	ORLD2	GRLD
0	0.97	43.2	277.07	0.680	-15.4	-13.5	-11.8	-10.0
27.3	0.89	22.6	117.28	2.50	-10.6	-8.61	-4.68	-2.43
52.1	0.78	15.7	91.48	0.295	-13.0	-9.30	-4.87	-0.420
76.4	0.56	8.95	62.24	8.21	-3.77	-1.44	5.65	5.42
101	0.51	6.45	58.45	1.49	-8.47	-2.35	2.13	2.34
125	0.33	5.24	46.84	2.13	-1.56	-1.73	2.89	-5.38

The results from simulations that tested the effects of SNR can be found in Table 5.2. As expected, increasing the SNR leads to a decrease in the variability for each window-sum lifetime calculation method. However, as suggested by the results in Figure 5.5, this does not mean that the accuracy of the calculation increases. For example, the GRLD calculations for the 250 μs decay were not within one standard deviation of the actual lifetime for any SNR. The DRLD method, however, was always within one standard deviation of the actual lifetime and showed variability that was the same order of magnitude or less than the other methods. The variability for higher lifetime values was generally less than the other window sum methods with equal window width and more accurate than the GRLD method. This suggests that the DRLD method is better suited to determine the lifetime response for a range of values.

Using decays experimentally obtained using the custom lifetime measurement system (Figure 5.6); the lifetimes were calculated for each method and plotted for comparison (Table 5.3, Figure 5.7). It appears that the lifetimes calculated from the real-time decay data follow the trends observed from to the simulated profiles. The NLLS calculations did not have very high R^2 values at higher oxygen concentrations due to increased quenching of the dye's luminescence intensity which lead to a lower SNR (Table 5.3). From these fittings, $\bar{\tau}$ was found to be 162 µs. When comparing the window-summing techniques, DRLD showed a much higher accuracy than the other methods and was not significantly different than NLLS lifetimes ($\alpha = 0.05$). The other

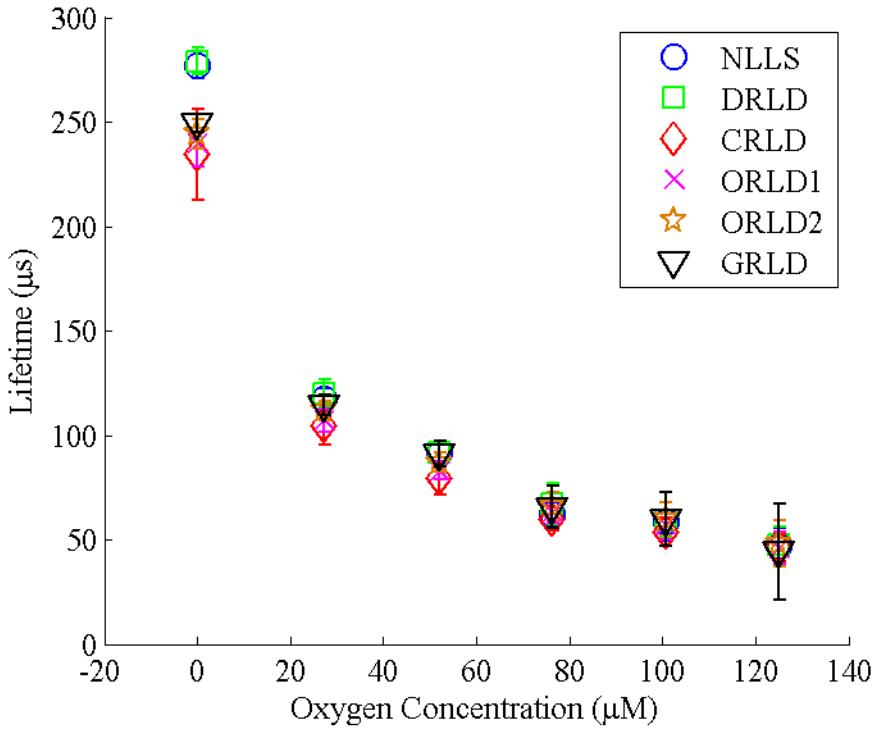

Figure 5.7 Lifetime response profile of the different window-sum methods compared to the lifetime calculated using traditional fittings. Error bars represent 95% confidence interval with n=25.

methods tended to underestimate the lifetimes at lower oxygen concentrations. GRLD did not show the high level of accuracy expected, especially at 0 μM oxygen, and the confidence intervals (uncertainty) increased with oxygen concentration. Neither of these observations agrees with modeling results. The high mean R^2 value for the NLLS calculation at 0 μM suggests that the fitting calculation is correct and the decrease with increasing oxygen levels is most likely due to low SNR from the decays obtained. It is important to appreciate that the accuracy of all static window methods is expected to decrease for a larger range of oxygen values. Although larger windows can be utilized for GRLD to increase accuracy at lower concentrations, it would most likely result in decreased accuracy at higher concentrations. The accuracy of DRLD will most likely increase further with a decrease in the optimal range of W but this could lead to an increase in computation time.

Following investigation of lifetime accuracy, the mean computation time was determined for the same set of data (Table 5.4). As expected, the non-iterative methods were found to be much faster than the iterative methods. The speed of DRLD, CRLD, and ORLD is two orders of magnitude greater than GRLD and four orders greater than NLLS. This lifetime calculation speed will allow these window-summing techniques to overcome their reduced accuracy by making more measurements in the same period of time. For example, with high speed excitation and collection, it could be possible to make over 100 DRLD lifetime measurements in the time it takes to make 1 NLLS measurement.

The speed and accuracy of DRLD has been shown capable of measuring a wide

Table 5.4 Real-time computation data for each window-based lifetime measurement technique. Values in parentheses represent standard deviation with $n = 25$.

Method	Mean Computation Time (ms)
NLLS	307 (65.6)
DRLD	0.197 (0.043)
CRLD	0.143 (0.045)
ORLD1	0.137 (0.010)
ORLD2	0.149 (0.055)
GRLD	13.6 (0.200)

range of lifetimes for a common oxygen sensing system. These calculations displayed a high degree of accuracy and precision over a variety of oxygen concentrations. The DRLD technique can be easily implemented with a wide variety of current and future sensor technologies for analyte measurement.

5.5 Conclusions

After investigation, DRLD was found to be more accurate than other window-summing lifetime calculation techniques with fixed window sizes when a wide range of lifetime values were considered. For the static window-summing methods, it is necessary to know beforehand the average expected lifetime to make accurate lifetime predictions. In contrast, DRLD is always accurate because it adjusts the window size and, despite this iterative approach, it is still more than one thousand times faster than traditional NLLS calculations. It is noteworthy that this algorithm may also be used with charge-coupled device (CCD) detectors with the window change not occurring until the

next lifetime measurement. This dynamic windowing algorithm can be implemented additional degrees of freedom, such as with overlapping windows in order to increase the optimal range of $\Delta t/\tau$ or with a three-window-sum calculation which does not require the background signal to be measured beforehand.[28, 181] With the aid of current microprocessor technology, it is anticipated that this method can be utilized within numerous sensing applications to enable accurate dynamic lifetime predictions using low-cost mobile devices.

6. DUAL DYNAMIC RAPID LIFETIME DETERMINATION

Luminescent sensing has become an area of interest in a variety of industries due to the greater sensitivity and measurement flexibility offered over other measurement methods including electrochemical. [4, 156] Oftentimes, multiplexed sensors or multi-sensors capable of measuring several analytes are needed for diagnostic and/or compensation purposes.[26] For example, temperature compensation is often needed of luminescent oxygen sensors.[162, 190, 192, 199-206] A key issue of multiplexing, however, is the separation of the individual sensor responses.[26] In the past, sensors capable of monitoring multiple analytes or multi-sensors were measured using intensity measurements; however, spectral cross-talk or overlap must be avoided.[26] Finding luminophores with adequate sensitivity, selectivity, and stability while still maintaining this spectral distinction may be difficult.[207] Even if appropriate luminophores are found, additional optical hardware will be required in order to separate the emission signals and/or excite the respective luminophores. In addition, intensity measurements are susceptible to errors due to photobleaching of the luminophore, optoelectronic drift, or variations in luminophore concentrations from sensor-to-sensor (see Chapter 4 for more details).[24, 114] Luminescence lifetime measurements are able to overcome these problems by determining the rate of luminescence decay using temporally-resolved measurements in the time- or frequency-domain (TD and FD, respectively). Advances in technology in recent years have allowed these types of measurements to become more common. [24]

Several methods have already been reported which temporally-resolve the response of multiple sensors with distinct lifetimes. Although multi-sensor lifetime

measurements can be made by optically filtering the signal from spectrally-distinct luminophores, this again requires spectrally-distinct luminophores.[162] As an alternative, many TD and FD methods have been developed which utilize luminophores with distinct decay times.[156, 162, 190, 192] These and other approaches that utilize temporal-based measurements have been recently reviewed elsewhere; only dual lifetime calculation techniques will be discussed herein.[165]

Multi-lifetime calculations in the frequency-domain (FD) require phase or modulation measurements at multiple frequencies. Non-linear least-squares analysis (NLLS) is used to fit the frequency dependent response data and determine the lifetimes.[149] Fittings, however, are computationally intense and dependent on the initial guesses which can be an issue for highly sensitive luminophores where the lifetime and intensity are expected to have a wide dynamic range.[25] The increased computational intensity can affect the speed of calculation and thus the real-time measurement capabilities. In addition, FD calculations can suffer from errors *in vivo* due to scattered excitation light and tissue autofluorescence. TD measurements, however, can easily remove these short-lived signals (typically ≤10 ns) by delaying the lifetime calculation of the longer-lived luminophores until after these events have decayed to zero.

In the TD, the decay data obtained are typically fit using NLLS to a multi-exponential curve:

$$I(t) = k_1 e^{-t/\tau_1} + k_2 e^{-t/\tau_2} \qquad 6.1$$

where k_1 and τ_1 refer to the initial intensity and lifetime of the response of the luminophore with a shorter lifetime, L_1. Similarly, k_2 and τ_2 describe the response of

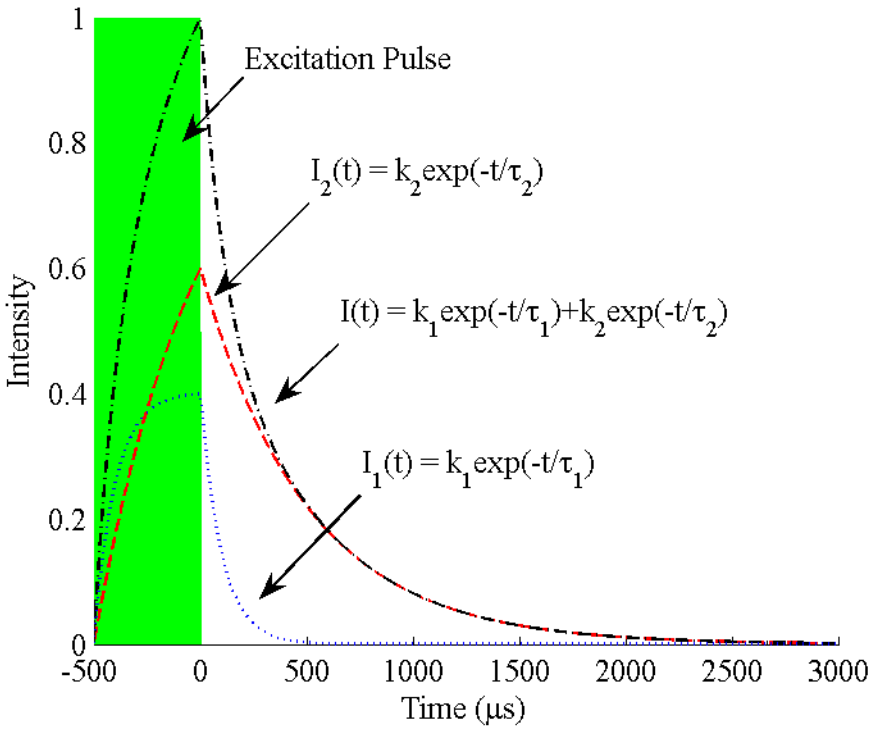

Figure 6.1 Diagram showing the combined response of a shorter-lived luminophore, L_1, and a longer-lived luminophore, L_2.

the luminophore with the longer lifetime, L_2. An example of a multi-exponential decay can be seen in Figure 6.1.

As with mono-exponential lifetime calculations, several methods have been developed to simplify multi-exponential lifetime measurements. This can be done by separating the response of L_2 from the combined response (Figure 4.3). This allows mono-exponential calculations to be used for each response assuming the contribution from L_2 is constant during the decay of L_1 (see Figure 4.3). This technique has been demonstrated with a windowed calculation technique (Dual Lifetime Determination) and NLLS.[156, 162, 190, 192] However, this may not be practical in cases where the lifetimes are

not different by three orders of magnitude which will result in τ_1 being dependent on the response of L_2. A similar approach utilizes four equi-width windows, either contiguous or overlapping, to calculate both lifetimes without separation of the signal (Figure 4.4).[181] However, the accuracy of this method has been shown to be highly dependent on signal level[181].[191] The requirement of equi-width windows for both lifetime measurements also means lifetimes must be similar in value ($\tau_2/\tau_1 \approx$ 3 to 4) to ensure that the window width is optimal and accurate lifetimes can be calculated.

Due to the limitations of these approaches, a new approach for dual lifetime calculations was investigated. This method combines the Dynamic Rapid Lifetime Determination (DRLD) discussed above and a window sum correction which will allow accurate lifetime calculations of both dyes.

6.1 Theory

As an alternative to least-squares analysis, there have been several methods developed which utilize window-sums to determine the lifetime responses.[27-29, 171, 179-181, 183, 185, 188-189, 208] Window-sums are calculated by performing integration or adding the data found in each windowed segment. Of the various methods reported, DRLD is of particular interest for dual lifetime calculations because of its speed and simplicity (see Chapter 5). This method calculates lifetimes using the traditional Rapid Lifetime Determination (RLD) equation:

$$\tau = \frac{\Delta t}{\ln(W_1/W_2)} \qquad 6.2$$

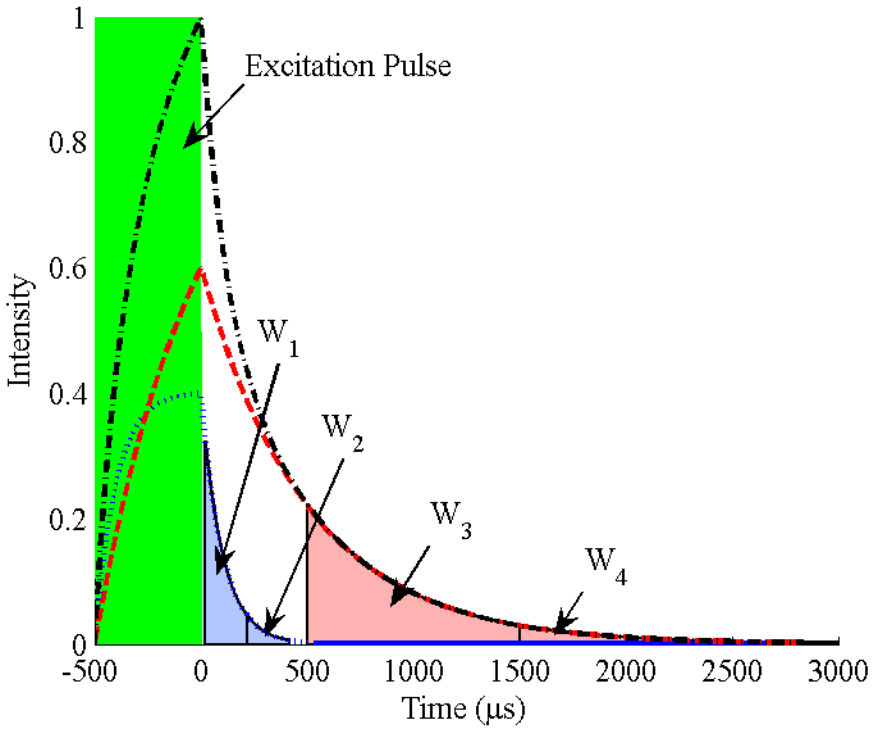

Figure 6.2 Depiction of a dual-exponential decay and the window sums utilized to calculate the lifetime response using DDRLD. The black dashed line represents the combined response, while the blue and red dashed lines represent response of L_1 and L_2, respectively. Example window sums are shown in the shaded regions.

where τ is the lifetime, Δt is the window width, and W_1/W_2 is the ratio of the window sums from the respective windows.[27-28] In addition, an algorithm is used to dynamically select the appropriate window width. Without such a selection algorithm, the window widths and start times remain constant during an experiment, leading to sub-optimal sampling parameters and inaccuracies in many cases.[27, 181, 188-189] For example, windows that are too large will lead to sampling data that contains very little signal while windows that are too small will be more greatly affected by the signal noise. However, by optimizing the window width, the accuracy of lifetime calculation can be improved

over a wider dynamic range which is necessary for applications where the lifetime is expected to vary (*e.g.* oxygen sensitive luminophores). In addition, this method retains the speed of other approaches that utilize window sums when compared to the speed of traditional NLLS calculations.[153]

To calculate the lifetimes of two luminophores, DRLD is utilized for each dye where the windows for the calculation of τ_2 were delayed until L_1 had decayed to zero (Figure 6.2). In order to determine τ_1, the initial intensity of L_2 is calculated using:

$$k_2 = \frac{W_3}{\tau_2 f_s \left(1 - {W_4}/{W_3}\right) e^{-t_d/\tau_2}} \tag{6.3}$$

where τ_2 is the lifetime calculated using Equation 6.2, f_s is the sampling frequency used during measurement, t_d is the time delay incorporated before sampling, and W_n is the respective window sum for each window. The time delay was incorporated to remove unwanted scattering and instrument response. After k_2 is determined, the response of L_2 can be subtracted from the measured (combined) signal; the resulting decay will be representative of L_1 and is used to calculate τ_1 with DRLD. Adjustment of the window delay of the second set of windows to 5 times τ_1 will allow improved accuracy of the τ_2 and subsequently improved accuracy of τ_1. This delay was chosen because the signal from L_1 will be less than 1% of the original signal level k_1 and thus assumed to be negligible during calculation of τ_2.

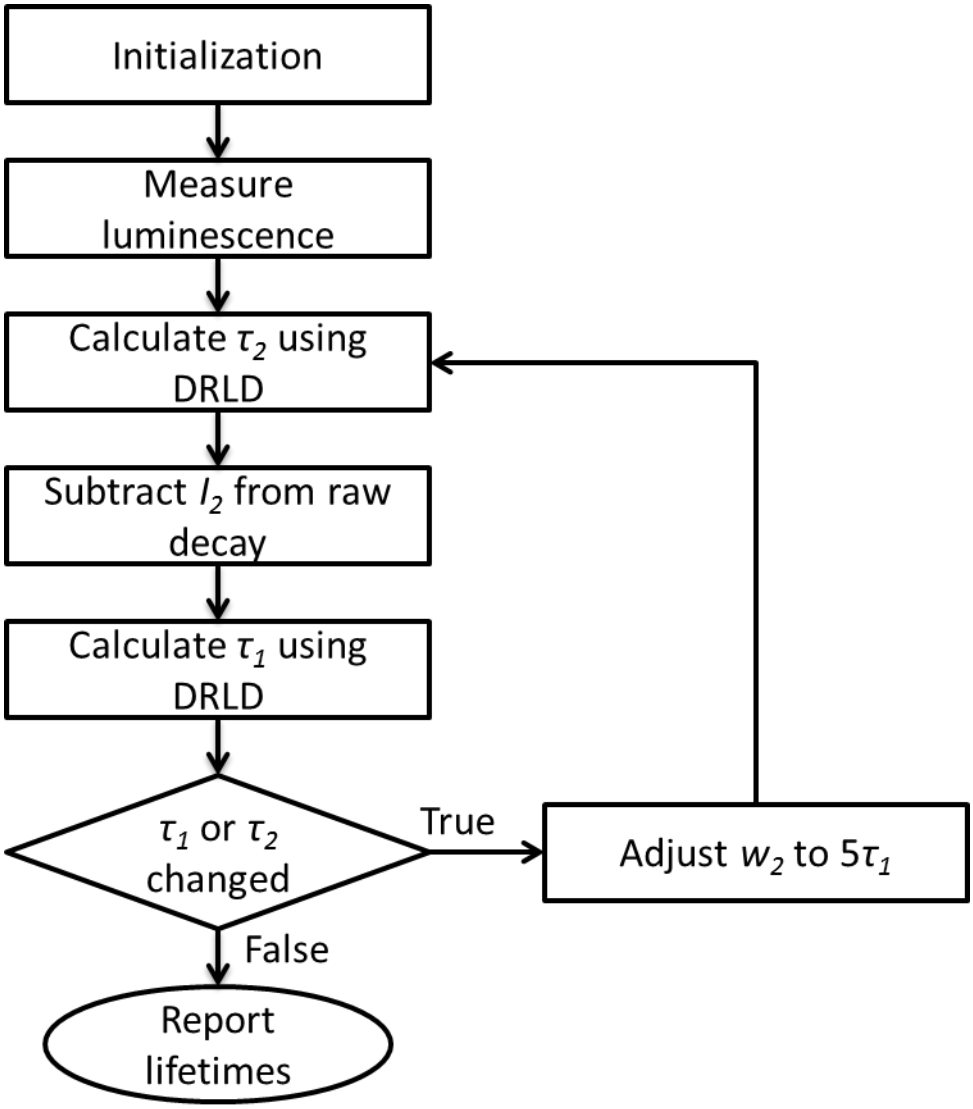

Figure 6.3 Diagram showing a simplified version of the DDRLD algorithm.

Dual lifetime calculations are done recursively until the window delay is no longer changing. The initial window delay time for the second set of windows for both calculation algorithms is initially set to a value greater than ten times the maximum expected lifetime of τ_1 (in this case 1000 μs) in order to ensure that there is not any contribution from L_1 in the initial τ_2 calculation. In addition, the maximum number of

iterations set for each algorithm is 10 in order to prevent infinite loops in the software where lifetimes bounce back and forth between two values. However, in most cases less iteration are needed. A simplified algorithm for this approach, which will be referred to as dual DRLD (DDRLD), can be found in Figure 6.3. An example of the MATLAB code used for DDRLD calculation can also be found in Appendix C. It should be noted that for the algorithm to work properly, the decay of L_2 must behave mono-exponentially.

6.2 Materials and Methods

In order to evaluate the potential of this method to accurately calculate the lifetime response of two luminophores simultaneously, an oxygen and temperature sensing system was employed. These analytes were chosen because of their biological significance. In addition, temperature compensation of oxygen sensitive luminophores is often necessary.[162, 190, 192, 199-206, 209] Platinum porphyrins are attractive for oxygen sensing due to their high sensitivity, large Stokes' shift, good photostability, long lifetimes, and emission in the red to NIR wavelengths.[210-218] Platinum(II) octaethylporphyrin (PtOEP) has excitation peaks close to 400, 500, and 550 nm and emission peaks near 650 nm.[203, 219] The lifetime of this dye in the absence of oxygen is also expected to be approximately 100 μs.[219] An inorganic phosphor, manganese(IV)-doped magnesium fluorogermanate (MFG), was used for temperature sensing because it does not display oxygen sensitivity.[220] The phosphor has an excitation peak near 400 nm, emits at 665 nm, and has a lifetime greater than 3 ms.[220-221] These luminophores were chosen because they both showed a large Stoke's shift and can be excited with a

single LED at 400 nm. The large difference in lifetime will also reduce the chance of inaccuracies occurring as was seen with similar approaches.[181] The overlap in emission spectra is not a concern because the response from each luminophore is resolved temporally.

Although DDRLD would ideally be performed with oxygen and glucose sensors in order to demonstrate *in vitro* the oxygen compensation method discussed in Chapter 3. However, due to the degradation often associated with enzymatic sensors, repeatability may be an issue. The dual sensing system described above will serve as an analogue of the desired oxygen and glucose sensing system because of its simplicity and higher expected repeatability (due to the absence of enzymatic components). Further considerations for employing DDRLD for measuring the response of glucose and oxygen sensors simultaneously will be discussed in Chapter 7.

6.2.1 Modeling of Dual Exponential Decays

Due to the large difference in lifetimes expected from PtOEP and MFG, dual exponential decays were also modeled using MATLAB to test the ability of DDRLD to distinguish decays from one another for a range of lifetimes and pre-exponential factors. This was done by setting k_1 and τ_1 to 1 and 10 μs, respectively, while k_2 and τ_2 were varied from 0.01 to 100 and 15 to 100 μs, respectively. This allows for the accuracy to be estimated as a function of the ratios k_2/k_1 and τ_2/τ_1. For each possible combination of decay parameters, ten decays were modeled using a sampling frequency of 2 MHz and a signal-to-noise ratio (SNR) of 10 in order to simulate real decays obtained. Lifetimes were then calculated using DDRLD with the first window delay set to 1 μs and

the second window delay set to five times τ_1 (50 μs) which is where it ideally remain due to the algorithm restrictions (Figure 6.3). Initial widths of each window pair were set to 10 μs. From these data, the relative standard deviation (RSD) of each lifetime was determined for each set of decay parameters by dividing the standard deviation by the average lifetime calculated. Absolute percent difference was also investigated by comparing the mean lifetime at each k and τ value to the modeled value. These parameters characterized the precision and accuracy of lifetime calculations, respectively and allowed analysis of the results to determine the optimal relative pre-exponential factors and lifetimes similar to previous reports.[27-28, 181, 188-189]

6.2.2 Sensor Formulation

PtOEP was purchased from Frontier Scientific and MFG was obtained from Global Tungsten & Powders Corp. (GTP Type 236). Similar to previously reported oxygen sensors, polystyrene (PS, Sigma, M_w=280,000) was utilized to slow oxygen diffusion through the matrix leading to higher lifetimes of the oxygen-quenchable dye.[213, 216] Toluene (Macron Chemicals) was used as a solvent for PtOEP and PS. A Sylgard 184 silicone elastomer kit (Dow Corning) was used to make polydimethylsiloxane (PDMS) films for support of each phosphor during testing.

Temperature sensing gels were made by mixing 3 mg of MFG in 2 mL of PDMS precursor and 200 μL of PDMS initiator. The solution was sonicated and then placed under vacuum until all bubbles were removed and then poured on a glass wafer. The wafer was then placed on a hot plate at 100°C to facilitate PDMS curing. The resulting film was approximately 4 cm in diameter. Although films were thoroughly mixed

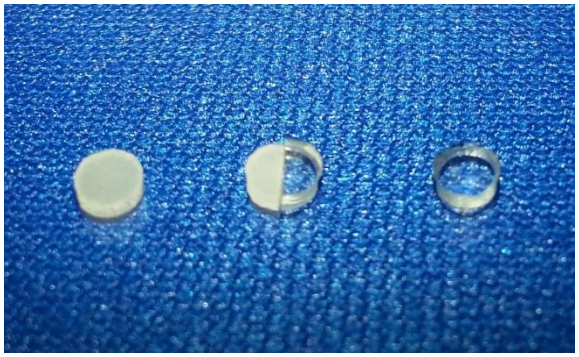

Figure 6.4 This picture shows examples of films tested. The sensor on the far left is an oxygen sensing film containing PtOEP and the sensor on the right is a temperature sensing film containing MFG. The sensor in the middle consists of halves of each film placed side-by-side.

before curing, aggregation of the phosphor was visible after curing and resulted in inhomogeneities in the film. The oxygen sensing film was made using a similar procedure. Fifteen μL of PtOEP solution (1 mg/mL of toluene) and 700 μL of polystyrene solution (250 mg/mL of toluene) were mixed with 1 mL of PDMS precursor and 100 μL of PDMS initiator. After vacuuming and heat curing, the resulting film was again approximately 4 cm in diameter. For individual film testing, a 2.5 mm biopsy punch was used to remove samples from each film for testing. Dual sensor measurement was performed by cutting the previously tested films in half and placing MFG and PtOEP films side-by-side (Figure 6.4).

6.2.3 Instrumentation and Measurement

The luminescent response of each of the sensors tested was measured using a custom TD measurement system.[153] Excitation of the dye was performed using an LED with a peak wavelength of 405 nm (LED 405E, Thorlabs). Square wave excitation with a frequency of 10 Hz and a duty cycle of 0.2 was utilized. Luminescence was detected

using a photo-multiplier tube module from Hamamatsu (H10721-20) after the light was passed through a longpass filter (3rd Millenium 620 nm, Omega Optical) using spherical lenses (LA-1951B). Decays were recorded for 15 ms with a sampling frequency of 2 MHz after the LED was turned off. For MFG and dual film experiments, the PMT control voltage was set to 0.85 V. Due to the wide range of intensities observed, a lower control voltage, 0.75 V, was used with PtOEP films to prevent saturation of the detector. During measurement, one hundred raw decays were summed to improve SNR and the resulting decay was used to calculate the lifetime. Further details of this measurement system can be found in Appendix A.

The gas-phase response of the sensors was measured using a custom reaction chamber.[152-153] The sensing films were immobilized in the reaction chamber by placing them on a glass slide which was then placed inside of an incubator (Torrey Pines Scientific, Echotherm IN35) used to control the temperature (25 to 65°C). Gas of various oxygen concentrations (0 to 21%) were exposed to the sensors by controlling compressed air and nitrogen flow rates using two mass flow controllers (MKS Instruments, 1179A) and a digital power supply (MKS Instruments, PR4000). The total flow rate was held constant at 2000 standard cubic centimeters per minute while the contribution from each gas was varied. All parts of the test-bench were automated and controlled using custom LabVIEW software (National Instruments). Further details of this test system can be found in Appendix B.

For this work, lifetime calculations for calibration purposes (single and dual films) were performed after data collection with MATLAB (MathWorks, Inc.). DRLD

was used to calculate the mono-exponential lifetimes for individual films while lifetimes of dual films were calculated using DDRLD. NLLS analysis with a mono-exponential fit was used to calculate lifetimes for individual films for comparison purposes. Real-time calculations utilizing DDRLD were performed with LabVIEW during a dynamic response experiment. In order to calculate lifetimes, windows used for MFG and PtOEP were set to an initial width of 200 and 5 μs, respectively. All single film experiments had an initial window delay of 1 μs while dual film experiments had 1 μs delay for PtOEP and an initial delay of 1000 μs for MFG as discussed above.

6.2.4 Film Testing and Analysis

Initially, individual PtOEP and MFG films were each tested in triplicate. For each test, ten lifetimes were averaged for each environmental condition (*i.e.* oxygen concentration and temperature) tested. The response of the three individual films was then averaged to determine the expected response from dual film measurements. For MFG films, the lifetime response of MFG films was recorded at five different temperatures (25 to 65°C in 10° increments) using an oxygen concentration of 21%. Linear regression was then used to fit the averaged film responses and obtain a calibration for the temperature sensitive MFG response.

To keep testing time to a minimum, calibration of the PtOEP films was performed at only three temperatures (25, 45, and 65°C) but for a range of oxygen concentrations at each temperature. These concentrations (0, 2.625, 5.25, 10.5, and 21% oxygen) were skewed towards lower oxygen levels where sensitivity of the porphyrin is

higher. The response at each temperature was fit with NLLS using a two-site Stern-Volmer equation:

$$\frac{\tau_0}{\tau} = \left(\frac{f}{1 + K_{SV1}[O_2]} + \frac{1 - f}{1 + K_{SV2}[O_2]}\right)^{-1} \quad 6.4$$

where τ_0, is the lifetime in the absence of the quencher (in this case oxygen O_2), τ is the lifetime, f is the fractional contribution from each site, and K_{SVn} is the respective Stern-Volmer constant.[19, 211, 214, 222] After initial fittings, the fractional contribution was averaged and used to re-fit the data to allow more accurate temperature-dependent trends to be determined. It is assumed that this value remains constant despite temperature changes. The temperature-dependent trends of the parameters (τ_0, K_{SV1}, and K_{SV1}) in Equation 6.4 were then determined using linear regression.

As previously mentioned, dual film responses were measured using the same measurement system with a side-by-side approach where halves of the previously tested films were utilized. Testing of the dual film response was performed similar to testing of PtOEP films. The validity of DDRLD was investigated by comparing the lifetimes obtained from the dual films with the response of the individual films.

A dynamic experiment was also performed to demonstrate the ability of DDRLD to measure the response of a dual luminescent system. This was done by exposing the dual films to random, un-calibrated temperatures and oxygen concentrations. When temperature was changed, the experimental setup was held there (*i.e.* temperature and oxygen was not changed) for 2 hours to ensure the temperature throughout the reaction chamber reached equilibrium. Changes in oxygen concentration were only held for 15

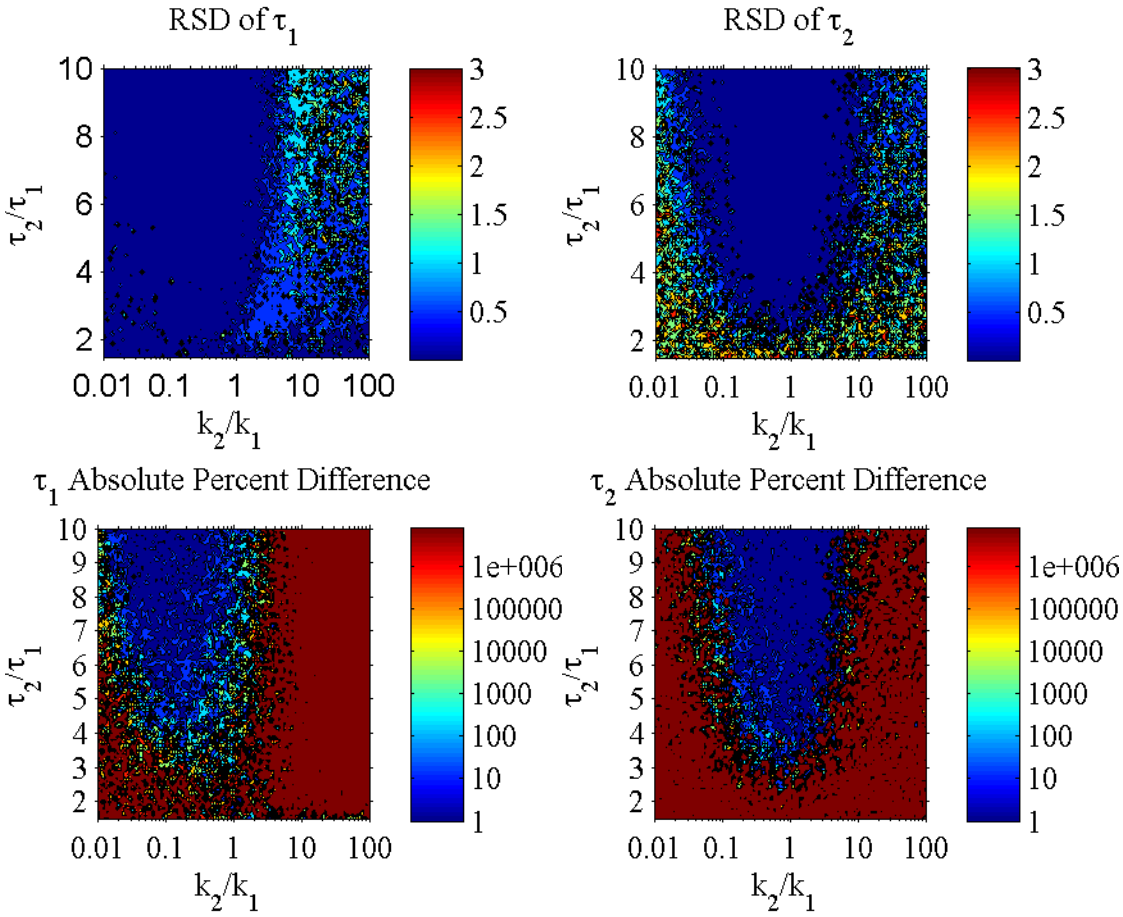

Figure 6.5 Contour maps showing RSD values lifetimes calculated using DDRLD for modeled decays with a range of k_2/k_1 and τ_2/τ_1 values. RSD for τ_1 is in the left graph while RSD for τ_2 is shown in the graph at the right.

minutes because the changes within the reaction chamber were almost immediate. Dual lifetime measurements were recorded for the duration of this experiment and converted to predictions of oxygen and temperature levels after the experiment. Although predictions could be made in real-time, dynamic tracking abilities could be assessed based on the accuracy of the lifetime responses. This accuracy was quantified by

calculating the percent difference for n = 10 predictions at each oxygen and temperature combination tested.

6.3 Results and Discussion

6.3.1 Results of Modeled Dual-Exponential Lifetime Calculations

RSD and absolute percent difference values obtained after modeling DDRLD calculations for a range of values for k_2/k_1 and τ_2/τ_1 can be seen in Figure 6.5. These graphs showed good agreement about the relative parameters needed for optimal dual lifetime calculations. Accuracy appears to be highest when k_2/k_1 is between 0.1 and 1 where the blue regions of each absolute percent difference contour map overlap. Lifetime calculations are also more accurate when τ_2/τ_1 is greater than 3. RSD contour maps display similar trends but with a slightly larger optimal area (values represented by blue).

When the relative decay parameters fall outside of this region, DDRLD suffers from a drastic reduction in accuracy for modeled decays with an SNR of 10. A higher SNR will likely lead to wider optimal regions, but these results clearly indicate the limitations of this method under normal working conditions. These results should be utilized to select luminophores with the appropriate lifetimes. Intensity is less of a concern when selecting luminophores because it is not an inherent property of the luminophore and can be adjusted by changing the concentration.

6.3.2 Calibration of Individual Film Responses

The response of individual MFG films can be seen in Figure 6.6. Although the response from film-to-film was statistically different, each response follows the same

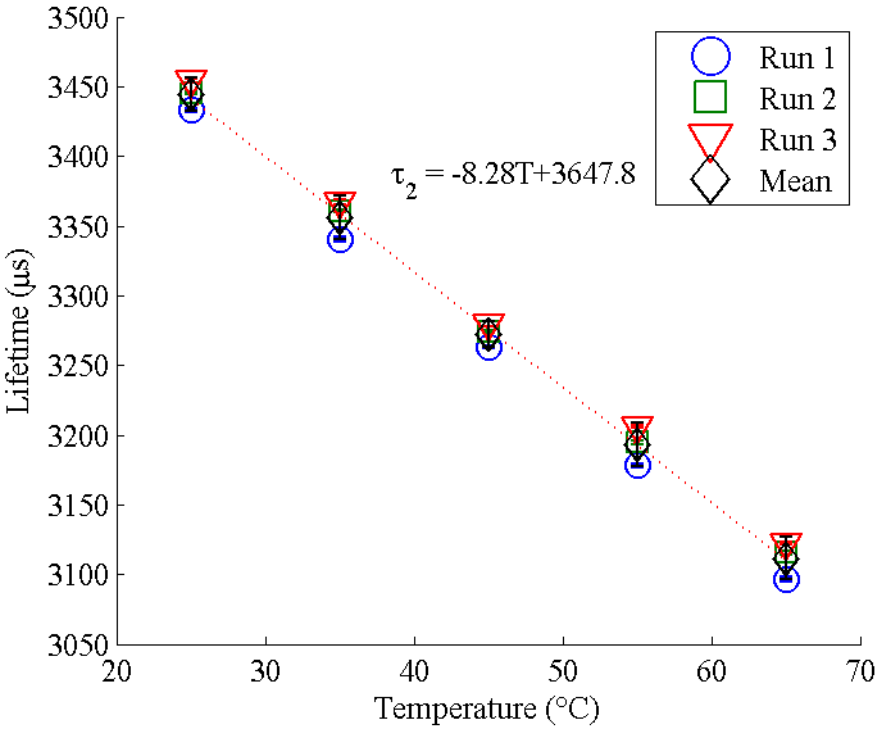

Figure 6.6 This graph shows the response of three individual MFG films (Runs 1-3) and the averaged response. The red dotted line represents the linear fit of the averaged response. Error bars represent the 95% confidence interval with n = 10 for individual films and n = 3 for the averaged response.

general trend. Variability may be a result of variations in the signal-to-noise ratio due to non-uniform dispersal in the PDMS. The averaged response, however, showed good linearity (R^2 > 0.99) with a slope of -8.28 µs/°C and an intercept of 3647.8 µs. The averaged lifetimes calculated using NLLS were not significantly different than averaged lifetimes calculated using DRLD (α = 0.05, data not shown).

In contrast to the MFG response, PtOEP films showed much less variability. In addition, the lifetimes calculated using NLLS were on average only 0.77 µs less than those calculated using DRLD despite being statistically different (α = 0.05, data not

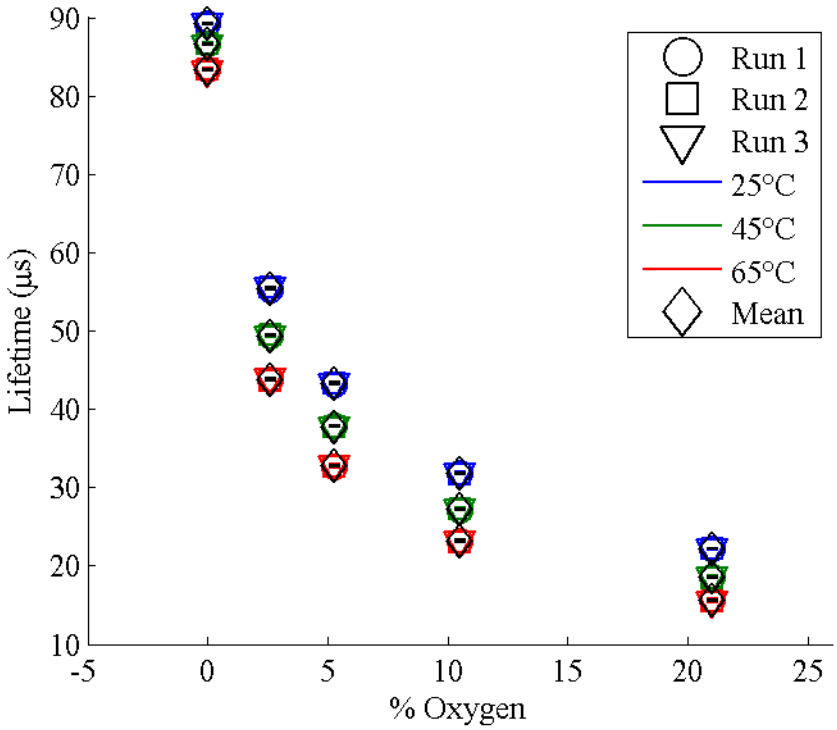

Figure 6.7 Response of individual PtOEP films to oxygen and temperature. Error bars represent the 95% confidence interval with n = 10 for individual films (Runs 1-3) and n = 3 for averaged data.

shown). The difference is most likely due to the multi-exponential nature of the decays for PtOEP which is often dependent on the immobilization matrix.[222-224] Similar to reports of other oxygen sensitive luminophores, the oxygen sensitivity was higher at lower oxygen concentrations and increases in temperature lead to decreases in the lifetime response.[162, 190, 200] Due to the non-linear nature (see Equation 6.4) of the oxygen response as well as the temperature dependency, calibration of the PtOEP films required more thorough analysis in order to predict oxygen concentrations accurately (Figure 6.7).

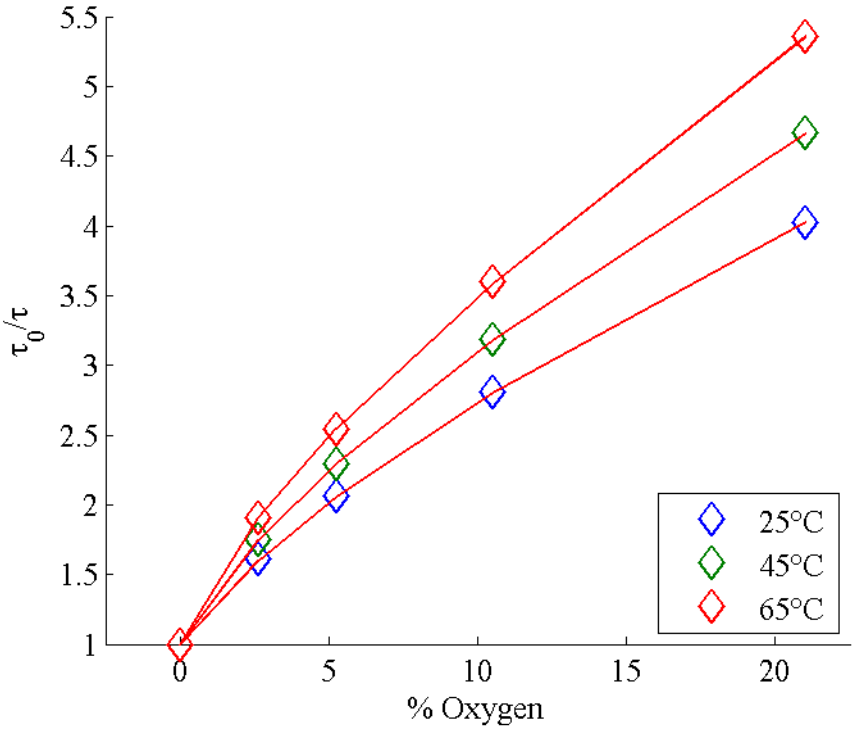

Figure 6.8 Stern-Volmer response of the PtOEP films. The red line represents the fit obtained using Equation 6.4 which was used for calibration.

First, the Stern-Volmer plot for the response at each temperature was determined using the appropriate values for τ_0 (Figure 6.8). After initial fitting using Equation 6.4, the mean fractional intensity, f, was found to be 0.278. This value was used to re-fit the Stern-Volmer responses and the resulting trends of K_{SV1} and K_{SV2} as a function of temperature (T) were found. These values along with the temperature dependent values for τ_0 can be found in Figure 6.9. The linear fits used for calibration of τ_0, K_{SV1}, and K_{SV2} all had an R^2 value greater than 0.99. This indicates that these trends can be used to estimate the oxygen concentration for all temperatures within or near the tested range as long as the ambient temperature is accurately predicted. When these values were

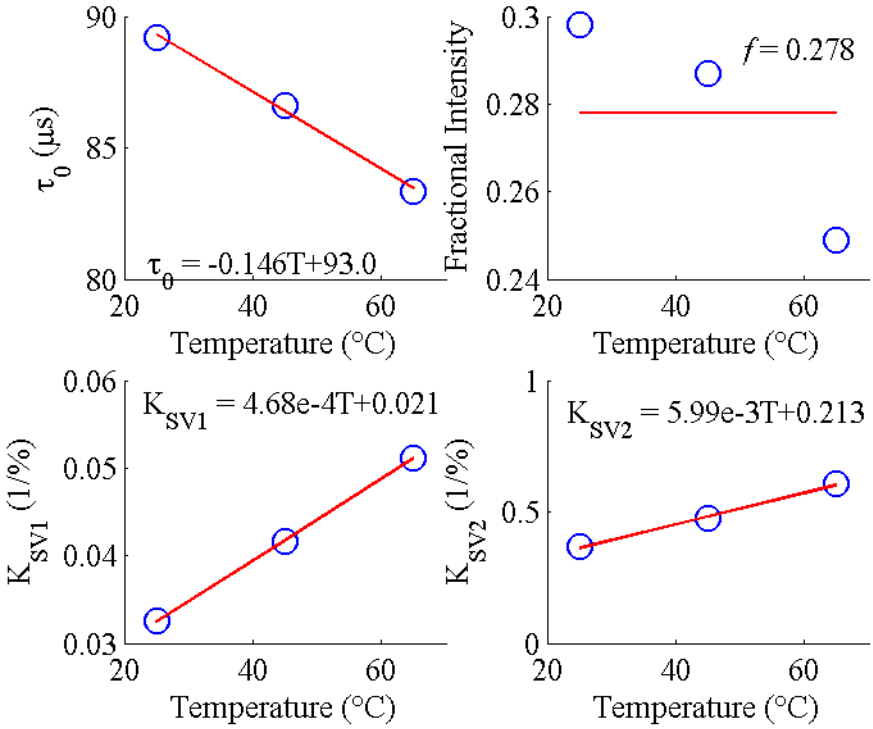

Figure 6.9 Temperature (T) dependent trends for τ_0, K_{SV1}, and K_{SV2} can be seen in the top left, bottom left, and bottom right images, respectively. The red lines show the linear fit obtained for each set of data. The top right image shows the initial fractional intensities obtained where the red line represents mean value that was used to obtain K_{SV1} and K_{SV2}.

plugged into Equation 6.4 and compared to the original data, R^2 remained greater than 0.99.

6.3.3 Dual Film Responses

Following calibration of the individual film responses, the lifetimes of dual films calculated using DDRLD were compared to the response of individual films where the lifetimes were calculated using DRLD. As can be seen in Figure 6.10, the MFG response calculated using DDRLD for dual film measurements was not significantly different than the average DRLD response for any condition tested. Although it appears

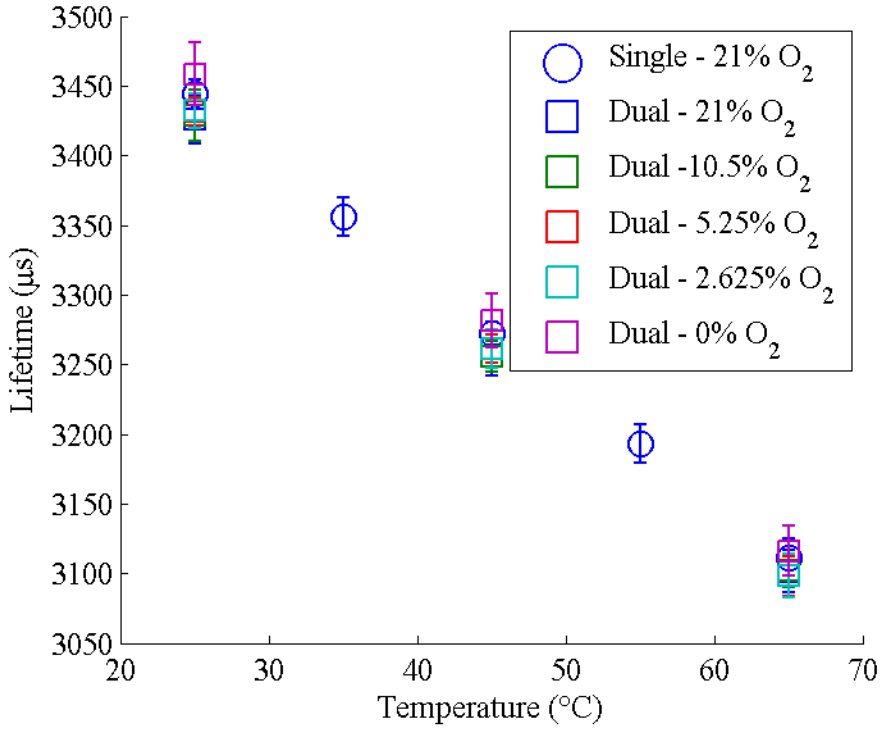

Figure 6.10 Comparison of the MFG lifetime response for individual and dual film experiments where lifetimes were calculated using DRLD and DDRLD, respectively. Error bars represent the 95% confidence interval for n = 3 films.

that the lifetime increases slightly with increasing oxygen concentration, this is not statistically significant and is actually due to a decrease in the noise as luminescence decays (data not shown). Increasing delay in the windows used for τ_2 calculation, as is done for DDRLD calculation, results in a slight shift in the calculated lifetime. Improvements in SNR throughout the decay are expected to reduce this issue.

As expected, PtOEP lifetimes calculated using DDRLD for dual film measurements followed the same trends as individual film data (Figure 6.11). However, the lifetimes calculated for dual films were statistically different than results calculated for individual films. Despite this, the average percent difference for the dual film

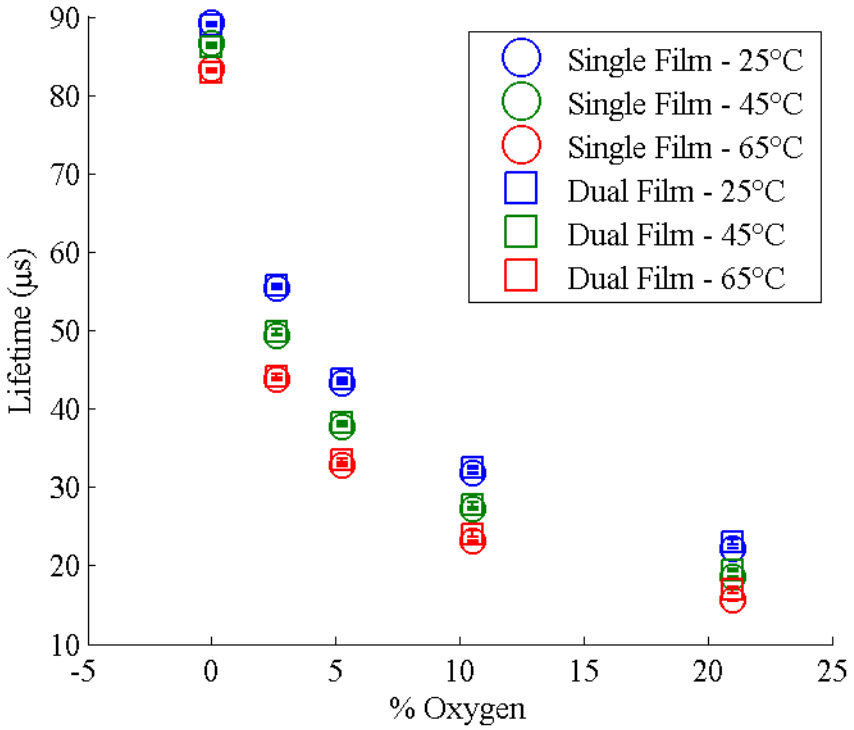

Figure 6.11 Comparison of lifetimes calculated for dual film experiments using DDRLD and individual film experiments where lifetimes were calculated using DRLD. Error bars represent 95% confidence intervals for n = 3 films.

lifetimes was only 2.04% above the expected (*i.e.* individual film) values suggesting DDRLD is still a valuable tool. The largest percent difference, 8.41%, occurred at 21% oxygen and 25°C where the SNR of the response of L_1 is the lowest compared to the response of L_2. Overall, lifetimes calculated using DDRLD for dual film measurements were in good agreement with the response of individual films containing MFG and PtOEP.

6.3.4 Dynamic Testing

Using the calibration curves obtained above, a dynamic experiment was performed where ambient oxygen levels and temperature were predicted. The real-time

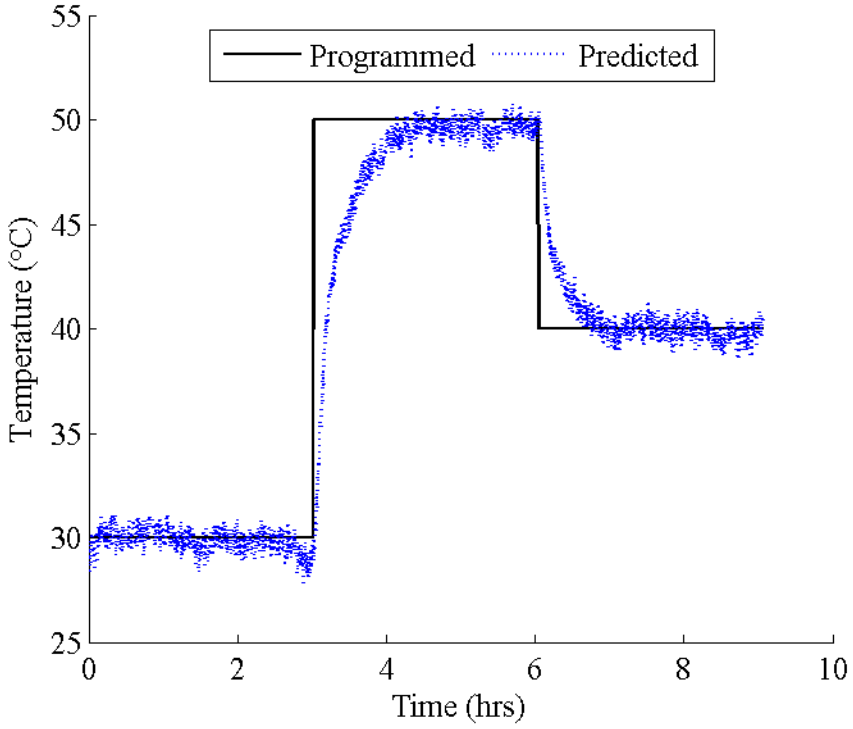

Figure 6.12 Results of a dynamic test showing programmed and predicted temperatures. DDRLD was utilized to monitor the lifetime responses of the two films simultaneously. Temperature predictions were determined from a linear calibration curve.

temperature prediction from the MFG response compared to the temperature programmed into the incubator can be seen in Figure 6.12, and as expected, the MFG response is able to track the ambient changes in temperature. Calculating the percent difference for n = 10 predictions at each concentration and temperature, the average percent difference for all concentrations and temperatures was found to be 0.72% suggesting an accurate prediction of temperature. It is important to note that the slow response time observed for MFG is due to the long equilibration time of the incubator and reaction chamber and not the sensor film.

Oxygen predictions performed with compensation showed a similar ability to

track oxygen levels as temperature predictions; however, predictions tended to be lower than the actual levels (Figure 6.13). At 15.75% oxygen, the relative error for compensated predictions was found to be 8.77% but at the lowest levels tested (2.1% oxygen), the response was off by only 0.63% (Table 6.1). This improved accuracy at lower oxygen levels is due to an increase in intensity from the PtOEP resulting in a higher SNR. The reduced accuracy in oxygen prediction at higher oxygen concentrations is due to the exponential shape of the oxygen response curve and the difference in PtOEP lifetimes calculated using DRLD and DDRLD (discussed above).

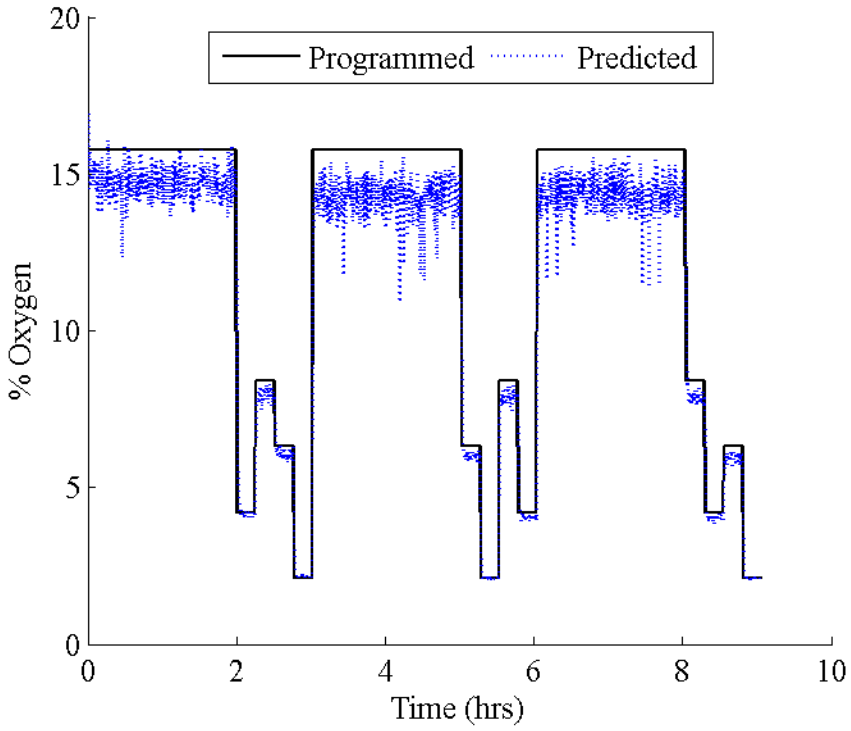

Figure 6.13 This graph depicts the programmed and predicted oxygen concentrations from a dynamic test. DDRLD was utilized to monitor the lifetime responses of the two films simultaneously. A temperature compensating PtOEP calibration curve was used to predict oxygen levels.

Table 6.1 Percent differences calculated for n = 10 predictions during the dynamic testing of dual film responses. Calibration type refers to calibrations made using either single or dual film responses. Uncompensated results utilized the calibration curve at 40°C while compensated results utilize a variable calibration curve as discussed in the text.

Oxygen (%)	Calibration Type	Compens.	Temp. (°C)		
			30	40	50
2.1	Single	N	17.3	0.468	-17.8
	Single	Y	-2.60	0.919	-0.200
	Dual	Y	-4.35	-0.560	-1.59
4.2	Single	N	18.1	4.59	-12.8
	Single	Y	0.82	3.42	3.72
	Dual	Y	-1.17	1.46	1.65
6.3	Single	N	20.2	6.18	-10.6
	Single	Y	3.93	5.66	5.14
	Dual	Y	1.61	3.10	2.14
8.4	Single	N	20.7	6.70	-9.60
	Single	Y	5.46	7.07	5.90
	Dual	Y	2.64	3.75	1.84
15.75	Single	N	21.3	9.00	-3.64
	Single	Y	7.09	9.07	10.14
	Dual	Y	2.16	3.04	3.04

For example, the expected response of τ_1 at 25°C and 21% oxygen is 22.3 μs, however, if τ_1 was measured to be 1 μs lower than the expected, the predicted oxygen concentration would be 22.8%. Similarly, if the expected response of τ_1 at 25°C and 0% oxygen (89.3 μs) was low by 1 μs, the predicted oxygen concentration would be 0.04%.

These differences in predicted and actual oxygen levels indicate the greater effect inaccurate lifetime calculations have at higher oxygen concentrations.

To improve the accuracy of lifetime predictions, calibration curves of the PtOEP response using DDRLD data from Figure 6.11 were determined (data not shown). These calibration curves were then utilized to make oxygen predictions for the same dynamically obtained lifetimes utilized to obtain the predictions in Figure 6.13. As can be seen in Figure 6.14 and Table 6.1, these results show a higher accuracy at higher oxygen levels than predictions made using calibrations obtained from individual film responses. Again, this is due to the difference in the lifetime response calculated for

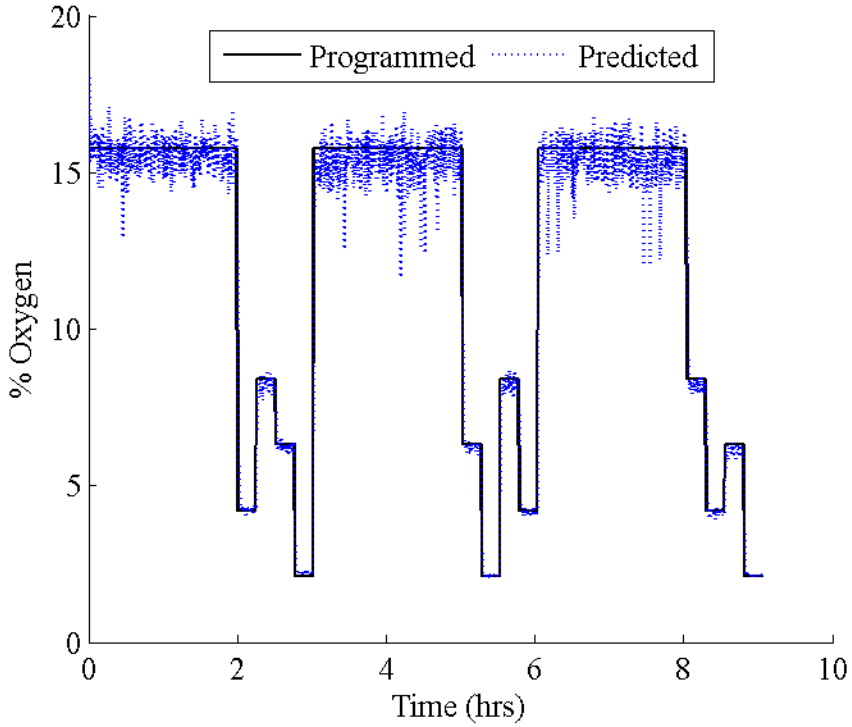

Figure 6.14 Real-time dynamic oxygen predictions made using calibration curves obtained from a dual film PtOEP response. The same lifetimes obtained from the previously described dynamic experiment were utilized.

individual and dual film measurements using DRLD and DDRLD, respectively.

Oxygen predictions made with temperature compensation were also compared to predictions made without compensation (assuming calibration was performed at 40°C). As expected for predictions made when the programmed temperature was 40°C, the compensated and uncompensated predictions have similar accuracy (Table 6.1). However, when the actual temperature is not 40°C, uncompensated oxygen predictions are much less accurate. This demonstrates the need for temperature compensation of a luminescent oxygen sensor response when a range of ambient temperatures are expected.

Despite the inaccuracies of oxygen prediction, which could be reduced by improving SNR, the usefulness of this approach is evident based on the predictions for un-calibrated temperatures and oxygen concentrations. It is also interesting to note that the oxygen predictions do not appear to be temperature dependent because the responses at the same oxygen concentration but different temperatures appear to be the same.

6.4 Conclusions

A dual dynamic rapid lifetime determination (DDRLD) algorithm was investigated that is able to calculate the lifetime response of two temporally-distinct luminophores simultaneously. Using modeled decays, this dual lifetime calculation approach was found to be limited multi-exponential decays where τ_2/τ_1 is greater than 3 and k_2/k_1 is between 0.1 and 1. This approach was demonstrated *in vitro* by performing temperature compensation of an oxygen-sensitive porphyrin after calibrating an oxygen sensing film at three different temperatures and determining the linear temperature dependency of the calibration fit parameters. Lifetimes calculated for dual films using

DDRLD were compared to lifetimes calculated for individual films using DRLD. The response of the temperature sensing films was not found to be statistically different. Lifetimes of oxygen sensing films did display some difference but is considered to be quite low on average (2%). Temperature compensation was then applied with DDRLD to demonstrate real-time, dynamic predictions of oxygen and temperature.

Individually, each of the techniques demonstrated (a compensation algorithm and a method for measuring two lifetimes simultaneously) can be applied to a variety of sensing applications. The compensation method demonstrated will allow improved accuracy in oxygen measurements. The simplicity of the approach will also lend its usefulness to other applications where compensation is needed to improve the accuracy of measurements of the desired analyte (such as oxygen compensation of enzymatic glucose sensors). DDRLD can also be utilized with a variety of biomedical, environmental, and food industry applications due to its ability to perform real-time measurements without sacrificing accuracy.

7. CONCLUSIONS AND FUTURE WORK

Different computational and algorithmic techniques to improve the accuracy and thus viability of luminescent, enzymatic sensors were proposed and demonstrated within this work. These techniques will assist in the progression of these sensors toward *in vivo* use by people with diabetes.

Due to the co-consumption of glucose and oxygen during the reaction of glucose oxidase (GOx), an enzyme commonly used by glucose sensors, the dependence of the response on ambient oxygen concentration was investigated *in silico* using COMSOL Multiphysics. After confirmation of inaccurate glucose predictions due to variations in the ambient oxygen concentration, a novel compensation technique was developed and demonstrated. This approach utilized a variable calibration curve where the fit parameters were determined as a function of oxygen levels which will be measured separately. Using randomized oxygen and glucose levels based on expected *in vivo* values, glucose predictions using the proposed compensation technique and un-compensated predictions were compared. Even when measurement error was considered, compensated predictions were located within the clinically acceptable regions (A and B) of the standard Clarke error grid more than 95% of the time while un-compensated predictions were within this region less than 50% of the time.

The compensation algorithm demonstrated utilizes a variable calibration curve which is dependent on the interfering species. Due to its nature, this mechanism is broadly applicable to a variety of enzymatic and other kinds of sensors where the response follows predictable trends for both analytes. However, extensive calibration

will need to be performed for both analytes in order to understand these trends. In addition, this approach may only be applied in instances where the confounding analyte can be measured separately from the analyte of interest. Nevertheless, this approach will lead to improved accuracy of a variety of analytes in instances where confounding analytes are present.

This large improvement in accuracy using oxygen compensation led to the investigation of a novel technique for monitoring two sensors simultaneously. Due to the advantages of time-domain luminescence lifetime measurements over intensity and frequency-domain lifetime measurements *in vivo*, this approach is ideal for measuring the response of implantable luminescent sensors. The development of this approach was first limited to the measurement of the response of a single sensor.

Building on the principles of Rapid Lifetime Determination, the Dynamic Rapid Lifetime Determination (DRLD) method utilizes integration of two temporal windows in order to quickly calculate the lifetime response. However, due to the inaccuracies that result when static window widths are used for a wide range of lifetime responses, a dynamic windowing approach was implemented. This resulted in improved accuracy of lifetime calculations over a wider dynamic range as demonstrated by monitoring the response of a luminescent oxygen sensor. In addition, DRLD displayed a calculation time that was six orders of magnitude less than traditional non-linear least-squares calculations of lifetime.

Due to the need for measurement of ambient oxygen concentration while performing compensation of an enzymatic glucose sensor, DRLD was extended to

measurement of two lifetimes (and thus two sensors) simultaneously. The Dual DRLD (DDRLD) approach requires luminophores with temporally-distinct lifetimes (at least three times different) in order to separate the response of each sensor. Two pairs of windows are required in order to calculate the lifetime of each luminophore. Initially, the lifetime and initial intensity of the longer-lived luminophore is calculated by delaying the second pair of windows until after the response of the shorter-lived dye has decayed to zero. The response of this luminophore can then be removed from the total signal allowing the lifetime of the shorter-lived luminophore to be calculated.

DDRLD was demonstrated using temperature and oxygen sensing films. These analytes were chosen as a model system due to the temperature dependency of oxygen-quenchable porphyrins. Similar to a glucose and oxygen sensing system, a variable oxygen calibration curve that is dependent on the ambient temperature was utilized. An inorganic phosphor was chosen as the temperature sensitive luminophore due its long lifetimes (~3.5 ms) and insensitivity towards oxygen. Responses measured for films containing a single luminophore showed good agreement with the responses measured during measurement of both films simultaneously. In the case of the inorganic phosphor, the single and dual film measurements were not significantly different. Although oxygen sensitive films did display a statistical difference ($\alpha = 0.05$) in the response measurement for single and dual films, the average percent difference was only 2.04%. Using the results obtained, dynamic tracking of un-calibrated temperature and oxygen values was demonstrated. As expected, compensated oxygen predictions

displayed more accuracy over a range of temperatures than un-compensated predictions made using a static calibration curve.

The development of DDRLD provides a unique tool for the determination of multiple luminescence lifetimes which can be employed with a variety of luminescent, multi-analyte sensors which are often needed for compensation or diagnostic purposes. The variety of implementations may be limited to the ability to find luminophores or develop luminescent sensors (*e.g.* enzymatic sensors where the response is measured indirectly) with enough temporal-resolution between the lifetimes (see Chapter 6). However, it will be easier to implement sensors using DDRLD because actual lifetime responses are measured which allows calibration of these sensors to be performed individually unlike many ratiometric-based time-resolved measurements. In addition, the speed of computation over non-linear least-squares calculations will allow implementation of this algorithm with low-cost, portable electronics. Furthermore, the development of DDRLD provides a mechanism whereby oxygen compensation of enzymatic glucose sensors can be measured *in vivo*.

Employing DDRLD to perform oxygen compensation in the future will require the use of two oxygen-sensitive dyes will not to be utilized; one for glucose sensing and one for oxygen sensing. However, the lifetime of these luminophores must remain sufficiently distinct as discussed above. This can be achieved by utilizing porphyrins with different metal ions (*i.e.* platinum and palladium) bound to the center. Palladium porphyrins have been shown to have a lifetime that is an order of magnitude longer in the absence of oxygen than platinum porphyrins with the same structure.[219] Assuming

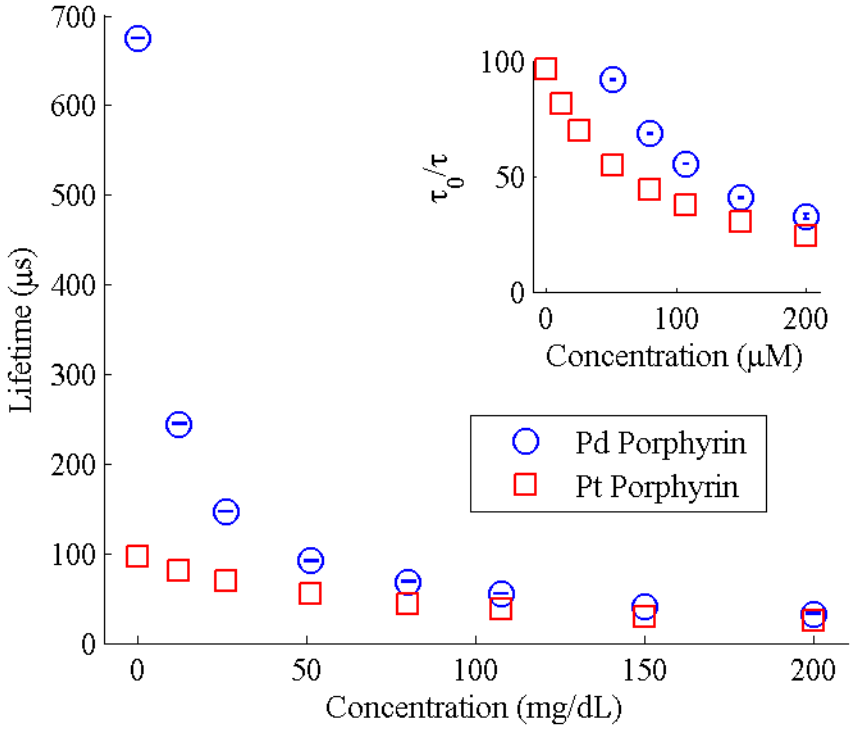

Figure 7.1 Measured lifetime responses of a palladium porphyrin and the estimated lifetime response of a platinum porphyrin of the same structure and immobilized in the same matrix (see text). The inset shows the response of the platinum porphyrin in greater detail.

the glucose concentration never reaches zero, the ambient oxygen concentration will always be greater than oxygen levels inside glucose sensors which will allow oxygen and glucose sensors to utilize a platinum and palladium porphyrin, respectively. The glucose sensor must utilize the longer-lived palladium porphyrin because the consumption of oxygen within the sensor will lead to increases in the lifetime. This will help ensure that each luminophore response can be resolved at lower oxygen concentration where the lifetimes have less temporal distinction (see below).

Modeling was again utilized to predict the simultaneous response of these oxygen and glucose sensors. The relative response of a platinum porphyrin to a palladium porphyrin with the same molecular structure and immobilized in the same matrix was estimated by reviewing the literature. For both K_{SV} and τ_0, palladium porphyrins were found to have values that were approximately seven times larger than values for platinum porphyrins.[224-226] Using this information, the response of a platinum porphyrin immobilized in a pHEMA matrix was estimated using the data from Chapter 3 (Figure 7.1).

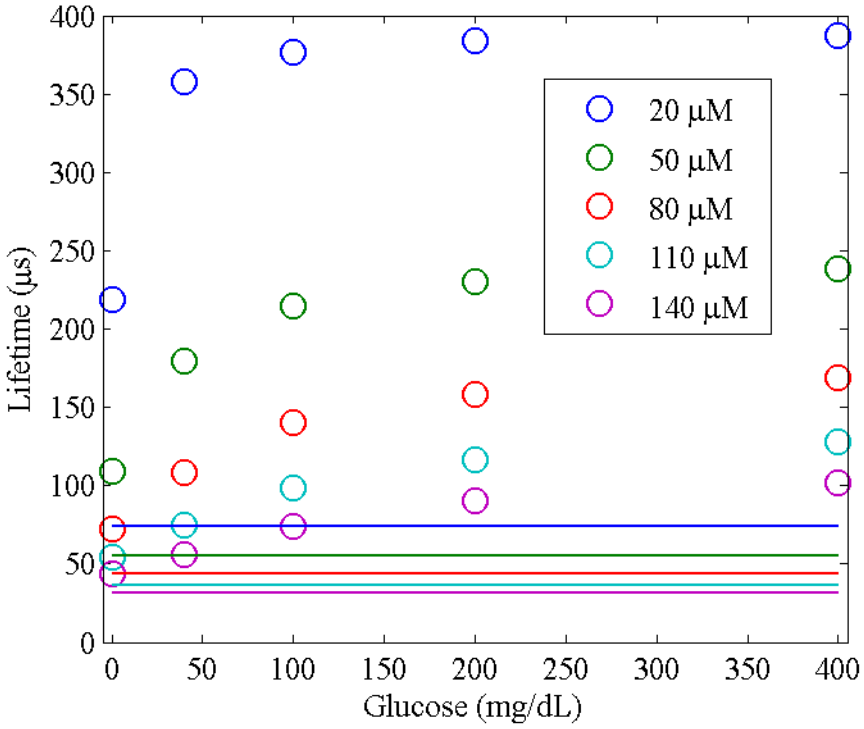

Figure 7.2 Values in circles represent the modeled response of an enzymatic glucose sensor utilizing a palladium porphyrin to a range of glucose and oxygen values. Lines are used to represent the response of an oxygen sensor utilizing a platinum porphyrin because the response is independent of glucose concentration. Circles and lines with the same color represent the response to a specific oxygen level shown in the legend.

Following estimation of a platinum porphyrin response, modeling was utilized to determine the combined response for a dual oxygen and glucose sensing system. Similar to the work performed in Chapter 3, a GOx concentration of 1.62e-10 M was utilized with the diffusion coefficients of glucose and oxygen each set to 1e-11 m^2/s. Using these parameters, the lifetime responses were predicted for a range of glucose (0 to 400 mg/dL) and oxygen (20 to 140 μM) concentrations. The results can be found in Figure 7.2 where the line represents the expected oxygen response which is independent of glucose concentration and the circle markers show the expected glucose sensor response. As expected, the lifetime of the glucose sensor was always higher than the response of the oxygen sensor. However, higher oxygen concentrations and lower glucose values produced lifetimes that were not sufficiently distinct as determined in Chapter 6 (Table 7.1). The predicted results at 0 mg/dL are not a concern because *in vivo* glucose levels are not expected to get this low. However, glucose values greater than 40 mg/dL this remains an issue which will lead to less accurate glucose predictions when oxygen is greater than 50 μM. This suggests that the current formulation will be viable for only

Table 7.1 Ratio of the glucose sensor lifetime response to the oxygen sensor lifetime for the oxygen and glucose values modeled. Shaded areas represent values that are below the required ratio needed to obtain accurate results ($\tau_2/\tau_1 > 3$).

[glucose] (mg/dL)	$[O_2]$ (μM)				
	20	50	80	110	140
0	2.95	1.97	1.65	1.49	1.39
40	4.82	3.25	2.46	2.04	1.80
100	5.08	3.89	3.18	2.71	2.37
200	5.17	4.16	3.59	3.19	2.88
400	5.21	4.31	3.84	3.51	3.26

low oxygen concentrations (< 50 μM). However, variability and baseline oxygen concentrations at *in vivo* implantation sites are still not widely characterized, unlike oxygen pressure (see Chapter 3). A better understanding of these values and additional tailoring of the response of each sensor will lead to improve the temporal distinction leading to glucose measurements with a higher degree of accuracy.

Future work will entail the *in vitro* validation of the proposed method for oxygen compensation of enzymatic glucose sensors. After thorough characterization of oxygen-dependence of the sensor through testing at a range of oxygen and glucose levels, development of a dual sensing matrix or configuration for oxygen and glucose will be investigated. I hypothesize that DDRLD can then be used in conjunction with the oxygen compensation algorithm to accurately predict *in vivo* glucose levels. The development of these techniques will lead to improved glucose monitoring and thus reduced risk of health complications related to diabetes.

REFERENCES

1. American Diabetes Association. *Diabetes Care* **2004**, *27*. s91-s93.

2. Brauker, J. *Diabetes Technol. Ther.* **2009**, *11*. S-25-S-36.

3. McNichols, R. J.; Cote, G. L. *J. Biomed. Opt.* **2000**, *5*. 5-16.

4. Pickup, J. C., Hussain, F., Evans, N. D., Rolinski, O. J.; Birch, D. J. S. *Biosens. Bioelectron.* **2005**, *20*. 2555-2565.

5. Pickup, J. C., Hussain, F., Evans, N. D.; Sachedina, N. *Biosens. Bioelectron.* **2005**, *20*. 1897-1902.

6. Khalil, O. S. *Clin. Chem.* **1999**, *45*. 165-177.

7. Oliver, N. S., Toumazou, C., Cass, A. E. G.; Johnston, D. G. *Diabet. Med.* **2009**, *26*. 197-210.

8. Steiner, M.-S., Duerkop, A.; Wolfbeis, O. S. *Chem. Soc. Rev.* **2011**, *40*. 4805-4839.

9. Wilson, R.; Turner, A. P. F. *Biosens. Bioelectron.* **1992**, *7*. 165-185.

10. Brown, J. Q., Srivastava, R.; McShane, M. J. *Biosens. Bioelectron.* **2005**, *21*. 212-216.

11. Brown, J. Q., Srivastava, R., Zhu, H.; McShane, M. J. *Diabetes Technol. Ther.* **2006**, *8*. 288-295.

12. Brown, J. Q.; McShane, M. J. *Biosens. Bioelectron.* **2006**, *21*. 1760-1769.

13. McShane, M. J., Microcapsules as “Smart Tattoo” Glucose Sensors: Engineering Systems with Enzymes and Glucose-Binding Sensing Elements. In *Topics in Fluorescence Spectroscopy: Glucose Sensing*, ed. C. D. Geddes, J. R. Lakowicz. Springer: New York, NY, 2006, vol. 11, pp 131-163.

14. Gough, D. A., Lucisano, J. Y.; Tse, P. H. S. *Anal. Chem.* **1985**, *57*. 2351-2357.

15. Leypoldt, J. K.; Gough, D. A. *Anal. Chem.* **1984**, *56*. 2896-2904.

16. Parker, J. W.; Schwartz, C. S. *Biotechnol. Bioeng.* **1987**, *30*. 724-735.

17. Stein, E. W., Grant, P. S., Zhu, H. G.; McShane, M. J. *Anal. Chem.* **2007**, *79*. 1339-1348.

18. Healey, B. G., Li, L.; Walt, D. R. *Biosens. Bioelectron.* **1997**, *12*. 521-529.

19. Li, L.; Walt, D. R. *Anal. Chem.* **1995**, *67*. 3746-3752.

20. Pasic, A., Koehler, H., Schaupp, L., Pieber, T. R.; Klimant, I. *Anal. Bioanal. Chem.* **2006**, *386*. 1293-1302.

21. Pasic, A., Koehler, H., Klimant, I.; Schaupp, L. *Sens. Actuators, B* **2007**, *122*. 60-68.

22. Wolfbeis, O. S., Oehme, I., Papkovskaya, N.; Klimant, I. *Biosens. Bioelectron.* **2000**, *15*. 69-76.

23. Zhang, Y.; Wilson, G. S. *Anal. Chim. Acta* **1993**, *281*. 513-520.

24. Demčenko, A. P., *Introduction to Fluorescence Sensing*. Springer: New York, 2009.

25. Digris, A. V., Novikov, E. G.; Apanasovich, V. V. *Opt. Commun.* **2005**, *252*. 29-38.

26. Nagl, S.; Wolfbeis, O. S. *Analyst* **2007**, *132*. 507-511.

27. Ballew, R. M.; Demas, J. N. *Anal. Chem.* **1989**, *61*. 30-33.

28. Ballew, R. M.; Demas, J. N. *Anal. Chim. Acta* **1991**, *245*. 121-127.

29. Woods, R. J., Scypinski, S.; Love, L. J. C. *Anal. Chem.* **1984**, *56*. 1395-1400.

30. Roberts, J. R., Park, J., Helton, K., Wisniewski, N.; McShane, M. J. *Journal of Diabetes Science and Technology* **2012**, *6*. 1267-1275.

31. Singh, S.; McShane, M. *Biosens. Bioelectron.* **2010**, *25*. 1075-1081.

32. Center for Disease Control and Prevention. National diabetes fact sheet: national estimates and general information on diabetes and prediabetes in the United States, 2011. Atlanta, GA: U.S. Department of Health and Human Services, Centers for Disease Control, 2011.

33. Boyle, J. P. *Population Health Metrics* **2010**, *8*. 29-41.

34. Clarke, S. F.; Foster, J. R. *Br. J. Biomed. Sci.* **2012**, *69*. 83-93.

35. Klonoff, D. C. *Diabetes Care* **2005**, *28*. 1231-1239.

36. Heller, A.; Feldman, B. *Chem. Rev.* **2008**, *108*. 2482-2505.

37. McGarraugh, G. *Diabetes Technol. Ther.* **2009**, *11*. 17-24.

38. Sachedina, N.; Pickup, J. C. *Diabet. Med.* **2003**, *20*. 1012-1015.

39. Chico, A., Vidal-Rios, P., Subira, M.; Novials, A. *Diabetes Care* **2003**, *26*. 1153-1157.

40. Gough, D. A., Kumosa, L. S., Routh, T. L., Lin, J. T.; Lucisano, J. Y. *Sci. Transl. Med.* **2010**, *2*. 42ra53.

41. Guiseppi-Elie, A. *Anal. Bioanal. Chem.* **2010**. 1-17.

42. Maran, A., Crepaldi, C., Tiengo, A., Grassi, G., Vitali, E., Pagano, G., Bistoni, S., Calabrese, G., Santeusanio, F., Leonetti, F., Ribaudo, M., Di Mario, U., Annuzzi, G., Genovese, S., Riccardi, G., Previti, M., Cucinotta, D., Giorgino, F., Bellomo, A., Giorgino, R., Poscia, A.; Varalli, M. *Diabetes Care* **2002**, *25*. 347-352.

43. Pickup, J. C., Claremont, D. J.; Shaw, G. W. *Acta Diabetol.* **1993**, *30*. 143-148.

44. Tamborlane, W. V., Beck, R. W., Bode, B. W., Buckingham, B., Chase, H. P., Clemons, R., Fiallo-Scharer, R., Fox, L. A., Gilliam, L. K., Hirsch, I. B., Huang, E. S., Kollman, C., Kowalski, A. J., Laffel, L., Lawrence, J. M., Lee, J., Mauras, N., O'Grady, M., Ruedy, K. J., Tansey, M., Tsalikian, E., Weinzimer, S., Wilson, D. M., Wolpert, H., Wysocki, T.; Xing, D. *New Engl. J. Med.* **2008**, *359*. 1464-1476.

45. Thome-Duret, V., Gangnerau, M. N., Zhang, Y., Wilson, G. S.; Reach, G. *Diabetes Metab.* **1996**, *22*. 174-178.

46. Weinstein, R. L., Schwartz, S. L., Brazg, R. L., Bugler, J. R., Peyser, T. A.; McGarraugh, G. V. *Diabetes Care* **2007**, *30*. 1125-1130.

47. Rao, G., Glikfeld, P.; Guy, R. *Pharm. Res.* **1993**, *10*. 1751-1755.

48. Rhee, S. Y., Chon, S., Koh, G., Paeng, J. R., Oh, S., Woo, J., Kim, S. W., Kim, J.-W.; Kim, Y. S. *J. Korean Med. Sci.* **2007**, *22*. 70-73.

49. Tierney, M. J., Tamada, J. A., Potts, R. O., Jovanovic, L.; Garg, S. *Biosens. Bioelectron.* **2001**, *16*. 621-629.

50. Vashist, S. K. *Anal. Chim. Acta* **2012**, *750*. 16-27.

51. Lyandres, O., Yuen, J. M., Shah, N. C., VanDuyne, R. P., Walsh, J. T., Jr.; Glucksberg, M. R. *Diabetes Technol. Ther.* **2008**, *10*. 257-265.

52. Baba, J. S., Cameron, B. D., Theru, S.; Cote, G. L. *J. Biomed. Opt.* **2002**, *7*. 321-328.

53. Cameron, B. D., Baba, J. S.; Cote, G. L. *Diabetes Technol. Ther.* **2001**, *3*. 201-207.

54. Cameron, B. D.; Anumula, H. *Diabetes Technol. Ther.* **2006**, *8*. 156-164.

55. Malik, B. H.; Cote, G. L. *Biomed. Opt. Express* **2010**, *1*. 1247-1258.

56. Malik, B. H.; Cote, G. L. *J. Biomed. Opt.* **2010**, *15*.

57. Malik, B. H., Pirnstill, C. W.; Cote, G. L. *J. Biomed. Opt.* **2013**, *18*.

58. Esenaliev, R. O., Larin, K. V., Larina, I. V.; Motamedi, M. *Opt. Lett.* **2001**, *26*. 992-994.

59. Larin, K. V., Eledrisi, M. S., Motamedi, M.; Esenaliev, R. O. *Diabetes Care* **2002**, *25*. 2263-2267.

60. MacKenzie, H. A., Ashton, H. S., Spiers, S., Shen, Y., Freeborn, S. S., Hannigan, J., Lindberg, J.; Rae, P. *Clin. Chem.* **1999**, *45*. 1587-1595.

61. Weiss, R., Yegorchikov, Y., Shusterman, A.; Raz, I. *Diabetes Technol. Ther.* **2007**, *9*. 68-74.

62. Ballerstadt, R., Evans, C., Gowda, A.; McNichols, R. *Diabetes Technol. Ther.* **2006**, *8*. 296-311.

63. Chinnayelka, S.; McShane, M. J. *J. Fluoresc.* **2004**, *14*. 585-595.

64. Meadows, D.; Schultz, J. S. *Talanta* **1988**, *35*. 145-150.

65. Meadows, D. L.; Schultz, J. S. *Anal. Chim. Acta* **1993**, *280*. 21-30.

66. Russell, R. J., Pishko, M. V., Gefrides, C. C., McShane, M. J.; Cote, G. L. *Anal. Chem.* **1999**, *71*. 3126-3132.

67. Tolosa, L., Szmacinski, H., Rao, G.; Lakowicz, J. R. *Anal. Biochem.* **1997**, *250*. 102-108.

68. Tolosa, L., Malak, H., Raob, G.; Lakowicz, J. R. *Sens. Actuators, B* **1997**, *45*. 93-99.

69. Ballerstadt, R.; Schultz, J. S. *Anal. Chem.* **2000**, *72*. 4185-4192.

70. Ballerstadt, R., Polak, A., Beuhler, A.; Frye, J. *Biosens. Bioelectron.* **2004**, *19*. 905-914.

71. Cummins, B. M., Lim, J., Simanek, E. E., Pishko, M. V.; Coté, G. L. *Biomed. Opt. Express* **2011**, *2*. 1243-1257.

72. Ballerstadt, R., Evans, C., McNichols, R.; Gowda, A. *Biosens. Bioelectron.* **2006**, *22*. 275-284.

73. Ge, X. D., Tolosa, L.; Rao, G. *Anal. Chem.* **2004**, *76*. 1403-1410.

74. Khan, F., Gnudi, L.; Pickup, J. C. *Biochem. Biophys. Res. Commun.* **2008**, *365*. 102-106.

75. Judge, K., Morrow, L., Lastovich, A. G., Kurisko, D., Keith, S. C., Hartsell, J., Roberts, B., McVey, E., Weidemaier, K., Win, K.; Hompesch, M. *Diabetes Technol. Ther.* **2011**, *13*. 309-317.

76. Weidemaier, K., Lastovich, A., Keith, S., Pitner, J. B., Sistare, M., Jacobson, R.; Kurisko, D. *Biosens. Bioelectron.* **2011**, *26*. 4117-4123.

77. Khan, F., Saxl, T. E.; Pickup, J. C. *Anal. Biochem.* **2010**, *399*. 39-43.

78. Marvin, J. S.; Hellinga, H. W. *J. Am. Chem. Soc.* **1998**, *120*. 7-11.

79. Thomas, K. J., Sherman, D. B., Amiss, T. J., Andaluz, S. A.; Pitner, J. B. *Diabetes Technol. Ther.* **2006**, *8*. 261-268.

80. D'Auria, S., Herman, P., Rossi, M.; Lakowicz, J. R. *Biochem. Biophys. Res. Commun.* **1999**, *263*. 550-553.

81. D'Auria, S., Di Cesare, N., Gryczynski, Z., Gryczynski, I., Rossi, M.; Lakowicz, J. R. *Biochem. Biophys. Res. Commun.* **2000**, *274*. 727-731.

82. Chaudhary, A., Raina, M., Harma, H., Hanninen, P., McShane, M. J.; Srivastava, R. *Biotechnol. Bioeng.* **2009**, *104*. 1075-1085.

83. Chaudhary, A., Harma, H., Hanninen, P., McShane, M.; Srivastava, R. *Diabetes Technol. Ther.* **2011**, *13*. 827-835.

84. Chinnayelka, S.; McShane, M. J. *Biomacromolecules* **2004**, *5*. 1657-1661.

85. Chinnayelka, S.; McShane, M. J. *Anal. Chem.* **2005**, *77*. 5501-5511.

86. Chinnayelka, S.; McShane, M. J. *Diabetes Technol. Ther.* **2006**, *8*. 269-278.

87. Adhikiri, D. P.; Heagy, M. D. *Tetrahedron Lett.* **1999**, *40*. 7893-7896.

88. Alexeev, V. L., Sharma, A. C., Goponenko, A. V., Das, S., Lednev, I. K., Wilcox, C. S., Finegold, D. N.; Asher, S. A. *Anal. Chem.* **2003**, *75*. 2316-2323.

89. Asher, S. A., Alexeev, V. L., Goponenko, A. V., Sharma, A. C., Lednev, I. K., Wilcox, C. S.; Finegold, D. N. *J. Am. Chem. Soc.* **2003**, *125*. 3322-3329.

90. Badugu, R., Lakowicz, J. R.; Geddes, C. D. *J. Fluoresc.* **2003**, *13*. 371-374.

91. Badugu, R., Lakowicz, J. R.; Geddes, C. D. *Anal. Chem.* **2004**, *76*. 610-618.

92. Badugu, R., Lakowicz, J. R.; Geddes, C. D. *Biorg. Med. Chem.* **2005**, *13*. 113-119.

93. Ben-Moshe, M., Alexeev, V. L.; Asher, S. A. *Anal. Chem.* **2006**, *78*. 5149-5157.

94. Cao, H., Diaz, D. I., DiCesare, N., Lakowicz, J. R.; Heagy, M. D. *Org. Lett.* **2002**, *4*. 1503-1505.

95. Cao, Z., Nandhikonda, P.; Heagy, M. D. *J. Org. Chem.* **2009**, *74*. 3544-3546.

96. Cappuccio, F. E., Suri, J. T., Cordes, D. B., Wessling, R. A.; Singaram, B. *J. Fluoresc.* **2004**, *14*. 521-533.

97. Cordes, D. B., Miller, A., Gamsey, S., Sharrett, Z., Thoniyot, P., Wessling, R.; Singaram, B. *Org. Biomol. Chem.* **2005**, *3*. 1708-1713.

98. DiCesare, N.; Lakowicz, J. R. *Anal. Biochem.* **2001**, *294*. 154-160.

99. DiCesare, N.; Lakowicz, J. R. *Org. Lett.* **2001**, *3*. 3891-3893.

100. Fang, H., Kaur, G.; Wang, B. *J. Fluoresc.* **2004**, *14*. 481-489.

101. Gamsey, S., Suri, J. T., Wessling, R. A.; Singaram, B. *Langmuir* **2006**, *22*. 9067-9074.

102. Gamsey, S., Miller, A., Olmstead, M. M., Beavers, C. M., Hirayama, L. C., Pradhan, S., Wessling, R. A.; Singaram, B. *J. Am. Chem. Soc.* **2007**, *129*. 1278-1286.

103. Holtz, J. H.; Asher, S. A. *Nature* **1997**, *389*. 829-832.

104. James, T. D., Sandanayake, K. R. A. S., Iguchi, R.; Shinkai, S. *J. Am. Chem. Soc.* **1995**, *117*. 8982-8987.

105. Mader, H. S.; Wolfbeis, O. S. *Microchim. Acta* **2008**, *162*. 1-34.

106. Murtaza, Z., Tolosa, L., Harms, P.; Lakowicz, J. R. *J. Fluoresc.* **2002**, *12*. 187-192.

107. Pringsheim, E., Terpetschnig, E., Piletsky, S. A.; Wolfbeis, O. S. *Adv. Mater.* **1999**, *11*. 865-868.

108. Schiller, A., Wessling, R. A.; Singaram, B. *Angew. Chem., Int. Ed.* **2007**, *46*. 6457-6459.

109. Suri, J. T., Cordes, D. B., Cappuccio, F. E., Wessling, R. A.; Singaram, B. *Angew. Chem., Int. Ed.* **2003**, *42*. 5857-5859.

110. Thoniyot, P., Cappuccio, F. E., Gamsey, S., Cordes, D. B., Wessling, R. A.; Singaram, B. *Diabetes Technol. Ther.* **2006**, *8*. 279-287.

111. Wolfbeis, O. S., Klimant, I., Werner, T., Huber, C., Kosch, U., Krause, C., Neurauter, G.; Durkop, A. *Sens. Actuators, B* **1998**, *51*. 17-24.

112. Wu, P., He, Y., Wang, H.-F.; Yan, X.-P. *Anal. Chem.* **2010**, *82*. 1427-1433.

113. Yang, W., Yan, J., Fang, H.; Wang, B. *Chem. Commun.* **2003**, *0*. 792-793.

114. Borisov, S. M.; Wolfbeis, O. S. *Chem. Rev.* **2008**, *108*. 423-461.

115. D'Auria, S., DiCesare, N., Staiano, M., Gryczynski, Z., Rossi, M.; Lakowicz, J. R. *Anal. Biochem.* **2002**, *303*. 138-144.

116. Koncki, R.; Wolfbeis, O. S. *Biosens. Bioelectron.* **1999**, *14*. 87-92.

117. Schaferling, M., Wu, M.; Wolfbeis, O. S. *J. Fluoresc.* **2004**, *14*. 561-568.

118. Wolfbeis, O. S., Schaferling, M.; Durkop, A. *Microchim. Acta* **2003**, *143*. 221-227.

119. Romoser, A., Romoser, D., Ritter, R., Majitha, K., Meissner, M., McShane, C., Sayes, G.; Chirico. *PLoS ONE* **2011**, *6*. e22079.

120. Baker, D. A.; Gough, D. A. *Biosens. Bioelectron.* **1993**, *8*. 433-441.

121. De Benedetto, G. E., Palmisano, F.; Zambonin, P. G. *Biosens. Bioelectron.* **1996**, *11*. 1001-1008.

122. Gregg, B. A.; Heller, A. *Anal. Chem.* **1990**, *62*. 258-263.

123. Tse, P. H. S.; Gough, D. A. *Biotechnol. Bioeng.* **1987**, *29*. 705-713.

124. Stein, E. W.; McShane, M. J. *IEEE Trans. NanoBiosci.* **2003**, *2*. 133-137.

125. Wang, J., Li, S., Mo, J.-W., Porter, J., Musameh, M. M.; Dasgupta, P. K. *Biosens. Bioelectron.* **2002**, *17*. 999-1003.

126. Cass, A. E. G., Davis, G., Francis, G. D., Hill, H. A. O., Aston, W. J., Higgins, I. J., Plotkin, E. V., Scott, L. D. L.; Turner, A. P. F. *Anal. Chem.* **1984**, *56*. 667-671.

127. McMahon, C. P., Killoran, S. J.; O'Neill, R. D. *J. Electroanal. Chem.* **2005**, *580*. 193-202.

128. Andersson, M., Axelsson, A.; Zacchi, G. *Int. J. Pharm.* **1997**, *157*. 199-208.

129. Andrieux, C. P., Audebert, P., Bacchi, P.; Divisia-Blohorn, B. *J. Electroanal. Chem.* **1995**, *394*. 141-148.

130. Dembczynski, R.; Jankowski, T. *Biochem. Eng. J.* **2000**, *6*. 41-44.

131. Han, J. H., Taylor, J. D., Kim, D. S., Kim, Y. S., Kim, Y. T., Cha, G. S.; Nam, H. *Sens. Actuators, B* **2007**, *123*. 384-390.

132. Hepworth, S. J., Leach, M. O.; Doran, S. J. *Phys. Med. Biol.* **1999**, *44*. 1875-1884.

133. Kubin, M.; Spacek, P. *Collect. Czech. Chem. Commun.* **1965**, *30*. 3294-3298.

134. Lee, S., Koh, W., Brunello, G., Choi, J., Bucknall, D.; Jang, S. *Theor. Chem. Acc.* **2012**, *131*. 1-16.

135. Marchesiello, M.; Geniès, E. *J. Electroanal. Chem.* **1993**, *358*. 35-48.

136. Marucci, M., Pettersson, S. G., Ragnarsson, G.; Axelsson, A. *J. Phys. D: Appl. Phys.* **2007**, *40*. 2870-2880.

137. Myung, D., Farooqui, N., Waters, D., Schaber, S., Koh, W., Carrasco, M., Noolandi, J., Frank, C. W.; Ta, C. N. *Curr. Eye Res.* **2008**, *33*. 29-43.

138. Parker, J. W.; Cox, M. E. *J. Polym. Sci., Part A: Polym. Chem.* **1988**, *26*. 1179-1188.

139. Ratner, B. D.; Miller, I. F. *J. Biomed. Mater. Res.* **1973**, *7*. 353-367.

140. Tohda, K., Yamamoto, T.; Gratzl, M. *Supramol. Chem.* **2010**, *22*. 425-433.

141. van Stroe-Biezen, S. A. M., Everaerts, F. M., Janssen, L. J. J.; Tacken, R. A. *Anal. Chim. Acta* **1993**, *273*. 553-560.

142. Gibson, Q. H., Swoboda, B. E. P.; Massey, V. *J. Biol. Chem.* **1964**, *239*. 3927-3934.

143. Atkinson, B.; Lester, D. E. *Biotechnol. Bioeng.* **1974**, *16*. 1299-1320.

144. Bright, H. J.; Gibson, Q. H. *J. Biol. Chem.* **1967**, *242*. 994-1003.

145. Duke, F. R., Weibel, M., Page, D. S., Bulgrin, V. G.; Luthy, J. *J. Am. Chem. Soc.* **1969**, *91*. 3904-3909.

146. Bremer, T. M., Edelman, S. V.; Gough, D. A. *Diabetes Technol. Ther.* **2001**, *3*. 409-418.

147. Carreau, A., Hafny-Rahbi, B. E., Matejuk, A., Grillon, C.; Kieda, C. *J. Cell. Mol. Med.* **2011**, *15*. 1239-1253.

148. Patel, S.; Mehra, A. *ASAIO J.* **1998**, *44*. 157-165.

149. Lakowicz, J. R., *Principles of Fluorescence Spectroscopy*. 3rd ed.; Springer: New York, NY, 2006.

150. Buchholz, K., Kasche, V.; Bornscheuer, U. T., *Biocatalysts and Enzyme Technology*. Wiley-VCH: Weinheim, Great Britain, 2005.

151. Tse, P. H. S., Leypoldt, J. K.; Gough, D. A. *Biotechnol. Bioeng.* **1987**, *29*. 696-704.

152. Collier, B. B., Singh, S.; McShane, M. *Analyst* **2011**, *136*. 962-967.

153. Collier, B. B.; McShane, M. J. *Anal. Chem.* **2012**, *84*. 4725-4731.

154. Clarke, W. L. *Diabetes Technol. Ther.* **2005**, *7*. 776-779.

155. Dieck, R., Measurement Accuracy. In *The Measurement, Instrumentation and Sensors Handbook*. CRC Press: Boca Raton, F.L., 1999.

156. Nagl, S., Stich, M. I. J., Schaferling, M.; Wolfbeis, O. S. *Anal. Bioanal. Chem.* **2009**, *393*. 1199-1207.

157. Schäferling, M. *Angew. Chem. Int. Ed.* **2012**, *51*. 3532-3554.

158. Valledor, M., Carlos Campo, J., Sanchez-Barragan, I., Carlos Viera, J., Costa-Fernandez, J. M.; Sanz-Medel, A. *Sens. Actuators, B* **2006**, *117*. 266-273.

159. Demchenko, A. P. *Lab on a Chip* **2005**, *5*. 1210-1223.

160. Lippitsch, M. E.; Draxler, S. *Sens. Actuators, B* **1993**, *11*. 97-101.

161. Stich, M. I. J., Fischer, L. H.; Wolfbeis, O. S. *Chem. Soc. Rev.* **2010**, *39*. 3102-3114.

162. Stich, M. I. J., Nagl, S., Wolfbeis, O. S., Henne, U.; Schaeferling, M. *Adv. Funct. Mater.* **2008**, *18*. 1399-1406.

163. Feng, Y., Cheng, J., Zhou, L., Zhou, X.; Xiang, H. *Analyst* **2012**, *137*. 4885-4901.

164. Kostov, Y., Harms, P.; Rao, G. *Anal. Biochem.* **2001**, *297*. 105-108.

165. Collier, B. B.; McShane, M. J. *J. Lumin.* **2013**, *144*. 180-190.

166. Szmacinski, H.; Lakowicz, J. R. *Sens. Actuators, B* **1996**, *30*. 207-215.

167. O'Connor, D. V., Ware, W. R.; Andre, J. C. *The Journal of Physical Chemistry* **1979**, *83*. 1333-1343.

168. Guggenheim, E. A. *Philosophical Magazine* **1926**, *2*. 538-543.

169. Isenberg, I.; Dyson, R. D. *Biophys. J.* **1969**, *9*. 1337-1350.

170. Mangelsdorf, J. P. C. *J. Appl. Phys.* **1959**, *30*. 442-443.

171. Moore, C., Chan, S. P., Demas, J. N.; DeGraff, B. A. *Appl. Spectrosc.* **2004**, *58*. 603-607.

172. Johnson, M. L. *Anal. Biochem.* **1992**, *206*. 215-225.

173. Straume, M., Frasier-Cadoret, S.; Johnson, M., Least-Squares Analysis of Fluorescence Data. In *Top. Fluoresc. Spectrosc.*, ed. J. R. Lakowicz. Springer: New York, N.Y., 2002, vol. 2, pp 177-240.

174. Grinvald, A.; Steinberg, I. Z. *Anal. Biochem.* **1974**, *59*. 583-598.

175. Carroll, R. J.; Ruppert, D., *Transformation and Weighting in Regression*. Chapman & Hall: New York, N.Y., 1988.

176. Ryan, T. P., *Modern Regression Methods*. 2nd ed.; Wiley: Hoboken, N.J., 2008.

177. Cline Love, L. J.; Skrilec, M. *Anal. Chem.* **1981**, *53*. 2103-2106.

178. Köllner, M.; Wolfrum, J. *Chem. Phys. Lett.* **1992**, *200*. 199-204.

179. Maus, M., Cotlet, M., Hofkens, J., Gensch, T., De Schryver, F. C., Schaffer, J.; Seidel, C. A. M. *Anal. Chem.* **2001**, *73*. 2078-2086.

180. Greer, J. M., Reed, F. W.; Demas, J. N. *Anal. Chem.* **1981**, *53*. 710-714.

181. Sharman, K. K., Periasamy, A., Ashworth, H.; Demas, J. N. *Anal. Chem.* **1999**, *71*. 947-952.

182. Demas, J. N.; Adamson, A. W. *The Journal of Physical Chemistry* **1971**, *75*. 2463-2466.

183. Jezequel, J. Y., Bouchy, M.; Andre, J. C. *Anal. Chem.* **1982**, *54*. 2199-2204.

184. Hall, P.; Selinger, B. *The Journal of Physical Chemistry* **1981**, *85*. 2941-2946.

185. Soper, S. A.; Legendre, B. L. *Appl. Spectrosc.* **1994**, *48*. 400-405.

186. Tellinghuisen, J.; Wilkerson, C. W. *Anal. Chem.* **1993**, *65*. 1240-1246.

187. Chan, S. P., Fuller, Z. J., Demas, J. N., Ding, F.; DeGraff, B. A. *Appl. Spectrosc.* **2001**, *55*. 1245-1250.

188. Waters, P. D.; Burns, D. H. *Appl. Spectrosc.* **1993**, *47*. 111-115.

189. Chan, S. P., Fuller, Z. J., Demas, J. N.; DeGraff, B. A. *Anal. Chem.* **2001**, *73*. 4486-4490.

190. Hradil, J., Davis, C., Mongey, K., McDonagh, C.; MacCraith, B. D. *Meas. Sci. Technol.* **2002**, *13*. 1552-1557.

191. Bednarkiewicz, A.; Whelan, M. P. *J. Biomed. Opt.* **2008**, *13*. 0413161-1-0413161-13.

192. Stich, M. I. J., Schaeferling, M.; Wolfbeis, O. S. *Adv. Mater.* **2009**, *21*. 2216-2220.

193. Becker, W. *J. Microsc.* **2012**, *247*. 119-136.

194. Weigl, B. H., Holobar, A., Trettnak, W., Klimant, I., Kraus, H., Oleary, P.; Wolfbeis, O. S. *J. Biotechnol.* **1994**, *32*. 127-138.

195. McGraw, C. M., Khalil, G.; Callis, J. B. *Journal of Physical Chemistry C* **2008**, *112*. 8079-8084.

196. Rosso, L.; Fernicola, V. C. *Rev. Sci. Instrum.* **2006**, *77*. 034901-1-034901-6.

197. Gratton, E., Breusegem, S., Sutin, J., Ruan, Q.; Barry, N. *J. Biomed. Opt.* **2003**, *8*. 381-390.

198. Collier, B. B.; McShane, M. J., in *IEEE Sensors*. 2011, pp 943-946.

199. Borisov, S. M., Vasylevska, A. S., Krause, C.; Wolfbeis, O. S. *Adv. Funct. Mater.* **2006**, *16*. 1536-1542.

200. Fischer, L. H., Stich, M. I. J., Wolfbeis, O. S., Tian, N., Holder, E.; Schäferling, M. *Chemistry – A European Journal* **2009**, *15*. 10857-10863.

201. Fischer, L. H., Borisov, S. M., Schaeferling, M., Klimant, I.; Wolfbeis, O. S. *Analyst* **2010**, *135*. 1224-1229.

202. Fischer, L. H., Karakus, C., Meier, R. J., Risch, N., Wolfbeis, O. S., Holder, E.; Schäferling, M. *Chemistry – A European Journal* **2012**, *18*. 15706-15713.

203. Grenoble, S., Gouterman, M., Khalil, G., Callis, J.; Dalton, L. *J. Lumin.* **2005**, *113*. 33-44.

204. Köse, M. E., Carroll, B. F.; Schanze, K. S. *Langmuir* **2005**, *21*. 9121-9129.

205. Köse, M. E., Omar, A., Virgin, C. A., Carroll, B. F.; Schanze, K. S. *Langmuir* **2005**, *21*. 9110-9120.

206. Zelelow, B., Khalil, G. E., Phelan, G., Carlson, B., Gouterman, M., Callis, J. B.; Dalton, L. R. *Sens. Actuators, B* **2003**, *96*. 304-314.

207. Borisov, S., Seifner, R.; Klimant, I. *Anal. Bioanal. Chem.* **2011**. 1-12.

208. Bacon, J. R.; Demas, J. N. *Anal. Chem.* **1983**, *55*. 653-656.

209. Martin, G., James, C., Larry, D., Gamal, K., Youssef, M., Kevin, R. C.; Michel, G. *Meas. Sci. Technol.* **2004**, *15*. 1986.

210. Amao, Y., Asai, K.; Okura, I. *J. Porphyrins Phthalocyanines* **2000**, *4*. 179-184.

211. Amao, Y., Asai, K.; Okura, I. *J. Porphyrins Phthalocyanines* **2000**, *4*. 292-299.

212. Amao, Y., Miyashita, T.; Okura, I. *J. Fluorine Chem.* **2001**, *107*. 101-106.

213. Amao, Y. *Microchim. Acta* **2003**, *143*. 1-12.

214. Demas, J. N., DeGraff, B. A.; Coleman, P. B. *Anal. Chem.* **1999**, *71*. 793A-800A.

215. Lee, S.-K.; Okura, I. *Analyst* **1997**, *122*. 81-84.

216. Lee, S.-K.; Okura, I. *Anal. Commun.* **1997**, *34*. 185-188.

217. Lee, S. K.; Okura, I. *Anal. Chim. Acta* **1997**, *342*. 181-188.

218. Papkovsky, D. B., Ponomarev, G. V., Trettnak, W.; O'Leary, P. *Anal. Chem.* **1995**, *67*. 4112-4117.

219. Papkovsky, D. B.; O'Riordan, T. C. *J. Fluoresc.* **2005**, *15*. 569-584.

220. Borisov, S. M., Gatterer, K., Bitschnau, B.; Klimant, I. *The Journal of Physical Chemistry C* **2010**, *114*. 9118-9124.

221. Brübach, J., Feist, J. P.; Dreizler, A. *Meas. Sci. Technol.* **2008**, *19*. 025602.

222. Carraway, E. R., Demas, J. N., DeGraff, B. A.; Bacon, J. R. *Anal. Chem.* **1991**, *63*. 337-342.

223. Eaton, K.; Douglas, P. *Sens. Actuators, B* **2002**, *82*. 94-104.

224. Hartmann, P.; Trettnak, W. *Anal. Chem.* **1996**, *68*. 2615-2620.

225. Mills, A.; Lepre, A. *Anal. Chem.* **1997**, *69*. 4653-4659.

226. Vasil'ev, V. V.; Borisov, S. M. *Sens. Actuators, B* **2002**, *82*. 272-276.

227. Goff, D. R., *Fiber Optic Video Transmission: The Complete Guide*. Focal Press: Boston, M.A., 2003.

APPENDIX A. TIME-DOMAIN LIFETIME MEASUREMENT SYSTEM

Different combinations of hardware have been utilized for the experiments described within this work. Changes in hardware were made either in an effort to improve the overall system (*e.g.* more sensitive detectors) or to customize it for work with specific luminophores (*e.g.* different excitation/emission spectra). For simplicity, only the latest version of the hardware will be described herein but the setup will be similar to all other configurations utilized in the past. A generalized block diagram of these systems can be seen in Figure A.1.

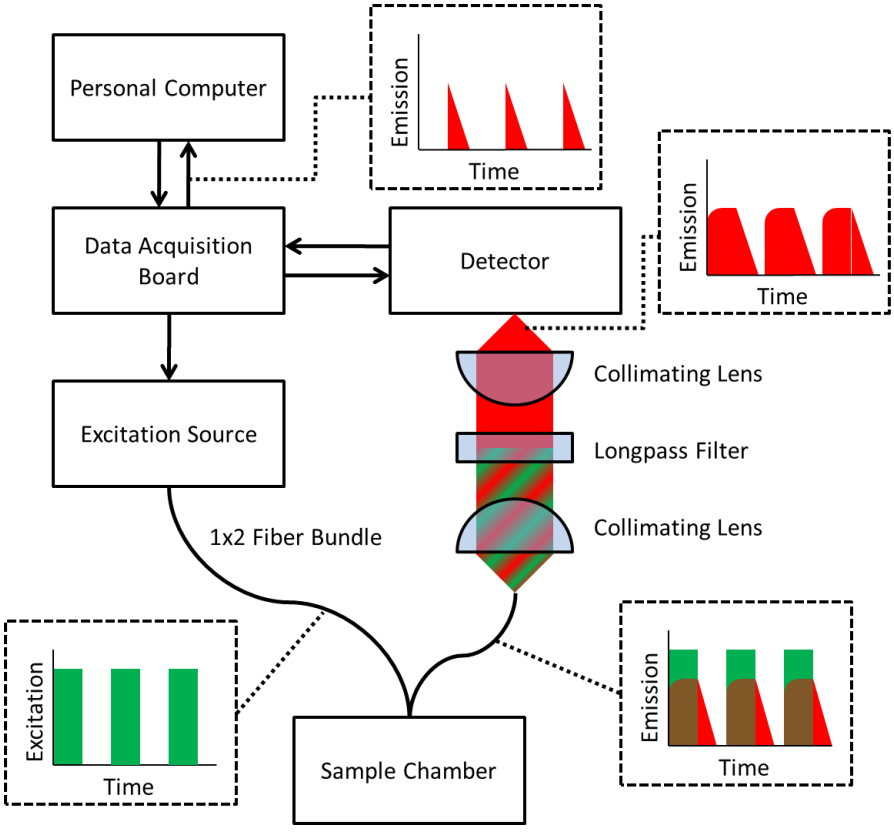

Figure A.1 This block diagram shows the general workings of the custom time-domain lifetime systems utilized in this work. Green represents the pulsed excitation signal while red represents the luminescence emission from the sample.

Table A.1 This table lists different signals found in the circuitry of the TD system and the abbreviations utilized throughout the text. *This describes connections made through the DAQ board only.

Connection	Abbreviation	Line Type*
Signal input from detector	V_{SIG}	Analog Input
LED excitation signal	V_{EX}	Counter
Circuit power	V_{ON}	Analog Output
Detector control voltage	V_C	Analog Output
Switch ground	SG	--

A.1 Circuitry

As can be seen in Figure A.1, a data acquisition (DAQ) board from National Instruments (USB-6361) is used to provide excitation signal as well as collect signals from the detector. In addition to these functions, the DAQ board switches power onto the circuitry controlling the hardware and provides a control voltage to control the detector gain. Connections from the DAQ board to the circuitry (see below) was performed using 4 pair shielded twisted wire. A list of the types of connections used and for what purpose can be found in Table A.1 along with other signals referenced in this work. Each connection will be discussed in further detail in the appropriate section below.

A.1.1 Device Power

To provide consistent power to the detector and the LED control circuit, an AC to DC converter (RECOM RAC15-05DA) was utilized. This component is connected to a standard wall outlet in the U.S. through a three prong cable and converts the 115 V AC

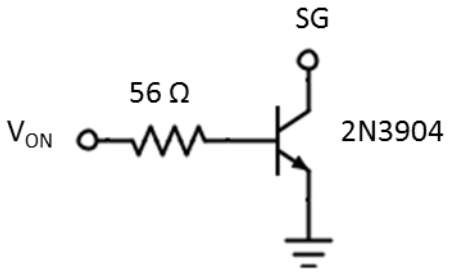

Figure A.2 This circuit shows the use of a common transistor as a switch to turn power on and off to the remaining circuits.

to ±5 V DC. For this device, only the +5 V signal is utilized. A 2A fuse is also included on the input to protect against power surges as suggested by the manufacturer.

To give power to the custom circuitry utilized by the system, a common NPN transistor (2N3904) was utilized as seen in Figure A.2. When power is applied to V_{ON}

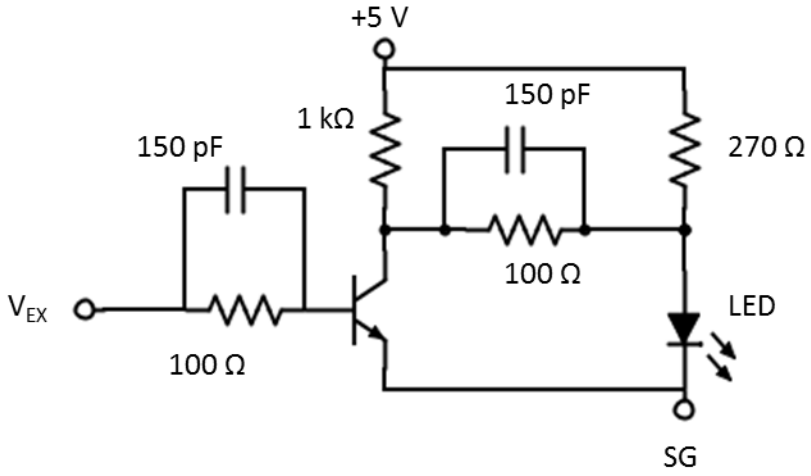

Figure A.3 This circuit is used to drive the LED and ensures that the on/off speed is much faster than the lifetimes measured.

through the DAQ board, the transistor is saturated allowing the rest of the circuit to be grounded through SG.

A.1.2 Excitation Circuit

To drive power to the LED, a fast digital drive circuit was utilized similar to one previously described where the capacitors in the circuit are utilized to improve the on/off speeds of the LED (Figure A.3).[227] This is needed in order to make the edges of the square wave used for excitation as sharp as possible. Ground for the circuit is again provided by the switch circuit shown in Figure A.2.

A.1.3 Detector Connections

The connections made for the detector can be seen in Figure A.4. The decoupling capacitors shown on the control voltage and input power serve to reduce any noise present on these lines. The 100 Ω resistor is needed to convert the current signal output from the detector into a voltage signal that is measurable by the DAQ board on V_{SIG}.

A.2 Optical Components

Although this system is utilized to measure optical responses of luminescent materials, only two parts of the device utilize optical components. The optical components are used for excitation of the luminophore and detection of luminescence following excitation. These two sections are coupled to the sample of interest through a custom 2x1 fiber bundle (CeramOptec Industries, Inc.).

A.2.1 Excitation Signal

For the luminescence measurement of porphyrin responses, green excitation (525

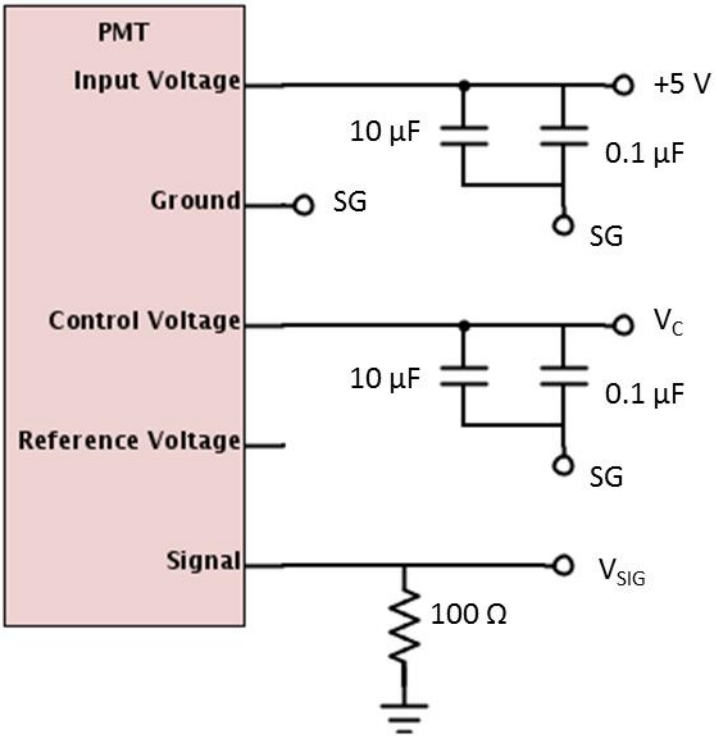

Figure A.4 The connections including decoupling capacitors and a resistor for current-to-voltage conversion for the detector are depicted above.

nm) is often utilized. In order to improve the LED intensity at the sample, a series of lenses with appropriate anti-reflection coatings were used to focus light from the LED onto the fiber bundle. The parts utilized can be found in Table A.2.

A.2.2 Emission and Collection

Similar to the optics utilized for excitation of the sample, lenses were utilized to focus light from the fiber bundle onto the detector and increase efficiency. Anti-reflective coatings for the appropriate wavelengths were again utilized for the spherical lenses. In addition, an optical longpass filter was implemented to ensure that any

Table A.1 The parts below were utilized for the excitation optics. All parts are 1" diameter components (*i.e.* lenses have a diameter of 1"). Values listed with the lens tube refer to the length. The parts are listed in order of the final assembly so that they can be re-assembled if needed.

Part Description	Part Number	Company
Green LED	LED528EHP	Thorlabs
LED Mount	S1LEDM	Thorlabs
0.5" Lens Tube	SM1L05	Thorlabs
Retaining Ring	SM1RR	Thorlabs
Plano-Convex Spherical Lens	LA1951-A	Thorlabs
0.3" Lens Tube	SM1L03	Thorlabs
Adjustable Lens Tube	SM1V05	Thorlabs
Retaining Ring	SM1RR	Thorlabs
Plano-Convex Spherical Lens	LA1951-A	Thorlabs
Locking Ring	SM1NT	Thorlabs
Coupler	SM1T1	Thorlabs
SMA Connector	SM1SMA	Thorlabs

scattered excitation light did not reach the detector. Luminescence was then measured using a photomultiplier tube (PMT) because of to its high sensitivity compared to other detectors. The parts utilized can be found in Table A.3.

A.3 Software

The system and all of its components described above are controlled by a custom LabVIEW (National Instruments) program or virtual instrument (VI) which allows the

Table A.3 The parts below were utilized for the emission optics. Unless mentioned, all parts are 1" diameter components (i.e. lenses have a diameter of 1"). Values listed with the lens tube refer to the length. The parts are listed in order of the final assembly so that they can be re-assembled if needed.

Part Description	Part Number	Company
SMA Connector	SM1SMA	Thorlabs
Coupler	SM1T1	Thorlabs
Locking Ring	SM1NT	Thorlabs
Threaded Union	SM1T2	Thorlabs
Retaining Ring	SM1RR	Thorlabs
Plano-Convex Spherical Lens	LA1951-B	Thorlabs
Retaining Ring	SM1RR	Thorlabs
0.5" Lens Tube	SM1L05	Thorlabs
Retaining Ring	SM1RR	Thorlabs
Longpass Optical Filter	3RD620LP	Omega Optical
Retaining Ring	SM1RR	Thorlabs
Retaining Ring	SM1RR	Thorlabs
Plano-Convex Spherical Lens	LA1951-B	Thorlabs
1" Lens Tube	SM1L10	Thorlabs
0.5" Lens Tube	SM1L05	Thorlabs
C-Mount to 1" Lens Tube Adapter	SM1A9	Thorlabs
C-Mount Adapter	A9865	Hamamatsu
PMT	H10721-20	Hamamatsu

user to extensively control functionality of the system. These functions can be separated into several different sections described below.

A.3.1 Excitation Signal Control

The parts of the excitation signal provided to the sample that can be controlled include the excitation frequency, duty cycle, number of decays collected, and the period between measurements. The excitation frequency controls how fast the excitation pulses of the square wave occur during measurement. The duty cycle refers to the amount of time the LED is on relative to the excitation period. It should be noted that the time the LED is on should be long enough to allow the luminescence to reach steady state to improve the signal-to-noise ratio (SNR) of the decays. Also, the length of data collection is typically a fraction of the time that the LED is off. Longer sampling will not help because the signal will decay to zero. To further improve the SNR of the luminescence decay, multiple decays were often collected and summed for a single lifetime calculation. The measurement period must be greater than the number of decays collected divided by the excitation frequency in order to prevent overworking of the computer. A depiction of these parameters can be found in Figure A.5.

A.3.2 Data Acquisition

The start of data collection for each decay is timed through the software to begin when the clock pulse used for excitation turns the LED off. Through the software, the user is able to control the sampling frequency and the acquisition time. The sampling frequency will be limited by the specifications of the DAQ board which in this case is 2 MHz. The acquisition time, however, will be limited by the amount of time the LED is off which is dependent on the excitation frequency and the duty cycle.

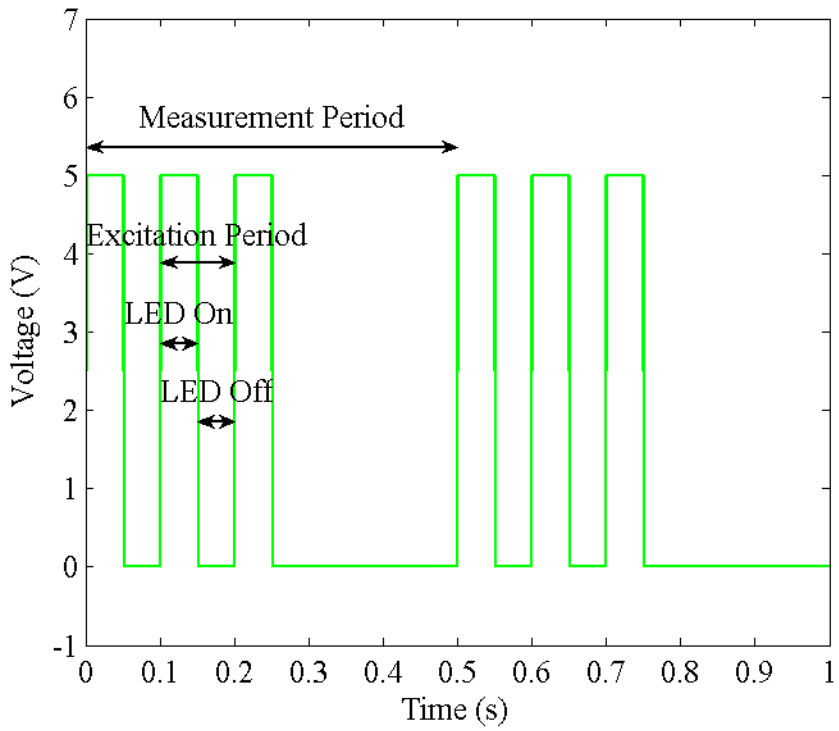

Figure A.5 This figure depicts an example of a 10 Hz excitation signal with a duty cycle of 0.5. During the 0.5 s measurement period, three decays are collected for lifetime calculation.

A.3.3 Lifetime Calculation

After data collection, decays are sent to a LabVIEW sub-VI which calculates the lifetime(s) using one of the algorithms previously discussed. Generally, the user is not given much control over this portion of the software because the algorithm is not expected to change from experiment-to-experiment. However, the user is capable of choosing a delay for lifetime calculation. This delay removes a small portion (~ 1 μs) at the beginning of the decay data which may have interference from scattering or instrumental response of the DAQ board.

A.3.4 Data Storage

Following data collection, the lifetimes calculated and any other appropriate information such as time of measurement are written to a spreadsheet file for later analysis.

APPENDIX B. CUSTOM TESTING BENCH

Oftentimes, the response to of luminescent sensors needs to be characterized for a variety of environmental conditions. Usually this entails testing at a range of analyte concentrations. In order to simplify data collection, automated test benches are often utilized. These systems are pre-programmed by a user to expose the sensors to the desired conditions while the response is recorded and saved for later data analysis. Ultimately, this saves time because the user does not need to be present to constantly monitor the response of the sensor or manually change the environment.

A general overview is provided for the test benches utilized in this and previous works (Figure B.1).[30-31, 152-153] This includes control of three environmental conditions (glucose and oxygen concentration as well as temperature) and the measurement system.

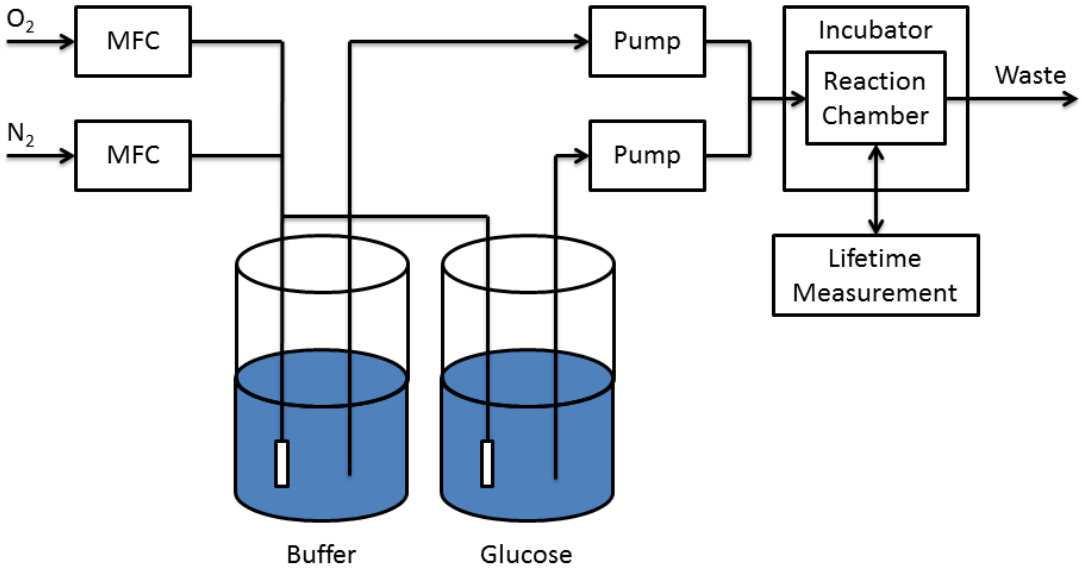

Figure B.1 A general diagram of the test-bench is shown with glucose, oxygen, and temperature control. A computer with custom software (not shown) is used to control the MFCs, pumps, incubator, and the lifetime measurement system.

Control of the system was again performed using custom LabVIEW software (National Instruments). Initially, programs were developed for each environmental element and the measurement system. After validation, these programs were combined to create a single program which encompassed the function of each. The sections below describe the hardware and software used for each environmental entity. Details of the measurement system can found in Appendix A.

B.1 Glucose Concentration Control

As seen in Figure B, control of glucose concentration requires two reservoirs usually containing a phosphate-buffered saline solution. One reservoir also contains glucose at the maximum concentration of interest. Using a pump for each reservoir, solutions from each reservoir are combined to obtain the glucose concentration of interest. This is done by holding the total flow rate constant while varying the flow rate from each reservoir. For example, in order to get a concentration of 100 mg/dL for a reservoir concentration of 400 mg/dL and a total flow rate of 4 mL/min the buffer pump is run at 3 mL/min while the glucose pump is run at 1 mL/min. The concentrations available will be dependent on the resolution of the pumps as well as the maximum and minimum flow rates.

Three different kinds of pumps have been used in the past with this system. Initially, peristaltic pumps (Cole Parmer, Masterflex 7550-50 and 77800-60) were utilized, however, due to the need for frequent calibration, new pumps were sought. Positive displacement piston pumps (VICI Valco Instruments Co., M50) were then integrated into the system to overcome the issue of constant calibration and provide a

much higher resolution. However, the stainless steel parts and the PBS solutions utilized are not very compatible for long-term use without rinsing frequently. The third set of pumps (KNF, STEPDOS 03RC) were utilized positive displacement but with a diaphragm mechanism. Although, they do not provide the resolution as the piston pumps, they have a higher chemical inertness for use with PBS solutions.

Solutions were pumped through standard 1/8" tubing using ¼"-28 threaded ferrules (IDEX Health and Science) and the appropriate adapters when needed. The sensor being tested was immobilized on a glass slide and placed in a custom reaction chamber that contained ports for the tubing coming from the supply reservoirs and out to a waste reservoir. When the chamber was sealed a channel was formed between the top of the chamber and the glass slide using a gasket. This channel allowed solution to flow from the supply over the sensor and out to the waste. The chamber also has a port on the bottom for a fiber optic bundle (see Appendix A) to allow interrogation of the sensor. All three sets of pumps were controlled through USB connections on the computer and LabVIEW software. The software utilized the Virtual Instrument Software Archietecture (VISA) in conjunction with the driver functions provided by the manufacturer for each pump. The functions utilized were able to start and stop the pumps as well as set the flow rates which were calculated based on the desired glucose concentration, total flow rate, and glucose reservoir concentration.

B.2 Oxygen Concentration Control

Control of oxygen concentration is provided in a similar fashion as that for glucose. Rather than utilize liquid pumps, two mass flow controllers (MFCs, MKS

Instruments, 1179A) are used to control the flow of gas. Typically, compressed nitrogen and air were supplied to each MFC, however, nitrogen and oxygen can be used for a wider range of concentrations. The MFCs were controlled through an intermediate controller (MKS Instruments, PR4000) which also provided power to the devices. Two solenoid valves (Omega, SV3106) were placed inline before the MFCs because the MFCs are not rated for use as valves only to control flow rate.

Using ¼" air brake tubing and the appropriate ferrules (Swagelok), gas was flown into the supply reservoirs and dispersed using gas dispersion tubes (Chemglass, CG-203-01) in the case of liquid testing. In the case of dry testing, the gas was allowed to flow directly into to the reaction chamber. USB connections and VISA commands were again used to control flow rates through the MFCs. The solenoids, however, were controlled using a USB I/O Board (Phidgets, Inc., 1011_0) and a pair of relays (Omega, SSRL240AC10). Using LabVIEW and the digital outputs of the I/O Board, the appropriate relays are switched on or off as needed using the AC voltage from a standard U.S. wall outlet. Software provided by Phidgets, Inc. was modified in order to control the digital outputs.

Dissolved oxygen concentrations can be monitored in the reservoir using an amperometric oxygen sensor (PA2000, Unisense). This will ensure that the system is working as desired and allow measurements of the actual oxygen concentration to be made for calibration purposes, if necessary. A two point calibration using air and nitrogen or some other inert gas is required for this device.

B.3 Temperature Control

Temperature control of the system was more straightforward than the other environmental elements. This was done by placing the reaction chamber inside of a programmable incubator (Torrey Pines Scientific, IN35). A port on the side of the incubator was necessary to allow tubing for the solutions and the fiber bundle to connect to the reaction chamber. The incubator was connected to a USB port on the computer and controlled through a VISA interface in LabVIEW. It is important to note that while glucose and oxygen concentrations can be changed almost instantaneously, it takes much more time for the incubator to reach steady-state and even more time for the reaction chamber to reach that temperature throughout.

B.4 Miscellaneous

In case of power outages, most components were connected to an uninterruptible power supply (UPS) which will provide power for a period of time. This will help prevent the loss of data and time since tests run using this system can take several hours to several days depending on the experiment.

APPENDIX C. LIFETIME CALCULATION SOURCE CODE

On the following pages, the MATLAB source code for both single and dual dynamic rapid lifetime determination is included. Commented lines not part of the function of the code begin with a percent symbol ("%"). Each lifetime calculation function begins with a comment section that describes the functions purpose, the inputs required, and the outputs received.

C.1 Dynamic Rapid Lifetime Determination Source Code

```
% ------------------------------------------------------------------------
% DRLD.m
%   Calculates lifetime and pre-exponential factor of a luminescence decay
%
% Syntax:
%
% [tau k] = DRLD(t, int, w1_delay, w_width1)
%
% Inputs:
% t = time array of decay
% int = time-dependent intensity array of decay
% w1_delay = initial time-delay before windows are implemented
%   (utilized to throw out back-scattered light or auto-fluorescence)
% w_width1 = initial window width utilized
%
% Outputs:
% tau = calcualted mono-exponential lifetime of decay provided
% k = calculated pre-exponential factor of decay provided
% ------------------------------------------------------------------------

function [tau k] = DRLD(t, int, w1_delay, w_width1)

ts = 1e-6;  %magnitude of time array, in this case microseconds (1e-6)
fs = 2e6;   %sampling frequency of time-array, 1/fs gives time resolution
        %which is 0.5 microseconds in this case

w_scale = 1.5;  %factor by which to scale windows to calculate lifetime
range1 = 2.7;   %acceptable range of window sum ratios
```

```
range2 = 7.4;

%convert initial window width from time to next highest indexed value
%if not equal
w_width1_i = ceil(w_width1*ts*fs);
%convert window delay from time value to next highest indexed value
%if not equal
w1_delay_i = ceil(fs*w1_delay*ts)+1;
%max window set based on length of time array and window delay previously
%determined
max_window_i = floor((length(t)-w1_delay_i)/2);
%makes sure initial width selected is not larger than max width allowed
w_width1_i = min(max_window_i, w_width1_i);

%max number of iterations allowed before stopping, prevents infinite loops
max_loop = 10;
%initialize iterations number to zero
i = 0;

%loop performed until the ratio of window sums is within the desired
%or another ending condition is met
while(true)
   %increment the iteration number
   i=i+1;

   %determine the start and end times for window (in indices, not time)
   t1 = w1_delay_i;
   t2 = w_width1_i+w1_delay_i;
   t3 = 2*w_width1_i+w1_delay_i;

   %calculate the window sums for each window and the ratio
   w1 = sum(int(t1:t1+w_width1_i));
   w2 = sum(int(t2:t2+w_width1_i));
   R = w1./w2;

   %determine the window width in time value
   dif1 = w_width1_i/fs;
   %calculate the lifetime using RLD equation
   tau = abs((dif1)/log(R));

   %checks if max loop # reached or R within desired range
```

```
   if( (i >= max_loop) || ( (R >= range1) && (R <= range2) ) )
      %exit loop
      break;

   %checks for negative R value indicative of windows being too long
   elseif(R < 0)
      % cut window length in half
      w_width1_i = floor(w_width1_i/2);

   %check if window has reached max width but needs to be larger in order
   %to reach optimal width
   elseif((R < range2)&&(w_width1_i == max_window_i))
      %exit loop because cannot improve further
      break;

   else
      %adjust window width based to estimated optimal value or max
      w_width1_i = min([floor(fs*w_scale*tau), max_window_i]);
   end

end

%determine actual window delay using time value
t1 = t1/fs;
%calculate pre-exponential factor using calculated lifetime, window delay,
%and sampling frequency
k = w1/(tau*(1-1/R)*exp(-t1/tau))/fs;
%convert lifetime to appropriate magnitude
tau = tau/ts;
```

C.2 Dual Dynamic Rapid Lifetime Determination Source Code

```
% ------------------------------------------------------------------------
% DDRLD.m
%   Calculates lifetimes and pre-exponential factors of a dual-exponential
%   luminescence decay of the form I(t) = k1*exp(-t/tau1)+k2*exp(-t/tau2)
%   where k1 and tau1 refer to the lifetime and pre-exponential factor of
%   the shorter-lived dye, and k2 and tau2 refer to the same parameters of
%   the longer-lived dye
%
% Syntax:
```

```
%
% [lt1 k1 lt2 k2] = DDRLD(t, int, w1_delay, w2_delay, w1, w2)
%
% Inputs:
% t = time array of luminescence response
% int = time-dependent intensity array of dual-exponential decay
% w1_delay = initial time-delay before windows are implemented
%   (utilized to throw out back-scattered light or auto-fluorescence)
% w2_delay = initial time-delay of 2nd pair of windows, set high enough
%   to prevent initial interference from shorter-lived luminophore
% w1 = initial window width of 1st set of windows used for tau1 calculation
% w2 = initial window width of 2nd set of windows used for tau2 calculation
%
% Outputs:
% lt1 = calcualted lifetime of shorter-lived dye
% k1 = calculated pre-exponential factor of shorter-lived dye
% lt2 = calculated lifetime of longer-lived dye
% k2 = calculated pre-exponential factor of longer-lived dye
% ------------------------------------------------------------------------

function [lt1 k1 lt2 k2] = DDRLD(t, int, w1_delay, w2_delay, w1, w2)

% maximum number of iterations to perform
max_loop = 10;
% maximum delay for 2nd set of windows
max_w2_delay = 1000;

%iterative loop which solves for lifetimes and pre-exponential factors
for i=1:max_loop;

   %calculate lifetime of longer-lived dye using DRLD and assigned width
   %and delay values
   [lt2, k2] = DRLD(t, int, w2_delay, w2);

   %subtract calculated response of longer-lived dye from total response
   %to obtain decay representative of only shorter-lived dye
   f = int-k2.*exp(-t/lt2);

   %calculate response of shorter-lived dye from new decay using DRLD
   [lt1, k1] = DRLD(t, f, w1_delay, w1);
```

```
    %adjust delay of 2nd set of window to improve lifetime accuracy of both
    %lifetimes
    w2_delay2 = min([5*lt1 max_w2_delay]);

    %if the delay does not change, optimal window widths and delays
    %reached, break from loop
    if(w2_delay2==w2_delay)
       break;
    end

    %assign new delay value for next iteration
    w2_delay = w2_delay2;

end
```